Magnetic properties of Co nanowires self-assembled by pulsed laser deposition

Pedro Schio de Noronha Muniz

UNIVERSIDADE FEDERAL DE SÃO CARLOS

CENTRO DE CIENCIAS EXATAS E TECNOLOGIA

PROGRAMA DE POS-GRADUAÇÃO EM FISICA

&

L'UNIVERSITE PIERRE ET MARIE CURIE

ECOLE DOCTORALE PHYSIQUE ET CHEMIE DES MATERIAUX

Pedro Schio de Noronha Muniz

Propriedades Magnéticas de nanofios de Cobalto auto-formados por deposição à laser pulsado

SÃO CARLOS, SP

2012

Pedro Schio de Noronha Muniz

Propriedades Magnéticas de nanofios de Cobalto auto-formados por deposição à laser pulsado

Tese apresentada em regime de co-tutela entre a Universidade Federal de São Carlos e l'Université Pierre et Marie Curie, ao Programa de Pos-Gradução em Física e à Ecole Doctorale de Physique et de Chimie des Matériaux como parte dos pre-requisitos para obtenção dos títulos de Doutor em Física pela UFSCar e de Docteur en Physique de l'UPMC

ORIENTADORES:

BRASIL: Prof. Dr. Adilson Jesus Aparecido de Oliveira

FRANÇA: Dr. Victor Hugo Etgens

SÃO CARLOS, SP

2012

Thèse de doctorat en cotutelle entre

L'UNIVERSITE PIERRE ET MARIE CURIE
(Ecole doctorale Physique et Chimie des Matériaux)
&
UNIVERSIDADE FEDERAL DE SÃO CARLOS
(Programa de pós-graduação em Física)

Présentée par

Mr. Pedro Schio de Noronha Muniz

Pour obtenir le grade de

DOCTEUR de l'UNIVERSITÉ PIERRE ET MARIE CURIE
&
Doutor em Física pela Universidade Federal de São Carlos

Sujet de la thèse :

Propriétés magnétiques de nanofils de cobalt auto-assemblés élaborés par ablation laser pulsée

Soutenue le 15 février 2012 devant le jury composé de :

Prof. Dr. Adilson Jesus Aperecido de Oliveira	Directeur de thèse, UFSCar
Dr. Victor H. Etgens	Directeur de thèse, UPMC
Prof. Dr. Alberto Passos Guimarães	Rapporteur
Prof. Dr. Paulo Noronha Lisboa-Filho	Rapporteur
Prof. Dr. Andrea Gauzzi	Examinateur
Prof. Dr. José Carlos Egues de Menezes	Examinateur
Dr. Franck Vidal	Invité

Université Pierre & Marie Curie - Paris 6
Bureau d'accueil, inscription des doctorants et base de données
Esc G, 2ème étage
15 rue de l'école de médecine
75270-PARIS CEDEX 06
E-mail : scolarite.doctorat@upmc.fr

Universidade Federal de São Carlos
ProPG - Pró-Reitoria de Pós-Graduação
Rod. Washington Luis, km 235
São Carlos - SP - BR - CEP:13565-905
Telefone: (16)3351 8109
Email: propg@ufscar.br

Agradecimentos

Gostaria de agradecer primeiramente aos membros da banca por terem aceitado o convite de serem jurados do trabalho. Em especial ao professores Dr. Alberto Passos Guimarães e Dr. Paulo Noronha Lisboa-Filho por serem relatores da tese e aos professores Dr. Andrea Gauzzi e Dr. Jos Carlos Egues de Menezes por terem aceitado prontamente o convite apesar da eventual longa distância de seus locais de trabalho até São Carlos.

O trabalho de tese apresentado é fruto de uma colaboração internacional da qual tive a sorte de poder participar. Gostaria de agradecer ao meus orientadores que me convidaram a fazer parte desta colaboração; Dr. Victor Hugo Etgens ao professor Dr. Adilson Jesus Aparecido de Oliveira. Apesar de não ser oficialmente meu orientador, gostaria de agradecer neste momento ao professor Dr. Franck Vidal que me guiou nas discussões de resultados me ensianando muitas coisas e principalmente por ter me auxiliado na escrita deste manuscrito. Além de um incrível conhecimento sobre quase tudo, Franck possui disciplina e dedicação ao trabalho que levarei como exemplo na minha vida de pesquisador.

Neste momento gostaria também de agradecer á algumas pessoas com quem tive o prazer de trabalhar durante os quatro anos de doutoramento.

Gostaria de agradecer à equipe do Instituto de Nanociências de Paris pelo caloroso acolhimento durante meu estágio de um ano e meio em Paris. Em especial ao Dr. Yunlin Zheng que me auxiliou em grande parte dos experimentos e também na compreensão dos mistérios do espaço recíproco; à Dr. Dominique Demaille pelo auxilio nas longas sequências de microscopia e aos amigos Vilmar Fernandes, Benjamin Salles e Francisco Bonilla.

Durante o estágio na França também tive a prazer de conhecer e dividir o escritório com Dr. Juliàn Milano do Instituto Balseiro em San Carlos de Bariloche, Argnetina onde posteriormente fui realizar dois meses de estágio. Gostaria de agradecê-lo pelo acolhimento e pelos bons momentos em Bariloche e em Paris. Gostaria também de agrader ao grupo de resonancias do Instituto Balseiro, principalmente a doutoranda Mariana Barturen pelo auxìlio durante as medidas de resonância e com idioma.

Gostaria de agradecer também ao pessoal do GSM em São Carlos. Aos professores técnicos e alunos que passaram a amigos nestes pouco mais de oito anos de convivência. Obrigado, Alonso, André, César, Cláudio, Driele, Fabiano, Fernando, Gualdi, Maycon, Ortiz.

Gostaria de agradecer imensamente à minha familia, especialmente meus avós *nono* e *nona* e à minha mãe. Obrigado por sempre me acompanharem e torcerem por mim. Não teria nada se não fosse por vocês.

Encerro esta seão agradecendo às agências financiadoras CAPES/COFECUB e FAPESP pelo apoio financeiro durante a realização deste trabalho.

Abstract

The subject of this thesis is the study of the magnetic properties of cobalt nanowires self-assembled in a cerium oxide matrix grown epitaxially on a $SrTiO_3(001)$ substrate. The spontaneous self-assembly of Co nanowires was evidenced in strongly Co-doped thin films grown by pulsed laser deposition. The metallic character of Co has been attested by analysis of X-Ray absorption spectra taken at the Co K-edge at synchrotron SOLEIL (France). The formation of nanowires could be evidenced by transmission electron microscopy experiments carried out in high resolution and energy filtered modes. Combining these results altogether led to the conclusion of Co nanowires formation in the CeO_2 matrix. These nanowires are oriented parallel to the growth direction; have length up to the thickness of film and have a narrow diameter size distribution centered in the 3 - 7 nm range, depending on the growth conditions.

Due to the reduced values of diameter obtained, these nanowires assemblies are model systems for studies in the field of nanomagnetism. The magnetic properties of two nanowires assemblies (with diameters distribution centered on 3 and 5 nm) were investigated in details. The inner structure could be determined by means of transmission electron microscopy and the magnetization reversal was probed through static and dynamic magnetization measurements. Investigation of the magnetic anisotropy was carried out by analysis of resonance ferromagnetic spectra. The localization of the magnetization reversal could be related to the inner structure of nanowires, more precisely to the orientation of hcp Co crystalline grains. In these grains, shape and magnetocrystalline anisotropies compete in strength and direction, leading to a thermally dependent effective anisotropy.

The results presented indicate that it is possible to correlate the magnetic behavior with the real structure of nanowires in these systems.

Resumo

O objeto de estudo da presente tese é o estudo das propriedades magnéticas de nanofios de cobalto auto-formados em matriz isolante de óxido de cério (CeO_2) epitaxiado sobre substrato de titanato de estrôncio ($SrTiO_3$).

A formação espontânea de nanofios de Co metálico foi observada em filmes finos fortemente dopados produzidos por abação laser. O caracter metálico do cobalto presente no filme foi evidenciado através da análise de espectros de absorção de Raios-X na borda K do cobalto realizados no síncrotron SOLEIL (França). Aglomeração na forma de nanofios pôde ser comprovada através de microscopia eletrônica em transmissão de elétrons nos modos de alta resolução e de filtragem em energia (cartografia química). Combinando os resultados, chega-se a conclusão de formação de nanofios metálicos de cobalto orientados paralelamente à direção de crescimento do filme com comprimento podendo alcançar até toda espessura do filme e com uma distribuição estreita de diâmetro centrada entre 3 e 7 nm dependendo das condição de crescimento do filme.

Devido ao diâmetro reduzido, os nanofios são sistemas modelos para estudo em nanomagnetismo. Propriedades de dois conjuntos de nanofios (com diâmetros de 3 e de 5 nm) foram detalhadamente estudadas. A estrutura interna foi determinada por microscopia eletrônica e a reversão de magnetização através de medidas estáticas e dinâmicas. As anisotropias magnéticas das amostras foram investigadas através ressonância ferromagnética. A interpretação dos resultados permitiram evidenciar a localização da reversão de magnetização nos nanofios. A localização foi relacionada à estrutura interna dos nanofios, precisamente à existência de uma textura na orientação de grãos de cobalto hcp. Nestes grãos, anisotropia de forma e anisotropia magnetocristalina competem.

O conjunto de resultados indica que pode-se correlacionar o comportamento magnético com a estrutura real dos nanofios para estes sistema.

Résumé

Le sujet de cette thèse est l'étude de nanofils de cobalt auto-assemblés dans une matrice isolante d'oxyde de cérium (CeO_2) épitaxiée sur SrTiO3(001).

La formation de nanofils de cobalt métalliques a été mise en évidence lors de la croissance de couches minces de CeO_2 fortement dopées au cobalt par ablation laser pulsée. Le caractère métallique du cobalt a été vérifié par des mesures d'absorption X au seuil K du cobalt réalisées au synchrotron. La formation de nanofils a été mise en évidence par des études de microscopie électronique en transmission en mode haute résolution et en mode d'énergie filtrée (cartographie chimique). Ces études combinées montrent la formation de fils métalliques de Co dans la matrice, orientés le long de la direction de croissance, de longueur pouvant aller jusqu'à 400 nm (limitée par l'épaisseur de la couche) et de diamètre très faible, dans la gamme 3-7 nm.

Ces nanofils, en raison de leur diamètre très faible, constituent des systèmes modèles en nanomagnétisme. Deux assemblées de fils (diamètre 3 nm et 5 nm) ont été étudiées en détail. La structure interne des fils a été déterminée par microscopie électronique et le renversement de l'aimantation au moyen de mesures magnétiques statiques et dynamiques (relaxation lente de l'aimantation). L'anisotropie magnétique de ces systèmes a été sondée par résonance ferromagnétique. Ces mesures et leurs interprétations ont permis de mettre en évidence la localisation du renversement de l'aimantation dans les fils. Ce phénomène de localisation a été corrélé à la structure interne des fils, plus précisément à l'existence de grains hexagonaux au sein desquels l'anisotropie magnétocristalline est en compétition avec l'anisotropie de forme.

L'ensemble de ces résultats indique que ces objets sont des systèmes qui pourraient permettre de relier le comportement magnétique à la structure réelle.

Resumo estendido

As propriedades magnéticas dos materiais sempre atraíram a curiosidade e o espírito investigativo da humanidade. Por exemplo, a invenção da bússola e sua utilização para navegação datam do século 10 na China. A ciência moderna vem estudando o magnetismo nos últimos 500 anos. Entretanto, a compreensão dos mecanismos que originam as propriedades magnéticas em materiais só pôde ser obtida no início do século 20 com o desenvolvimento da mecânica quântica e da física do estado sólido.

Além do interesse do ponto de vista fundamental, as propriedades magnéticas dos materiais são amplamente utilizadas em aplicações, por exemplo, como geradores, motores e transformadores elétricos, aceleradores de partículas, amplificadores sonoros e, mais do que nunca, como mídia para armazenamento de informação. Uma verdadeira revolução iniciou-se na segunda metade do século 20, quando se comeou a utilizar magnetismo para armazenamento de informação. Desde então, informação é armazenada na direção de magnetização de um bit ferromagnético. Atualmente existe uma crescente necessidade de se aumentar a capacidade e velocidade no armazenamento, na leitura e na transmissão da informação. Esta necessidade resultou na crescente miniaturização dos bits ferromagnéticos. Entretetanto, a dimensionalidade do sistema influencia fortemente em suas propriedades e neste contexto se insere o trabalho descrito na presente tese.

Especificamente, a presente tese versa sobre as propriedades magnéticas de nanofios de cobalto autoformados em matriz cristalina de óxido de cério (CeO_2). Este trabalho é parte de uma colaboração entre laboratórios no Brasil, França e Argentina. Nesta seção descrevo, em alguns parágrafos escritos em língua portuguesa, um resumo das principais idéias desenvolvidas na tese, que esta escrita em inglês.

O primeiro capítulo da tese apresenta um pequeno histórico do magnetismo e dos modelos científicos desenvolvidos pela humanidade para explicá-lo, destacando a importância da mecânica quântica na descrição completa das propriedades magnéticas nos materiais. Algumas aplicações de materais magnéticos foram citadas destacando-se a utilização de materiais magnéticos como mídia para armazenamento de informação. A crescente miniaturização dos dispositivos induziu interesse prático e acadêmico no estudo da influência da dimensionalidade sobre as propriedades magnéticas dos sistemas. Neste contexto se introduz o tema da presente tese: O estudo das propriedades magnéticas de nanofios de Co auto-formados em matriz de CeO_2.

O segundo capítulo apresenta uma curta introdução às categorias de materiais magnéticos: *diamagnetismo*, *paramagnetismo* e *ferromagnetismo*. Ferromagnetismo é a propriedade mais interessante para aplicações e por isso ganha um destaque na seqüência do capítulo. A formação de domínios magnéticos e as bases da teoria de micromagnetismo são apresentadas assim como algumas das contribuições energéticas que influenciam as propriedades magnéticas. O capítulo se encerra por uma breve revisão do estado da arte da pesquisa de propriedades magnéticas de nanofios.

O terceiro capítulo descreve as técnicas experimentais utilizadas no trabalho, a saber; *deposição por laser pulsado*, *microscopia de transmissão de elétrons*, *espectroscopia de absorção de raios-X*, *magnetometria SQUID* e *ressonância ferromagnética*. Os filmes finos foram produzidos pela técnica deposição por laser pulsado no *Institut des Nanosciences de Paris* (INSP - Paris, França) sobre a supervisão do Dr. Yunlin Zheng e Dr. Franck Vidal, com a assistência da Dra. Dominique Demaille. As caracterizações por microscopia de transmissão de elétrons foram realizadas pela Dra. Dominique Demaille em microscópio pertencente ao *Institut de Minéralogie et de Physique des Milieux Condensés* (IMPMC - Paris, França). Espectroscopia de absorção de raios-X foi executada na linha SAMBA do síncrotron SOLEIL (St Aubin - França) em colaboração com Dr. Emiliano Fonda, quem também realizou as simulações numéricas dos resultados. Medidas de magnetização foram realizadas por mim em magnetômetros SQUID do INSP e do Grupo de Supercondutividade e Magnetismo (GSM - Depto de Física - UFSCar). Medidas de ressonância ferromagnética foram realizadas também por mim no Instituto Balseiro (em San Carlos de Bariloche - Argentina) sobre a supervisão do Dr. Juliàn Milano.

O quarto capítulo inicia com a descrição do crescimento dos fimes finos pela técnica deposição por laser pulsado. As propriedades estruturais e espectroscópicas dos fimes são apresentadas na seqüência. Os resultados de microscopia e de espectroscopia combinados indicam a formação espontânea de nanofios de cobalto metálico nos filmes fortemente dopados. Foi ressaltado que os nanofios são extremamente difícies de se detectar para baixas densidades de Cobalto, o que pode levar a interpretações prematuras sobre a origem de ferromagnetismo em alguns compósitos ditos óxidos magnéticos diluídos. No caso dos filmes estudados, o ferromagnetismo está intrinsecamente ligado à formação espontânea de nanofios.

O mecanismo de formação dos nanofios se apresenta como um interessante objeto de pesquisa. Entretanto, devido ao diâmetro reduzido dos objetos formados (entre 3 e 7 nm

de diâmetro depenedendo das condições de crescimento) a enfâse foi dada às propriedades magnéticas do sistema. Nestas dimensões, o sistema se apresenta como um sistema-modelo para investigação da reversão de magnetização em dimensões reduzidas. As características estruturais de duas amostras que serão detalhadamente estudadas no decorrer da tese, são apresentadas neste capítulo. Estas amostras possuem estreitas distribuições de diâmetro, centradas em 3 nm (amostra d_3) e em 5 nm (amostra d_5).

No capítulo 5 as propriedades magnéticas das amostras d_5 e d_3 foram investigadas através de magnetometria SQUID. Medidas de magnetização e de viscosidade magnética foram realizadas nas duas amostras para se avaliar a influência da dimensionalidade e da estrutura sobre o mecanismo de reversão da magnetização. Para as duas amostras, o comportamento magnético é dominado pela anisotropia de forma dos nanofios e as amostras apresentam eixo de fácil magnetização perpendicular à superfície do filme. Os campos coercivos das amostras, mesmo em baixas temperaturas, são inferiores aos valores teóricos para reversão de magnetização coerente em todo o fio. Este resultado indica a localização da reversão de magnetização.

Um comportamento distinto foi observado para variação do campo coercivo com a temperatura comparando-se as duas amostras. Para d_5, o comportamento pode ser descrito considerando-se que a barreira de energia a ser vencida para que ocorra a reversão não varie com a temperatura. Para a amostra d_3 o modelo de barreira independente da temperatura não ajusta os dados experimentais. Entretanto, un ajuste dos dados pôde ser obtido supondo uma barreira de energia efetiva proveniente proveniente da competição entre energia de forma e energia magnetocristalina. Para d_5 não é necessária a inserção do termo de energia magnetocristalina, e isto indica que a estrutura granular da amostra d_5 deve ser tal que a anisotropia magnetocristalina se anula entre diferentes grãos.

Para obter uma visão mais detalhada do processo de reversão de magnetização nos filmes, a técnica de viscosidade magnética foi utilizada em intervalos amplos de temperaturas e de campos de reversão. O comportamento termicamente ativado com uma barreira de energia independente da temperatura foi confirmado para a amostra d_5. Esta técnica permite ainda uma estimativa do volume de ativação e a variação deste volume em função da temperatura pôde ser ajustada considerando o modelo de barreira de energia independente da temperatura.

Para amostra d_3, os experimentos de viscosidade magnética indicam que a distribuição de barreiras de energia para amostra d_3 possui dois comportamentos distintos em função

da temperatura. Em baixa temperatura, o sistema possui uma distribuição de barreiras de energia mais larga que a alta temperatura. O volume de ativação para a amostra d_3 é pequeno a baixas temperaturas e cresce fortamente com a temperatura até 150 K.

Este comportamento pode ser explicado pelo modelo de anisotropia efetiva derivada da competição entre anisotropias de forma e magnetocristalina. A constante magnetocristalina do Co varia com a temperaura, seu valor é aproximadamente constante para temperaturas até 150 K e descresce rapidamente com aumento da temperatura. Assim a baixa temperatura, a anisotropia magnetocristalina induz uma forte localização da reversão do momento magnético pois possui mesma ordem de grandeza que a anisotropia de forma. Aumentando a temperatura, a anisotropia magnetocristalina diminui e passa a ser menos importante e assim as inomogeneidades não influenciam a distribuição de barreiras de energia.

O capítulo 6 descreve o processo de indexação de padrões de difração múltipla realizado nos nanofios observados em imagens de microscopia de transmissão de elétrons. A análise dos padrões permite determinar a estrutura interna dos nanofios e verificar a as hipóteses levantadas anteriormente. Através de processos de filtragem em imagens de microscopia em alta resolução, uma cartografia dos grãos de cobalto hcp foi obtida para as amostras. Os resultados mostram que para d_5 os grãos são pequenos com dimensão lateral inferior ao diâmetro do nanofio, enquanto que para d_3, os grãos ocupam todo o diâmetro do nanofio e possuem comprimento da ordem de 5 a 20 nanômetros. Estes resultados estão de acordo com as hipóteses anteriormente formuladas nas quais a contribuição magnetocristalina se anularia para d_5 e a amostra d_3 apresentaria grãos onde a anisotropia magnetocristalina compete com anisotropia de forma.

Com intuito de verificar as anisotropias existentes nos filmes finos, resonância ferromagnética dos filmes foi investigada para as duas amostras e os resultados são apresentados no capítulo 6. Os espectros de ressonância confirmam a forte anisotropia existente nos filmes devido à forma dos nanofios, originando um eixo de fácil magnetização na direção perpendicular à superfície do filme. Além do mais, para a amostra d_3 também foi verificada a existência de uma anisotropia no plano da amostra, corroborando com a textura suposta para os grãos no interior dos nanofios. Através de simulações, a técnica de ressonância permitiu estimar valores para constante de anisotropia magnetocristalina e para a razão de aspecto dos domínios magnéticos.

Por fim, o último capítulo apresenta algumas das conclusões obtidas na tese e propõe um modelo para a localização da reversão de magnetização. O modelo permite

calcular o campo de nucleação como uma soma de três termos: (i) termo relacionado com a anisotropia de forma do nanofios; (ii) termo relacionado com a anisotropia magnetocristalina que pode ser inclinada em relação ao eixo dos nanofios; e (iii) um termo relacionado com um aumento em energia de *exchange* nas bordas do grãos. Este modelo sugere que o presente estudo foi capaz de relacionar as propriedades magnéticas com a estrutura real dos nanofios.

Este último capítulo ainda sugere algumas perspectivas para seqüência dos estudos, a citar: (i) explorar diferente diâmentros de nanofios e diferentes estruturas de grãos na tentativa de correlacionar as propriedades magnéticas e estruturais; (ii) tentativa de redução do diâmetro dos objetos. Uma outra perspectiva a médio prazo seria a tentativa de utilizar-se outros materiais magnéticos como dopantes, inclusive ligas. Ainda, a longo prazo, outra possibilidade interessante seria encontrar estratégias para realizar contato elétrico nos objetos para investigar as propriedades de transporte dos nanofios.

Résumé étendu

Les propriétés magnétiques des matériaux ont toujours attiré la curiosité de l'humanité. Par exemple, l'invention de la boussole et son utilisation pour l'orientation datent du 10ème siècle en Chine. La science moderne a beaucoup étudie sur le magnétisme dans les 500 dernières années. Cependant la compréhension des mécanismes à l'origine des propriétés magnétiques des matériaux date seulement du début du 20ème siècle avec le développement de la mécanique quantique et de la physique de la matière condensée.

Au-delà de l'intérêt fondamental, les propriétés magnétiques des matériaux sont largement utilisées dans des applications, comme par exemple: les générateurs, moteurs et transformateurs électriques; les accélérateurs de particules, les amplificateurs sonores et, plus que jamais, dans le stockage d'information. Une vraie révolution a été déclenchée dans la deuxième moitié du 20ème siècle quand s'est initiée l'utilisation du magnétisme pour le stockage de données. Depuis cela, l'information est stockée dans l'orientation de l'aimantation d'un bit ferromagétique. Actuellement il existe un besoin croissant d'augmenter la capacité et la vitesse de stockage, lecture et transmission de l'information. Ceci nécessite une miniaturisation croissante des bits ferromagnétiques. Cependant, la dimensionalité du système influence fortement ses propriétés. C'est dans ce contexte que s'inscrit le présent travail de thèse.

Plus spécifiquement, cette thèse traite des propriétés magnétiques de nanofils de cobalt auto-assemblés dans une matrice d'oxyde de cérium (CeO_2). Ce travail a été méné dans le cadre d'une collaboration internationale entre laboratoires du Brésil, de France et d'Argentine. Dans cette section, je décris dans de brefs paragraphes rédigés en langue française les principales idées développées dans ma thèse, qui est écrite en anglais.

Le premier chapitre de la thèse présente une petite histoire du magnétisme et des modèles scientifiques développés pour l'expliquer, en soulignant l'importance de la mécanique quantique dans la description complète des propriétés magnétiques des matériaux. Aussi, des applications ont été listées, notamment l'utilisation de matériaux magnétiques comme média pour le stockage d'information. La miniaturisation croissante des dispositifs a induit un intérêt scientifique fondamental dans l'étude de l'influence de la dimensionalité sur les propriétés magnétiques. C'est dans ce contexte que s'inscrit le sujet de cette thèse : l'étude des propriétés magnétiques de nanofils de Co

auto-assemblés dans une matrice de CeO_2.

Le deuxième chapitre présente une brève introduction aux catégories de matériaux magnétiques: *diamagnétisme*, *paramagnétisme* et *ferromagnétisme*. Le ferromagnétisme est la propriété la plus intéressante pour des applications, elle est donc décrite plus en détails dans la suite du chapitre. La formation de domaines magnétiques et les bases de la théorie du micromagnétisme sont présentées, ainsi que quelques contributions energétiques qui gouvernent les propriétes des matériaux magnétiques. Le chapitre se termine par un bref aperçu de l'état de l'art de la recherche sur les propriétés magnétiques des nanofils.

Le troisième chapitre décrit les techniques expétimentales utilisées dans ce travail : *croissance par ablation laser pulsée*, *microscopie électronique en transmission*, *spectroscopie d'absorption des rayons X*, *magnétométrie SQUID* et *résonance ferromagnétique*. Les couches minces ont été produites par la technique d'ablation laser pulsée sous la supervision du Dr. Yunlin Zheng et du Dr. Franck Vidal, et avec l'assistance de Dr. Dominique Demaille. Les caractérisations par microscopie électronique en transmission ont été réalisées par Dominique Demaille sur le microscope de l'*Institut de Minéralogie et de Physique des Milieux Condensés* (IMPMC - Paris, France). La spectroscopie d'absorption X a été executée sur la ligne SAMBA du synchrotron SOLEIL (St Aubin - France), en collaboration avec le Dr. Emiliano Fonda qui a mené les simulations numériques des résultats. J'ai realisé les mesures d'aimantation avec des magnétomètres à l'INSP et dans le *Grupo de Superconditividade et Magnetismo* (GSM - Depto de Física - UFSCar). Les mesures de résonance ferromagnétique ont été réalisées à l'Instituto Balseiro (à San Carlos de Bariloche - Argentine) sous la supervision du Dr. Julián Milano.

Le quatrième chapitre débute avec la description de la croissance des couches minces par la technique de d'ablation laser pulsée. L'étude des propriétés structurales des films est ensuite présentée. Les résultats combinés de microscopie et de spectroscopie indiquent la formation spontanée de nanofils de Co métallique dans les films fortement dopés. Il a été souligné que ces nanofils sont extrêmement difficiles à détecter aux faibles concentrations de Co, ce qui peut mener à des conclusions prématurées sur l'origine du ferromagnétisme dans les oxydes magnétiques dilués. Dans les systèmes étudiés ici, le ferromagnétisme est intrinsèquement lié à la formation spontanée des nanofils.

Le mécanisme de formation des nanofils est un sujet intéressant de recherche. Cependant, en raison du faible diamètre des objets formés (entre 3 et 7 nm, dépendant des conditions de croissance), l'accent a été mis sur les propriétés magnétiques du

système qui se présente comme un système modèle pour étudier le renversement de l'aimantation d'objets de dimensions réduites. Les caractéristiques structurales de deux échantillons, étudiés en détail dans la suite du texte, sont présentées. Ces échantillons possèdent des distributions de diamètres étroites, centrées sur 3 nm (échantillon d_3) et sur 5 nm (échantillon d_5).

Dans le chapitre 5, les propriétés magétiques des échantillons d_3 et d_5 ont été étudiées par magnétometrie SQUID. Des mesures de l'aimantation et de la viscosité magnétique ont été realisées pour sonder l'influence des dimensions et de la structure sur le mécanisme de renversement de l'aimantation. Pour les deux échantillons le comportement magnétique est dominé par l'anisotropie de forme des nanofils et les échantillons présentent un axe de facile aimantation perpendiculaire à la surface du film. Les champs coercitifs des échantillons à basse temperature sont inférieurs aux valeurs théoriques attendues pour un renversement cohérent de l'aimantation. Ce résultat indique la localisation du reversement de l'aimantation.

Un comportement différent des échantillons a été observé pour la variation du champ coercitif avec la température. Pour d_5 le comportement peut être décrit en considérant que la barrière d'énergie contraire au renversement de l'aimantation est indépendante de la température. Pour l'échantillon d_3, ce modèle de barrière indépendante de la température ne suffit pas pour ajuster les données expérimentales. Cependant, un ajustement des données peut être obtenu avec l'hypothèse d'une barrière d'énergie provenant de la compétition entre l'anisotropie de forme et l'anisotropie magnétocristalline dans. Dans le cas de l'échantillon d_5, l'insertion du terme lié à l'anisotropie magnetocristalline n'est pas nécessaire. Ceci semble indiquer que la structure granulaire de cet échantillon doit être telle que l'anisotropie magnétocristalline s'annule en moyenne entre les différents grains.

Pour une image plus détaillée du processus de renversement de l'aimantation, la technique de viscosité magnétique a été utilisée sur des intervalles larges de températures et de champs de renversement. Le comportement thermiquement activé avec une barrière d'énergie indépendante de la température a été confirmé pour l'échantillon d_5. Cette technique a également permis d'estimer un volume d'activation et la variation de ce volume avec la température a pu être ajustée en considérant le modèle de barrière d'énergie indépendante de la température.

Pour l'échantillon d_3 , les expériences de viscosité magnétique ont indiqué que la distribution de barrières d'énergie possède deux comportements distincts en fonction de

la température. A basse température, le système possède une distribution de barrières plus large qu'à haute température. Le volume d'activation pour d_3 est faible à basse température et croît fortement avec la température au delà de 150 K.

Ce comportement peut être expliqué par le modèle d'anisotropie effective dérivé de la compétition entre les anistotropies de forme et magnétocristalline. La constante magnetocristalline du Co varie avec la température, sa valeur est approximativement constante jusqu'à 150 K puis décroit rapidement avec l'augmentation de la température. De cette façon, à basse température l'anisotropie magnétocristalline induit une forte localisation du renversement de l'aimantation, car les deux anisotropies possèdent le même ordre de grandeur. En augmentant la température, l'anisotropie magnétocristalline diminue et devient moins importante et de cette façon les inhomogénéités influencent moins la distribution des barrières d'énergie.

Dans le chapitre 6, le processus d'indexation des motifs de diffraction multiple obtenus au niveau des fils par microscopie électronique en transmission est décrit. L'analyse de ces données nous permet de déterminer la structure interne des fils qui vérifie les hypothèses proposées auparavant. Grâce à un processus de filtrage des images en haute résolution, la cartograpie des grains de cobalt hcp dans les fils a été obtenue. Les résultats montrent que pour d_5 les grains sont petits avec des dimensions latérales inférieures au diamètre du nanofil. Pour d_3 les grains occupent tout le diamètre du nanofil et possèdent des longueurs de l'ordre de 5 à 20 nm. Ces résultats confortent les hypothèses formulées antérieurement selon lesquelles la contribution magnétocristalline des grains de d_5 serait moyennée à zero et les grains de d_3 auraient une contribution de l'anisotropie magnétocristalline en compétition avec l'anisotropie de forme.

Avec l'objectif de vérifier les anisotropies existantes dans les films, l'étude par résonance ferromagnétique des deux echantillons a été realisée et les résultats sont présentés dans le chapitre 6. Les spectres de résonance ont confirmé la forte anisotropie existante dans les couches minces liée à l'anisotropie de forme des nanofils, donnant origine à un axe de facile aimantation dans la direction perpendiculaire à la surface du film. De plus, pour l'échantillon d_3, l'existence d'une anisotropie dans le plan de l'échantillon a été vérifiée, corroborant la texture des grains à l'intérieur des nanofils. Grâce à des simulations des champs de résonance, la technique a aussi permis d'estimer les valeurs de la constante d'anisotropie effective et du rapport de forme des domaines magnétiques.

Le dernier chapitre présente les conclusions obtenues au cours de cette thèse ainsi

qu'un modèle permettant d'expliquer la localisation du renversement de l'aimantation. Le modèle permet de calculer le champ de nucléation par une somme de trois termes: (i) un terme lié à l'anisotropie de forme des nanofils; (ii) un terme lié à l'anisotropie magnétocristalline des grains dont l'axe c est incliné par rapport à l'axe des fils; et (iii) un terme relié à l'augmentation de l'énergie d'échange aux bords des grains. La présente étude a permis de corréler les propriétés magnétiques à la structure interne réelle des nanofils.

Le dernier chapitre sugère aussi quelques perspectives pour la suite des études qui sont : (i) explorer différents diamètres de fils et différentes structures des grains en essayant de relier les propriétés magnétiques et structurales; (ii) essayer de réduire encore le diamètre des nanofils. Une autre perspective à moyen terme serait d'utiliser d'autres matériaux dopants pour former les nanofils, en incluant les alliages. A plus long terme, il serait très intéressant de trouver des stratégies pour réaliser des contacts électriques sur les nanofils et étudier leurs propriétés de transport.

Contents

List of Figures

1 Introduction

The magnetic properties of matter intrigue the humankind since the early beginnings of history. The magnetite's ability to attract ferrous materials captivates the imagination of curious spirits, even those who are not interested in science or applications. The observations that steel needles align themselves with the Earth's field when floated or suspended gives origin to the first known application of magnetism properties of materials by humankind, the utilization of a compass for navigation (GUIMARÃES, 2005).

Magnetism has been an intensively studied subject of science over the last five hundred years. The first scientific text on the subject is *De Magnetite* from William Gilbert (1544 - 1603) and dates from 1600 in which it is concluded that the Earth itself behaves as a huge magnet (GILBERT, 1958).

The comprehension that magnetism is correlated with electricity came in 1820. Hans Oersted (1777 - 1851), in Denmark, has demonstrate that a current-carrying wire deflects a needle compass (OERSTED, 1820, 1830). Some times after, the French physician Andre-Marie Ampere(1775 - 1833), extended Oersted's experimental work showing that two parallel wires carrying electric currents repel or attract each other, depending on whether the currents flow in the same or opposite directions (AMPÉRE, 1822).

Years later, Michael Faraday(1791 - 1867) gave to this knowledge revolution his own contribution conceiving the term "field" for the first time in history. Moreover, he discovered electromagnetic induction and applied this concept to elaborate the first electric motor converting electrical energy into mechanical energy. He also performed magneto-optics experiments, discovering the connection between magnetism and light (Faraday effect) (FARADAY, 1839).

These experimental works enabled James Clerk Maxwell (1831 - 1879) to formulate a unified theory of electricity, magnetism and light in 1864, summarized in four equations receiving his name (MAXWELL, 2010). These equations relate electric and magnetic field to distributions of electric charges and current densities in surrounding

space. From a practical point of view, this theory allowed sophisticated applications of magnetism: electric generators, motors, relays, transformers, particle accelerators and amplified music (COEY, 2010).

Despite this revolution in knowledge by humankind, explaining how a solid could possibly be a ferromagnetic was unsolved. The magnetization of such a kind of materials cannot be explained by the proposition of surface current densities because such huge value (hundreds of thousands of amperes) seems highly implausible (SKOMSKI, 2008). The complete comprehension of magnetism in materials could only be achieved with the progress in quantum mechanics and solid state physics in the early beginnings of 20th century. The keys ingredients for magnetism are the magnetic moments that are present in atoms (specifically talking in orbital and spin moments of electrons) and the interaction between then characterizing the magnetism as a cooperative phenomenon (BLUNDELL, 2001).

On the other hand, the magnetism had attracted attention also for practical purposes. A revolution starting in the middle of the twentieth century has changed profoundly the need for speed and capacity in recording/reading/transmitting data. One branch of data recording technology was therefore started around magnetism (GUIMARÃES, 2005). The possibility of writing and rewriting data by reorienting the magnetization of a ferromagnetic particle is used both in analog (audio- and video tapes) and digital (data recording tapes, magnetic arrays and disks) technology. Although there is an immense evolution in hard disk technology with respect to capacity, speed and reliability, the essence did not change: the information is stored by switching the magnetization of a tiny ferromagnetic bit (GUIMARÃES, 2005). This revolution is pushed by scientific advances in the comprehension of magnetic properties and also in the production of magnetic structures. As an example, one can cite the thin film technology and magnetic engineering of multilayers developing new recording materials or the application of new magnetism effects such as Giant or Tunnel Magneto-Resistance (GMR/TMR) in the read-heads (COEY, 2010).

In this context, the study of magnetism in reduced dimensions has attracted a huge effort in the last decades due to the growing miniaturization of electronic devices (SKOMSKI, 2003; GUIMARÃES, 2009). The influence of size on magnetic properties of a system with reduced dimensions and/or dimensionality has practical and academic interest (ATKINSON et al., 2003; GUIMARÃES, 2009). Specifically talking, magnetic nanowires have attracted huge interest. From a basic point of view, magnetic

nanowires are a model system to study the dependence of magnetic reversal on dimensionality, and for practical purpose they have been pointed as a solution to achieve large density of magnetic recording in perpendicular media (ATKINSON et al., 2003; VÁZQUEZ; VIVAS, 2011).

In this thesis, the magnetic properties of Co nanowires arrays self-assembled in an epitaxial cerium oxide matrix were studied. The thin films were grown by pulsed laser deposition with controlled temperature and atmosphere and the structural and magnetic properties were studied by several techniques. The reversal of the magnetization was found to be profoundly dependent on the inner structure of nanowires and local variation of magnetocrystalline anisotropy.

The thesis is organized as follows: the second chapter briefly introduces some basic concepts on the magnetic properties of materials with emphasis on the energetic contributions that govern the behavior of nanostructured magnets. A review of the state of the art in the field of magnetic nanowires is given. In chapter 3 the principal techniques used for the growth and characterization of thin films are described. The fourth chapter presents the growth procedure and the structural properties of the films and in the fifth chapter, the magnetic properties are presented and discussed. A general conclusion on the reversal of the magnetization in nanowires is given in the last chapter.

2 Magnetism in condensed matter

This chapter deals with the origins of magnetic properties in materials first introducing the magnetic moment of atoms and the different magnetic behaviors observed in materials. These different behaviors are related to the crystalline environment sensed by the magnetic moments in a crystal and also to the interactions between these moments.

2.1 Introduction

From classical electromagnetism it is stated that an electric current loop generates a magnetic moment (FEYNMAN; LEIGHTON; SANDS, 1965). If there is a current I around a loop area $\mathbf{dS}$ then the magnetic moment $\mathbf{d}\boldsymbol{\mu}$ generated is given by the product $\mathbf{d}\boldsymbol{\mu} = I\mathbf{dS}$. The magnetic moment has then units of Ampère meters squared (A m^2), the length of $\mathbf{dS}$ vector is the area of the loop and its direction is normal to the loop in a sense determined by the direction of current.

Let us consider a classical picture of an electron (with negative charge of modulus $e = 1.6022\text{x}10^{-19}$ C and mass $m_e = 9.9109\text{x}10^{-31}$ kg) performing a circular orbit around the nucleus of a hydrogen atom with a period τ. The current around the atom is then $I = -\ e/\tau$. The electron velocity modulus is given by $v = 2\pi r/\tau$ with r the radius of the orbit. The electron will have then an angular momentum $m_e vr$ that, from quantum mechanics, must be equal to $\hbar$ in the ground state. This way the magnetic moment is then:

$$|\boldsymbol{\mu}| = \pi r^2 I = -\frac{e\hbar}{2m_e} = -\mu_B \tag{2.1}$$

This equation defines a constant μ_B named Bohr magneton. This is a convenient unit to describe the magnetic moment in atoms and its value is $9.274\text{x}10^{-24}$ A·m^2.

It is possible to define a proportionality between magnetic and angular moments of the electron from Equation (2.1) This constant of proportionality is defined as the gyromagnetic factor γ and its value for the orbital electron angular moment is given by

γ = - $e/2m_e$ = 8.79x10^{10} kg C^{-1}.

The correct description for magnetism come from quantum mechanics arguments where the electrons in atoms have quantized values of orbital angular moment and associated to it quantized values of magnetic moment. The orbital angular moment depends on the electronic state occupied by the electron and is defined with the quantum numbers l and m_l. The magnitude of this orbital angular momentum is $l\sqrt{l(l+1)}\hbar$ and its component in a given direction **i** is $m_l\hbar$. Hence the component of magnetic moment along the direction **i** is $m_l\mu_B$ and the magnetic dipole moment is $l\sqrt{l(l+1)}\mu_B$.

The situation is further complicated by the fact that electrons possess a spin, an intrinsic magnetic moment. The electronic spin has a quantum numbers $s = \frac{1}{2}$ and $m_S = \pm\frac{1}{2}$. The component along the quantization axis is then $\frac{-\hbar}{2}$ or $\frac{\hbar}{2}$. The gyromagnetic factor for the electronic spin is $\gamma = e/m_e$, twice the value for orbital angular moment. An alternative way to express the relation between angular and magnetic moment is the ratio of magnetic moment in units of μ_B to the magnitude of angular moment in units of $\hbar$ as follows:

$$\frac{|\mu|}{\mu_B} = g_l\frac{|l|}{\hbar} = g_s\frac{|s|}{\hbar} \tag{2.2}$$

where this relation defines the g-factor. Its value for orbital angular moment is g_l=1 and for electron spin moment g_s=2.

A direct consequence of the magnetic moment origin is that closed shells have no resultant angular momentum and then do not have magnetic moment. Therefore their contribution to magnetic properties of materials is smaller as will be discussed further.

The magnetic moment $\boldsymbol{\mu}$ interacts with a magnetic field **B**. The energy E is given by E = -$\boldsymbol{\mu}\cdot\mathbf{B}$ and is then minimized when the magnetic moment is parallel to the field. Hence a torque **G** is applied on the magnetic moment, given by $\mathbf{G} = \boldsymbol{\mu}\times\mathbf{B}$.

Now, considering a macroscopic magnetic sample, containing a large number of electrons with magnetic moment, one defines the magnetization **M** as the total magnetic moment per unit volume.

$$\mathbf{M} = \frac{1}{V}\sum_i \boldsymbol{\mu}_i \tag{2.3}$$

where V is the sample volume and the sum extends on all magnetic moments $\boldsymbol{\mu}_i$ present in the sample. The magnetization is a vector and is considered to be continuous over large volumes of the sample (more details on section 2.2). To consider this continuum approximation the length scale should be large enough to average out the graininess due

to individual atoms.

Applying a magnetic field **H** applied on a material, the magnetic moments would respond in a certain way defining magnetic susceptibility χ as:

$$\mathbf{M} = \hat{\chi}\mathbf{H} \tag{2.4}$$

where in the most general case $\hat{\chi}$ is a tensor.

According to this response the magnetic materials can be basically categorized in diamagnetic, paramagnetic, ferromagnetic and antiferromagnetic. The next sections describe the behavior of such materials and the origins of these interactions.

2.1.1 Diamagnetism and Paramagnetism

Lets fist explain here two class of magnetic materials: the diamagnetic and paramagnetic. Diamagnetic materials respond to an applied magnetic field expelling the field lines. This opposition attenuates the magnetic field in the interior of sample by a magnetization in the opposite direction. Paramagnetic materials respond to a magnetic field approximating the field lines. Figure 2.1 present a picture of field lines in presence of diamagnetic and paramagnetic materials. It corresponds to a positive susceptibility and consequently to an alignment of magnetization in the direction of the applied field.

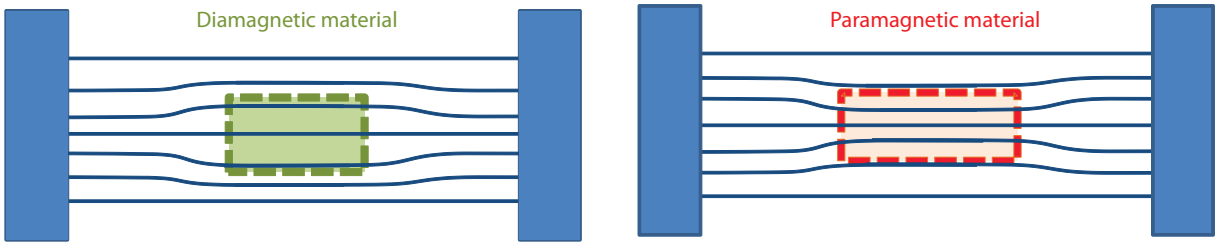

Figure 2.1: Picture of field lines in presence of diamagnetic and paramagnetic materials.

The origin diamagnetism can be explained considering an atom with no unfilled electronic shells under an applied magnetic field. It can be shown that the magnetic field breaks the degeneracy in energy creating a shift in energy. From this shift it is possible to extract the diamagnetic susceptibility (COEY, 2010):

$$\chi_{dia} = -\frac{N}{V}\frac{e^2\mu_0}{6m_e}\sum_i^Z \langle r_i^2 \rangle \tag{2.5}$$

where N is the number of ions with Z electrons of the sample with volume V, and $\langle r_i^2 \rangle$ is the quadratic mean of electronic orbit radius.

The diamagnetic susceptibility χ_{dia} is negative and is weak compared to other magnetic contributions. This is the result for first-order perturbation theory for zero temperature. As the temperature increase the excited states become more important, but it is a marginal effect and the diamagnetic susceptibilities are usually largely temperature independent. For the second order perturbation a positive term is found named *Van Vleckparamagnetism* that is also temperature independent (BLUNDELL, 2001) and is even smaller than diamagnetism.

All materials present some degree of diamagnetism, but due to its weakness it is easily overwhelmed by other magnetic contributions (BLUNDELL, 2001). The materials that present diamagnetism are those with only completed shells. The unpaired electrons contributed for an atomic magnetic moment in atoms. This atomic magnetic moments interacts with an applied magnetic field and are responsible for paramagnetic behavior.

In paramagnetic materials, the magnetic moments arise from orbital and spin magnetic moments of unpaired electrons in the atoms. Due to thermal agitation, the atomic magnetic moments point in random directions in the absence of applied magnetic field and then the net magnetization is zero. Applying a magnetic field, the degree of moment alignment depends proportionally on the strength of the magnetic field at low fields. At higher fields all the moments are pointing parallel to the applied field and the magnetization saturates. The thermal agitation also cause a strongly dependence of the magnetization on this materials with the temperature (at a constant applied field). The Figure 2.2 presents the behavior of the magnetization as a function of the field and also the susceptibility as a function of the temperature for diamagnetic and paramagnetic materials.

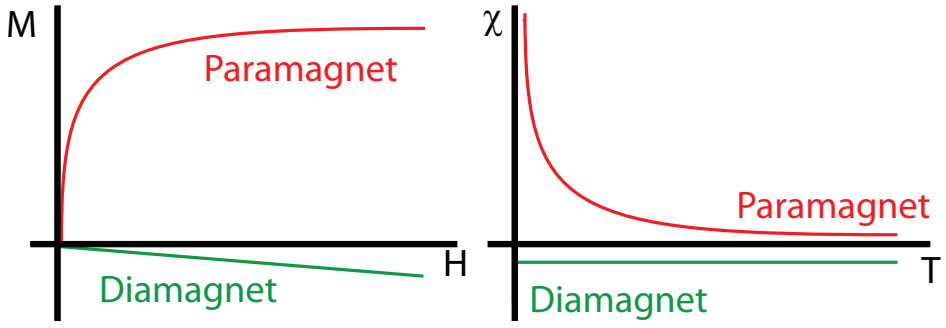

Figure 2.2: Magnetization behavior of paramagnetic and diamagnetic materials in function of magnetic field and temperature.

To account for magnetization dependence on field and temperature for paramagnetic

materials there exist two similar theoretical approaches: the semi-classical approach resulting in the Langevin function; and the quantum approach that results in the Brillouin approach.

The semi-classical treatment supposes that the projection of the magnetic moment on the field direction can present any value (in other words the magnetic moment can point in all directions). The quantum approach consider that the projection of the magnetic moment can only have the values predicted from quantum theory.

For both approaches one considers:

- medium containing a density n of elementary particles that possess a magnetic moment;
- a competition between applied field $\mu_0 H$ tendency of align the dipoles and thermal agitation ($k_B T$)

In both approaches it is possible to obtain the mean value of the magnetization in the direction of the applied field as a function of temperature and magnetic field departing form statistical mechanics arguments. The semi-classical treatment results in the following expression, known as the Langevin equation (GUIMARÃES, 1998):

$$M = n m_0 \left(\coth\left(\frac{m_0 \mu_0 H}{k_B T} \right) - \left(\frac{k_B T}{m_0 \mu_0 H} \right) \right) \tag{2.6}$$

where n is the density of magnetic moments in the sample with value m_0, $\mu_0 H$ is the applied field modulus and T is the temperature.

The result of the quantum mechanics approach is known as the Brillouin function and is:

$$M = n g \mu_B J \left(\frac{2J+1}{2J} \right) \left(\coth\left(\left(\frac{2J+1}{2J} \right) x \right) - \left(\frac{x}{2J} \right) \right) \tag{2.7}$$

where

$$x = \left(\frac{g \mu_B J \mu_0 H}{k_B T} \right) \tag{2.8}$$

with n the density of magnetic moments $g\mu_B J$ in the sample, g the electronic gyromagnetic factor, μ_B the Bohr magneton, $\mu_0 H$ the modulus of applied field, T the temperature and J the total angular momentum quantum number.

The Brillouin theory for localized magnetism explains the magnetic behavior of magnetically diluted 3d and 4f salts. In these salts the magnetic moments do not

interact with each other because the magnetic active ions are separated. The perfect agreement of the theory can be seen in the Figure 2.3 where the magnetization is in function of $x \sim H/T$ for different salts at different temperatures.

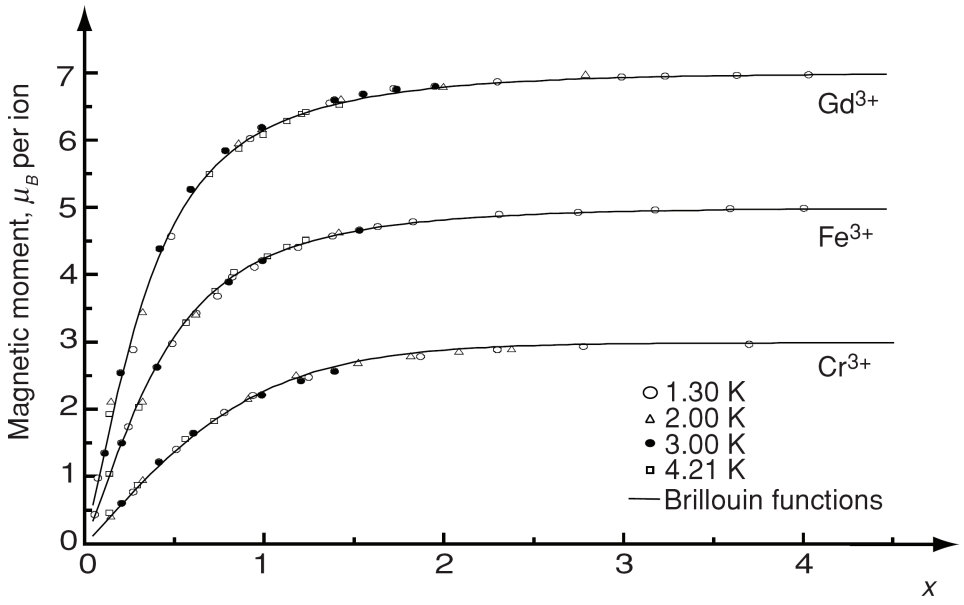

Figure 2.3: Reduced magnetization curves for three paramagnetic salts compared with Brillouin theory predictions. (Reprinted from (COEY, 2010)).

In experiments with paramagnetic samples, at typical values of magnetic field and temperature, the x value is usually small and the $\coth(x)$ can be approximated as

$$\coth(x) = \frac{1}{x} + \frac{x}{3} + ... \tag{2.9}$$

Substituing on Equation (2.13):

$$\frac{M}{ng\mu_B J} = \left(\frac{2J+1}{2J}\right)\left(\frac{2J}{(2J+1)x} + \frac{(2J+1)x}{6J}\right) - \left(\frac{1}{x} + \frac{x}{12J^2}\right) = \frac{(J+1)x}{3J} \tag{2.10}$$

The susceptibility is the rate of change of magnetization with field. Then for small x the susceptibility of a paramagnetic material is:

$$\chi = \frac{ng^2\mu_0\mu_B^2 J(J+1)}{3k_B T} = \frac{C}{T} \tag{2.11}$$

where C is the Curie constant given by:

$$C = \frac{ng^2\mu_0\mu_B^2 J(J+1)}{3k_B} \tag{2.12}$$

The Equation (2.11) is know as Currie Law and is obeyed for many substances (GUIMARÃES, 1998).

Applying a limit of J going to infinity in quantum results leads to the result given by the semi-classical approach. Then the Langevin function is the classical analog of Brillouin function. Indeed the Langevin function describes well the behavior of small magnetic clusters in systems known as *superparamagnetic*. This systems will be referenced latter on section 2.4.1

The Figure 2.4 presents the magnetic susceptibility value for materials as a function of the atomic number excluding those one who are ferromagnetic materials at room temperature.

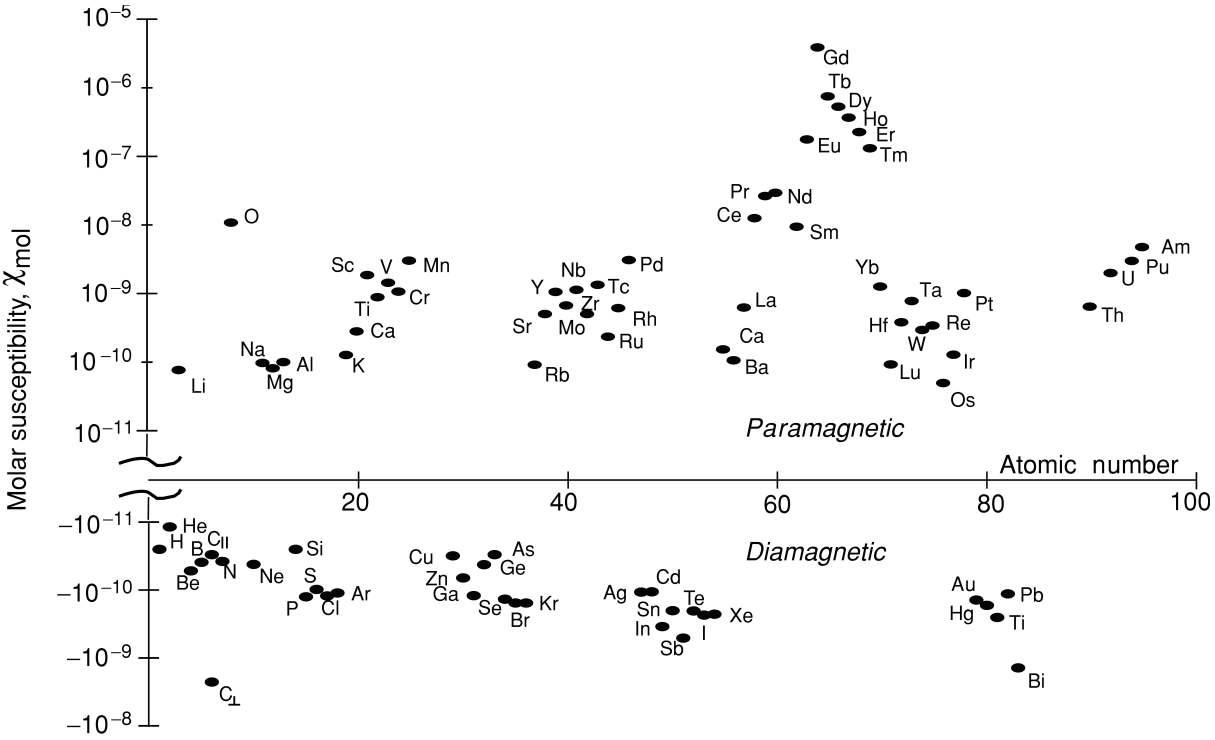

Figure 2.4: Molar susceptibility for diamagnetic and paramagnetic materials at room temperature. (Reprinted from (COEY, 2010)).

2.1.2 Ferromagnetism

For applications, the most important class of magnetic materials is the one gathering the ferromagnetic materials. The principal feature of these materials is their property of retain a remnant magnetization. This means that even in the absence of a magnetic field, they present a non-zero magnetization i.e. their magnetic moments prefer to point in the same direction and sense. Consequently, a characteristic feature of these materials is to present a hysteresis in curves of the magnetization as a function of the magnetic field. The Figure 2.5 presents a magnetic hysteresis cycle and its characteristic features:

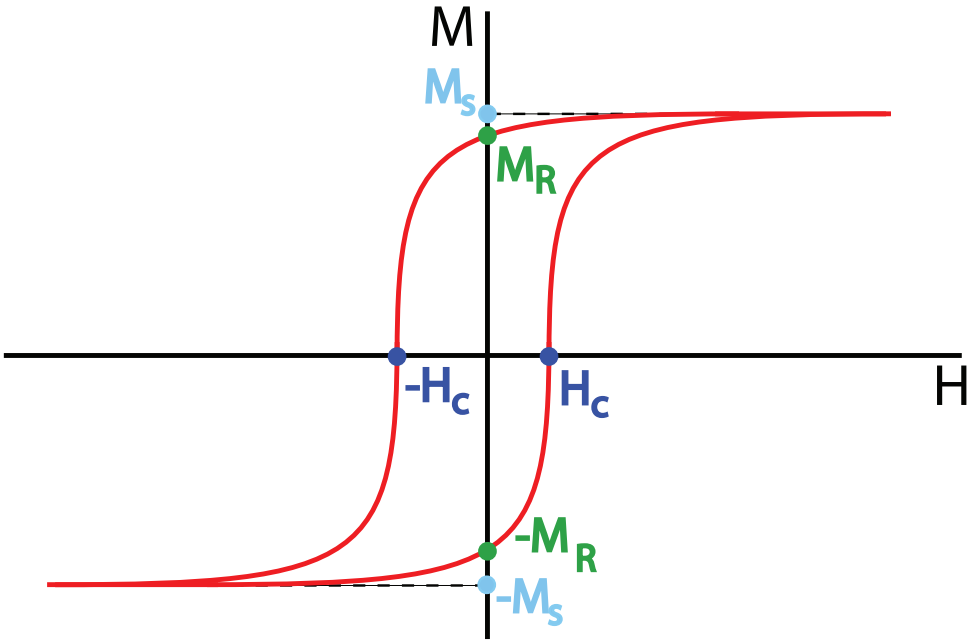

Figure 2.5: Representation of a hysteresis loop with its characteristic features.

M_S is the saturation magnetization; M_R is the remnant value of magnetization and H_C is the coercive field, i.e. the field necessary to attain zero magnetization after having saturated the material. The ferromagnetic properties in such materials are present up to a transition temperature (named *Curie Temperature*) above which they behave like paramagnetic materials.

The origin of ferromagnetic behavior is a strong interaction between the magnetic moments. This interaction favors the alignment of the magnetic moments, pointing in the same direction.

The first theoretical model accounting for ferromagnetic properties is the mean field Weiss model. In this model, it is stated that the magnetic field probed by a magnetic dipole in the sample is the external applied field $\mu_0\mathbf{H}$ plus an internal field proportional

to the total magnetization of sample ($\lambda\mathbf{M}$). Using then the same mechanical arguments of those to attain the Langevin and Brillouin equations it is possible to arrive to a function for magnetization

$$M = ng\mu_B J \left(\frac{2J+1}{2J}\right) \left(\coth\left(\left(\frac{2J+1}{2J}\right)x'\right) - \left(\frac{x'}{2J}\right)\right) \tag{2.13}$$

where

$$x' = \left(\frac{g\mu_B J(\mu_0 H + \lambda M)}{k_B T}\right) \tag{2.14}$$

The equation is similar to Brillouin but the magnetization now appears at the two sides of equation.

The phenomenology of ferromagnetism can be explained by this model, using this equation it is possible to explain qualitatively the thermal dependence of the magnetization, as shown in the case of Ni in Figure 2.6.

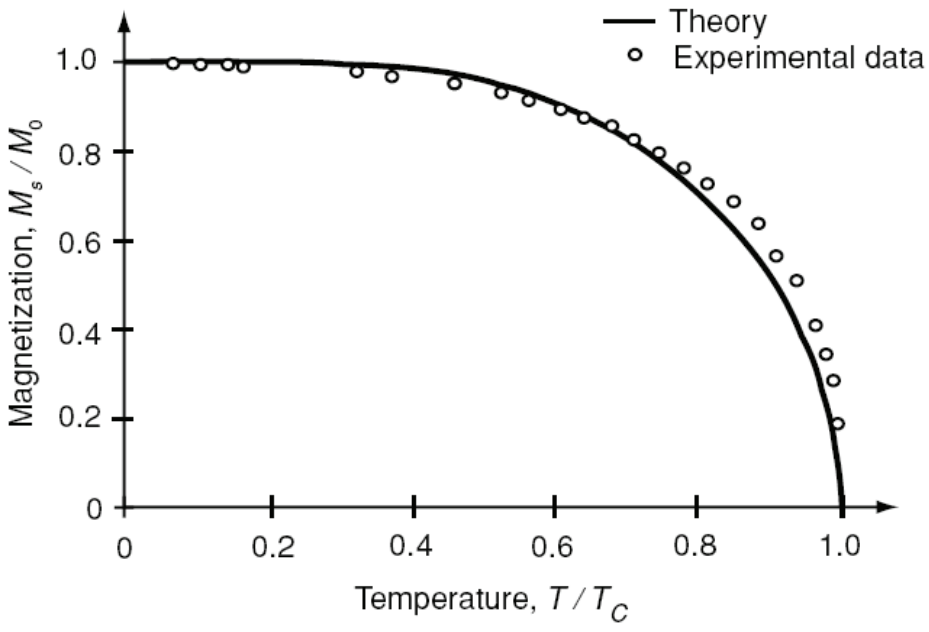

Figure 2.6: Spontaneous magnetization for nickel (circle) and theoretical curve for J = 1/2 from molecular field theory.(Reprinted from (COEY, 2010).)

Applying the approximation for small x' as previously the susceptibility can be evaluated as:

$$\chi = \frac{C}{T - \theta_p} = \frac{C}{T} \tag{2.15}$$

where

$$\theta_p = C\lambda = \frac{\mu_0 n g^2 \mu_B^2 J(J+1)}{3k_B} \tag{2.16}$$

is a parameter named *paramagnetic Curie Temperature*. This parameter should correspond to transition temperature of ferromagnetic order, but experimentally this coincidence is not observed. The Equation (2.15) is known as Curie-Weiss law for para-magnetism. It states then that a ferromagnet behaves as a paramagnet for temperatures above the the Curie temperature.

As was shown the Weiss model can explain some features about ferromagnetism phenomenology but does not explain the origin of the λ parameter. The field inside a ferromagnetic sample is not as high as the field propose: it is only an approximate description of the effect of interaction between the moments (BLUNDELL, 2001). To explain the ferromagnetic order then other arguments are necessary. The key argument has been shown independently by Heisenberg and Dirac in 1926. They found that the interaction between the moments is a quantum mechanical effect named exchange (COEY, 2010).

2.1.2.1 Exchange interaction

The exchange interaction is consequence of simultaneous action of electrostatic repulsion and Pauli's exclusion principle and depends on the relative spin orientation of two electrons at neighbor atoms. Its origin lies in the fact that electrons of two neighboring atoms are indistinguishable and can hop between the two adjacent atoms. Nevertheless, Pauli's exclusion principle forbids them of being in the same quantum state if they have the same spin orientation. There is then an energy difference between parallel and anti-parallel configurations. This exchange energy can be written in the form:

$$E_{ex} = -2J\boldsymbol{S_i} \cdot \boldsymbol{S_j} \tag{2.17}$$

where $\mathbf{S_i}$ and $\mathbf{S_i}$ are the spin magnetic moments of the two atoms and J is the energy difference between configurations and is defined by an integral involving the wave functions of both electrons. J >0 indicates that the spins prefer to align themselves parallel giving rise to a ferromagnetic interaction. Otherwise, if J < 0 the spins prefer the anti-parallel configuration and the interaction is antiferromagnetic. For a macroscopic sample, the interaction is summed on all pairs of atoms in the lattice.

Even if the Weiss theory is not appropriate to explain the magnetism, it is possible

to relate the Weiss constant λ of the molecular field theory to the Heisenberg constant J in the following way:

$$J = \frac{\mu_0 \lambda n g^2 \mu_B^2}{2Z} \tag{2.18}$$

where Z is the number of nearest neighbors in the lattice.

The exchange interaction is responsible for the spontaneous order in some magnetic materials giving origin to several magnetic properties such as ferromagnetism, antiferromagnetism and ferrimagnetism. Depending on the specific mechanism of exchange it can be categorized as direct exchange, RKKY exchange, double exchange or superexchange.

2.1.2.2 Band theory

The picture of localized electrons states evoked above is not appropriate to explain the magnetism in materials presenting metallic conductivity. Theoretical calculations of the exchange integral for the metallic materials have been either of the wrong sign or much too small in magnitude (STUART; MARSHALL, 1960).

The correct description of electrons in these materials requires considering band theory. It was shown by Stoner that a splitting between bands of spin up and spin down can occur spontaneously if the relative gain in exchange interaction is larger than the loss in kinetic energy. In the Stoner model, it is possible to define a criterion that determines if the material is ferromagnetic or not. This criterion is based on the density of states at the Fermi level and on the strength of the exchange correlation. It is then possible to rationalize this criterion in the following way:

Considering a band of energy of a magnetic material, the electrons with the same energy and the same spin state would have the same quantum number and the Pauli's principle would not permit them to get close to each other. This causes an augmentation in the electrons kinetic energy and hence a reduction in the potential energy of particles.

In ferromagnetic materials the gain in kinetic energy must be smaller than the reduction of potential energy. This explains why the ferromagnetism is a property of only some materials. The energy balance can only occurs for materials of appropriate band structure. The appropriate band structure is such that the Fermi energy lies within distinct peak of density of states of each spin polarization (as can be seen in Figure 2.7).

In materials with such band structure a relatively large number of electrons can flip

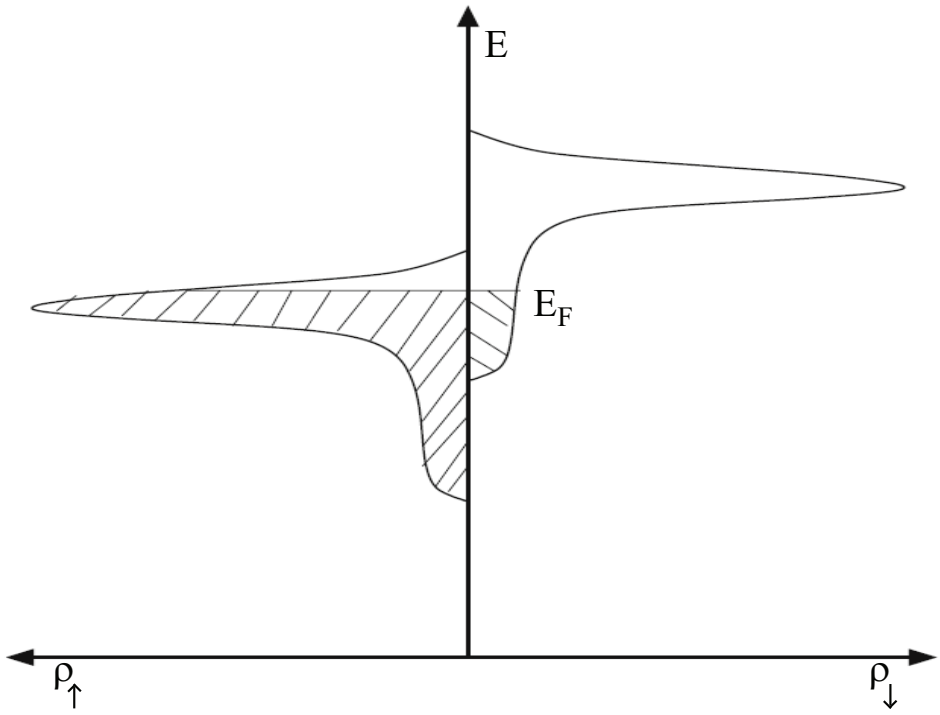

Figure 2.7: Schematic spin-split bands in the ferromagnetic model of Stoner (Reprinted from ref (NOLTING; RAMAKANTH, 2009)).

their spins without gaining too much kinetic energy. The Stoner criterion can also be summarized quantitatively by the inequality (2.19):

$$U\rho(\epsilon_F) > 1 \tag{2.19}$$

where U is a parameter accounting for the strength of exchange and $\rho(\epsilon_F)$ is the density of states at the Fermi level.

Then, if the intra-atomic Coulomb interaction is large, the loss in potential energy is also large favoring ferromagnetism, and at same time, a sharp density of states at Fermi level is convenient because then a relatively large number of electrons can flip their spin without gaining large amount of kinetic energy.

2.2 Micromagnetism

In the previous sections, models explaining the magnetic properties of materials were described. As shown, for some particular band structures, the ferromagnetism is the ground state and the magnetic moments point in the same direction. Despite that, a ferromagnetic macroscopic sample can be found with a magnetization lower than saturation or sometimes with no magnetization even below its Curie temperature. This is caused by the creation of magnetic domains pointing in different directions. In these domains, the magnetization has the saturation value, but averaging over the entire sample a smaller value is generally found.

The creation of these magnetic domains and their sizes can be rationalized with some consideration on the energy of the system. The formation of domains is a direct consequence of free magnetic energy minimization (LANDAU; LIFSHITS, 1935). The free energy of samples can have different contributions that will be discussed in the following sections. The new branch of study created from this theoretical point of view is named *micromagnetism*.

2.2.1 Exchange Energy: Stiffness

As discussed in the previous section, the ground state for a ferromagnetic specimen is to have all magnetic moments parallel to each other. Deviation of this ideal case will induce an energy cost that can be described by a "stiffness" constant (LANDAU; LIFSHITS, 1935):

$$E_x = A \int (\boldsymbol{\nabla} \cdot \boldsymbol{m})^2 dV \tag{2.20}$$

where the integral is performed on the entire volume of the sample, $\mathbf{m}$ is the local magnetization vector and A is the stiffness constant that is material dependent and is related to the exchange integral, the spin, and the lattice constant (a_L) of the material: $A = \xi JS^2/a_L$. ξ is an integer whose value depends on the lattice. This equation can also be obtained by a Taylor expansion of the discrete Heisenberg energy function (Equation (2.17)). Even if the discrete approach is not applicable in the case of metallic ferromagnetic materials, the Equation (2.20) still describes phenomenologically the stiffness effects (HUBERT; SCHÄFER, 2009).

2.2.2 Magnetocrystalline anisotropy energy

In a cubic system, the distance between two neighboring atoms is bigger in the <111> direction than in the <110> or in the <100> direction. Properties that depend on the electronic configuration can then be different in these directions. For magnetic properties this phenomenology is known as magnetocrystalline anisotropy and is a direct consequence of spin-orbit coupling (HUBERT; SCHÄFER, 2009; COEY, 2010). Indeed, in a ferromagnetic crystal the magnetization can have some preferential directions relative to the crystallographic axes of the material. The preferential axis is named easy axis and for correspondence the opposite is the hard axis (or hard plane).

Magnetization measurements of a single crystalline ferromagnetic material then depend on the direction of the applied field. Figure 2.8 presents results obtained for Fe, Ni, and Co. For Fe, the easy axis is <100> while <110> and <111> are the hard axis; for Ni, <111> is the easy axis while <110> and <100> are the hard axis; and for hexagonal Co, the <0001> is the easy axis and the plane perpendicular to it is a hard plane.

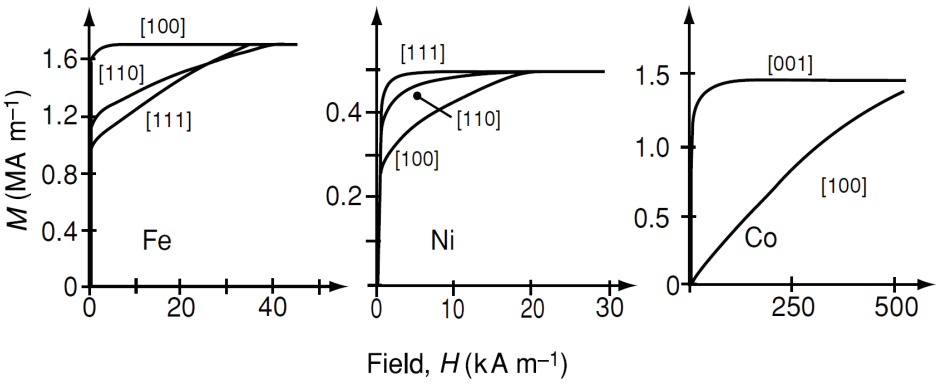

Figure 2.8: Magnetization of single crystals of Fe, Ni, and hexagonal Co for the different crystalline axes (Reprinted from ref (COEY, 2010)).

One can describe this with an energetic term depending on the symmetry of the lattice. For example, in cubic systems the density of magnetocrystalline energy can be written as:

$$E_{Crys,Cubic} = K_{1,c}(m_1^2 m_2^2 + m_1^2 m_3^2 + m_2^2 m_3^2) + K_{2,c}(m_1^2 m_2^2 m_3^2) \tag{2.21}$$

where m_i are the magnetization components along the cubic axes and $K_{1,c}$ and $K_{2,c}$ are constants. This equation is an approximation following a Taylor expansion and, generally, $K_{2,c}$ and the higher order terms are neglected. The $K_{1,c}$ constant has values

of $\pm 10^4$ J/m^3 (Joules per cubic meter) for different materials and its sign determines whether <100> ($K_{1,c} > 0$) or <111> ($K_{1,c} < 0$) are the easy directions. The Figure 2.9 presents the calculated energy surfaces for Fe and Ni, presenting the symmetry of the magnetocrystalline anisotropy in these materials.

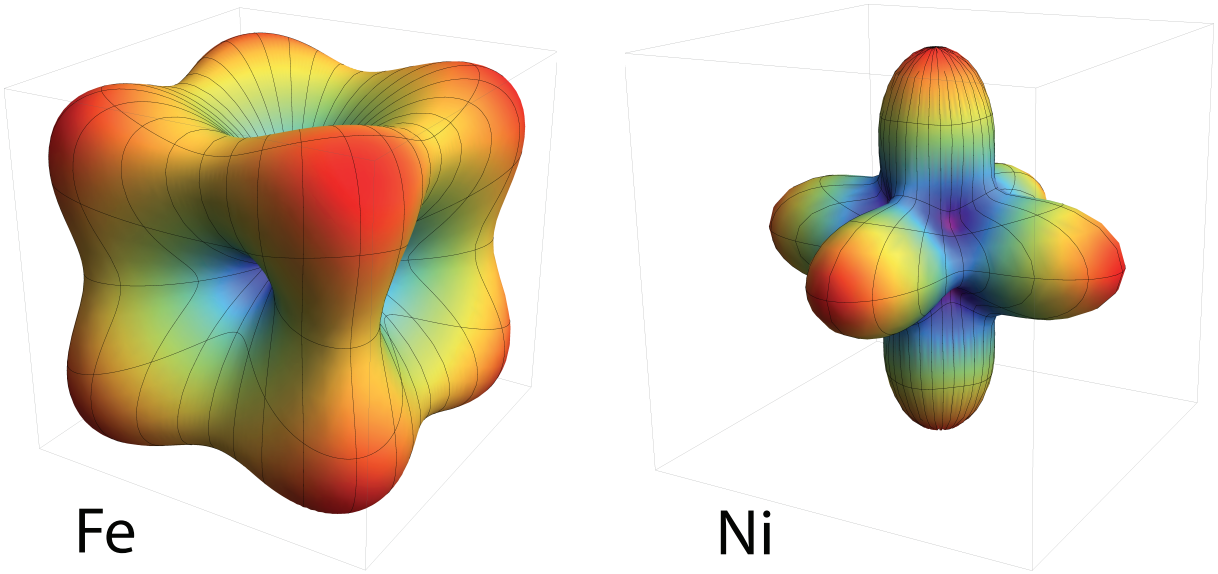

Figure 2.9: Energy surfaces for Fe and Ni calculated from Equation (2.21) with Mathematica software.

For hexagonal (or also tetragonal) structures, the anisotropy usually found has one axis of symmetry and is then named uniaxial anisotropy. The angular dependence of the magnetocrystalline energy in this case can be approximated up to the fourth-order as:

$$E_{Crys,Uniaxi} = K_{1,u}\cos^2(\theta) + K_{4,u}\cos^4(\theta) \tag{2.22}$$

where θ is the angle between the magnetization and the anisotropy axis. A large positive $K_{1,u}$ defines an easy axis and a large and negative $K_{1,u}$ defines an easy plane perpendicular to the anisotropy axis. For intermediate values, under the condition $0 > K_{1,u}/K_{2,u} > -2$, the easy axis lie on a cone with an angle γ relative to the axis given by $\sin^2(\gamma) = -\frac{1}{2}K_{1,u}/K_{2,u}$. The energy surface for these three cases are presented in Figure 2.10 and are named uniaxial, planar and conical magnetic anisotropies. The uniaxial anisotropies can be much stronger than cubic anisotropies, reaching 10^7 J/m^3 (Joules per cubic meter) for rare earth transition metals.

An additional term that can play an important role in magnetic domain formation was introduced by Néel and applies only to surface magnetization.It is the surface magnetic

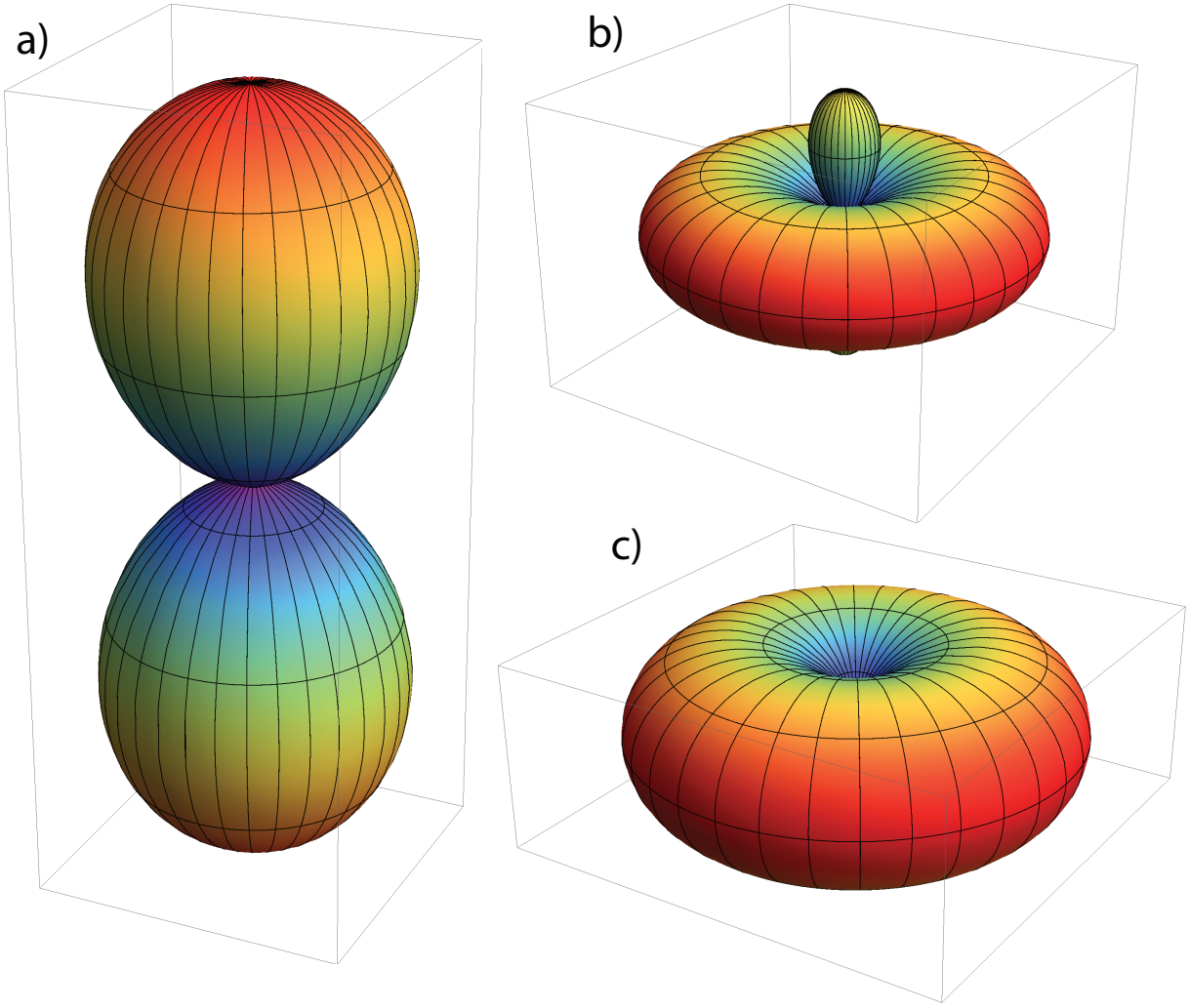

Figure 2.10: Energy surfaces calculated from Equation (2.22) with Mathematica software. The surfaces represent a planar (a), conical (b) and an uniaxial anisotropy (c).

anisotropy. It can be described by some phenomenological parameters as:

$$e_S = K_S(1 - (\boldsymbol{m} \cdot \boldsymbol{n})^2) \tag{2.23}$$

where $\mathbf{n}$ is the surface normal and K_S is the anisotropy constant. This expression must be integrated over the surface of the sample.

Also, non uniform samples in which exchanged coupled ferromagnetic and antiferromagnetic phases exist side by side often show asymmetrical magnetization curves. This occurs because the ferromagnetic phase has a preferential orientation induced by the antiferromagnetic phase. This anisotropy can be described as:

$$e_{XA} = K_{XA}\cos(\theta) \tag{2.24}$$

where θ is the angle between the magnetization and its preferential orientation in the ferromagnetic phase.

2.2.3 Interaction with external field: Zeeman energy

The magnetization of a sample interacts with the external applied field and this interaction needs also to be taken into account in the energy balance. The interaction between magnetization and the applied field can be written as:

$$E_Z = -M_s \int (\boldsymbol{H_{ex}} \cdot \boldsymbol{m}) dV \tag{2.25}$$

where M_s is the saturation magnetization, $\boldsymbol{H_{ex}}$ is the external applied field and $\boldsymbol{m}$ is a continuous approximation of the magnetization direction over the sample. For uniform external field, this energy only depends on the average magnetization and not on the particular domain structure of the sample, reducing to the form E_Z = -$\boldsymbol{M}\cdot\boldsymbol{H_{ex}}$.

2.2.4 Self-interaction energy

The magnetization on a sample generates itself a magnetic field. This magnetic field is called stray field $\boldsymbol{H_d}$ and can be defined by the divergence of $\mathbf{M}$ as:

$$\mu_0 \nabla \boldsymbol{H_d} = -\nabla \boldsymbol{M} \tag{2.26}$$

A uniformly magnetized sample carries then an energy excess coming from the interaction between the magnetization and this field. This energy can be written as:

$$E_d = -\frac{1}{2} \int_{sample} \boldsymbol{H_d} \cdot \boldsymbol{M} dV \tag{2.27}$$

where the integral is performed only over the sample. This energy is always positive and is only zero if the stray field is zero.

The effect of the stray field inside the sample is opposite to magnetization and, for this reason, it is sometimes named demagnetizing field. The stray field is linked to the magnetic poles created on the samples edges. The demagnetizing field is uniform and linearly related to the magnetization by a tensor $\mathbf{N}$:

$$\boldsymbol{H_d} = -\frac{1}{\mu_0} \boldsymbol{N} \cdot \boldsymbol{M} \tag{2.28}$$

Calculating this demagnetizing field implies the calculation of integrals of volume and surface density of charges defined as a function of the magnetization. Such calculation depends on the geometry of the sample and for most cases it can be very complicated (HUBERT; SCHÄFER, 2009). In a few simple cases, it can be calculated easily as for example in the case of a uniformly magnetized ellipsoid. For a general ellipsoid with axis (a, b, c) the demagnetizing factor along the a axis is given by:

$$N_a = \frac{1}{2}abc \int_0^\infty \frac{d\eta}{(a^2+\eta)\sqrt{(a^2+\eta)(b^2+\eta)(c^2+\eta)}} \tag{2.29}$$

Analogous expressions apply to N_b and N_c and the sum of the three coefficient is always equal to one. Explicit formulas are available for ellipsoids of revolution. For the case of prolate ellipsoid (cigar-shaped) with dimensions (a, a, c) and $\alpha = c/a > 1$ the demagnetizing factors are:

$$N_c = \frac{1}{\alpha^2-1}\left[\frac{\alpha}{\sqrt{\alpha^2-1}}\ln(\alpha+\sqrt{\alpha^2-1}) - 1\right] \tag{2.30}$$

$$N_a = \frac{1-N_c}{2} \tag{2.31}$$

For a oblate (disc-shaped) ellipsoids with dimensions (a, c, c) and $\alpha = c/a > 1$ the equations are:

$$N_a = \frac{\alpha^2}{\alpha^2-1}\left[1 - \frac{1}{\sqrt{\alpha^2-1}}\arcsin\left(\frac{\sqrt{\alpha^2-1}}{\alpha}\right)\right] \tag{2.32}$$

$$N_c = \frac{1-N_a}{2} \tag{2.33}$$

The energy associated to the stray field can be written as a function of these demagnetizing factors as:

$$E_d = \frac{\mu_0 M_S^2}{2}\left(N_c \sin^2\theta + N_a \cos^2\theta\right) \tag{2.34}$$

where θ is the angle between the magnetization and the a axis of the ellipsoid. Hence, the demagnetizing field contribution is analogous to an uniaxial anisotropy energy even if its origin is not related to spin-orbit coupling. Therefore, the magnetization has a preferential direction and this contribution is also called shape anisotropy.

2.2.5 Free energy analysis: characteristic lengths of magnetism

Analyzing the magnetic response through the energetic considerations made in previous sections is a branch of scientific research named *micromagnetism*. It is based on the supposition that the magnetization in a sample can be described as a continuous variable and that the magnetic free energy minimization determines the local magnetization. Hence, the magnetic properties are the result of the competition between interatomic exchange, anisotropies, Zeeman energy and magnetostatic interactions.

Adding the energetic contributions described in the previous sections gives the total magnetic free energy:

$$E_T = \int \left[A(\boldsymbol{\nabla} \cdot \boldsymbol{m})^2 - K_{Crys}(\boldsymbol{n} \cdot \boldsymbol{m})^2 - \mu_0 \boldsymbol{M}\boldsymbol{H} - \frac{\mu_0}{2}\boldsymbol{M}\boldsymbol{H_d} \right] dV \tag{2.35}$$

where A is the stiffness constant, $\mathbf{M}$ and $\mathbf{m}$ stand for magnetization and reduced magnetization field vectors, $\mathbf{n}$ is the unit vector in the easy-axis direction, $\mathbf{H}$ is the external field and $\boldsymbol{H_d}$ is the demagnetizing field. The different terms in the integrand are the energetic contributions related to exchange, magnetocrystalline anisotropy, Zeeman energy, and magnetostatic interactions, respectively.

Dimensional analysis of the free energy yields some important length scales of magnetism. For this, three basic quantities are important: the stiffness constant A which has units of J/m (Joule per meter); the magnetocrystalline anisotropy K_{Crys} with units of J/m^3 (Joule per cubic meter) and the magnetostatic self-energy $\mu_0 \mathrm{m}_s^2$ also measured in J/m^3 (Joule per cubic meter) and referenced as K_d in what follows.

The formation of domains can be understood considering the equation of free energy. The magnetostatic self-interaction favors magnetic domains with flux closure but exchange stiffness favors the same direction of the magnetization over the entire sample. The competition between this two energies defines a threshold length (named *Exchange length*, l_{ex})below which exchange interaction prevails over magnetostatic fields (SKOMSKI, 2003).

$$l_{ex} = \sqrt{\frac{A}{\mu_0 M_s^2}} \tag{2.36}$$

Moreover, two domains are separated by thin (but not atomically sharp) domains wall (BLOCH, 1932). Considering a Bloch-wall where the magnetization rotates in a plane parallel to the wall, it is possible to estimate the energy cost of its formation. For a

180-degrees wall, the energy is (SKOMSKI, 2008; HUBERT; SCHÄFER, 2009; COEY, 2010)

$$\gamma = 4\sqrt{AK_{Crys}} \tag{2.37}$$

and its width is

$$\delta_B = \pi\sqrt{A/K_{Crys}} \tag{2.38}$$

From the expression of the Bloch-wall width one can see that the anisotropy (K_{Crys}) favors narrow domain walls. This can be rationalized by the argument that inside the domains the magnetization lies in a favorable direction, but in the wall the magnetization is no longer parallel to the easy axis. On the other hand, narrow walls correspond to large magnetization gradients that are unfavorable from the stiffness point of view. Typical domain-wall widths are 5 nm for hard and 100 nm for soft magnetic materials and domain-wall energies range from 0.1 mJ/m^2 to 50 mJ/m^2 for soft and hard materials, respectively (SKOMSKI, 2008).

Domain-wall formation costs energy. Then, a simple criterion, established by comparing the energies of a sphere with one domain and with two domains, gives a *critical single domain radius*. Domain formation in spheres will therefore be favorable for particles of radius that exceeds this *critical single domain radius* given by:

$$R_{sd} = \frac{36\sqrt{AK_{Crys}}}{\mu_0 M_s^2} \tag{2.39}$$

The value of R_{sd} can vary between few nanometers in soft magnets to about 1 μm in very hard magnets. The derivation of Equation (2.39) involves only the comparison of ground states energies rather than the analysis of hills and valleys of the energy landscape. The application of an external magnetic field may create non-uniform states in single-domain particles.

2.3 Hysteresis and coercive field

Hysteresis is a key feature of magnetic materials and its shape is intimately linked to local energy barriers associated with magnetic inhomogeneities present in real structures. One major challenge in magnetism is to predict the hysteresis behavior from intrinsic parameters such as saturation magnetization and the anisotropy coefficient of the material in connection with the structural properties of samples. The difficulty lies in the nonlinear, nonequilibrium and nonlocal character of hysteresis. The following sections describe simple models that may be used to explain the magnetic behavior of systems.

2.3.1 Stoner-Wohlfarth model

A simple and powerful model is the Stoner-Wohlfarth model (or coherent rotation model). The basic assumption of the model is that the magnetization is constant throughout the magnet, i.e. the exchange energy remains unchanged and the only dependence in energy is due to anisotropy energy. This approximation can be considered valid for systems with small dimensions in units of the exchange length $\sqrt{A/K_d}$.

Let us consider an arbitrary small particle in the single domain regime in which all anisotropic contributions are represented by a single uniaxial effective anisotropy K_{eff}. Its magnetization value is M_S pointing in a direction described by an angle chosen, for simplicity, with reference to the easy magnetization axis as can be seen in Figure 2.11.

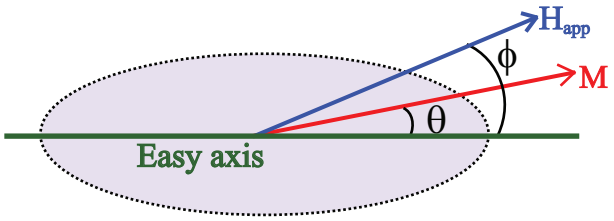

Figure 2.11: Geometry for applied magnetic field, magnetization and easy magnetization axis in the Stoner-Wohlfarth model.

Considering the energetic contributions described in Section 2.2, with the applied field pointing in a direction described by the angle ϕ with respect to the easy magnetization axis, the magnetic free energy of this particle can be written as:

$$E/V = K_{eff} \sin^2 \theta - \mu_0 M_S H \cos(\theta - \phi) \tag{2.40}$$

where V is the volume of the particle.

Analyzing the simplest case where the magnetic field is parallel to the easy axis ($\phi = 0$), the magnetization state is defined by the local minimum of the free energy. From the first and second derivatives of the free energy, it is possible to obtain the value of the applied field for which the reversal of the stable state occurs, named the *switching field*:

$$H_S = \frac{2K_{eff}}{\mu_0 M_S} \tag{2.41}$$

The Figure 2.12 represents the energy landscape for different values of applied magnetic field in units of H_S. For small modulus of the applied field there are two minima at $\theta = 0$ and $\theta = \pm\pi$. Increasing the field magnitude, one minimum shallows and vanishes at a field H_S and depending on the sense of applied magnetic field, only one direction of magnetization is privileged.

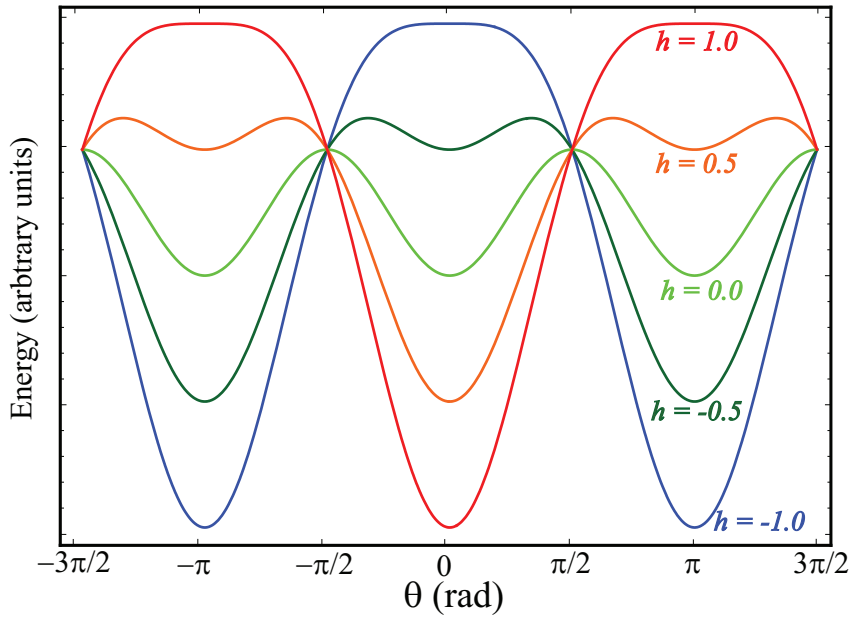

Figure 2.12: Energy landscapes calculated from Equation (2.40) with mathematica software.

One can rationalize the magnetic hysteresis regarding this energy landscape. The Figure 2.13 presents a hysteresis curve for a Stoner-Wohlfarth model and the energy landscape for some values of applied fields. For a saturated state in the positive direction, $H_{app} \geq H_S$, and one has only one minimum. The magnetization is then positive. Decreasing the field, there always exists an energy barrier that forbids the magnetic moment to flip its state to the negative direction up to the point where the applied field is equal to $-H_S$. The magnetic state flips and, in order to return to the positive state, it would be necessary to apply a field $+H_S$. This explanation considers the system under thermal equilibrium at T = 0 K. The thermal effects acting in this

energy landscape will be discussed in further sections.

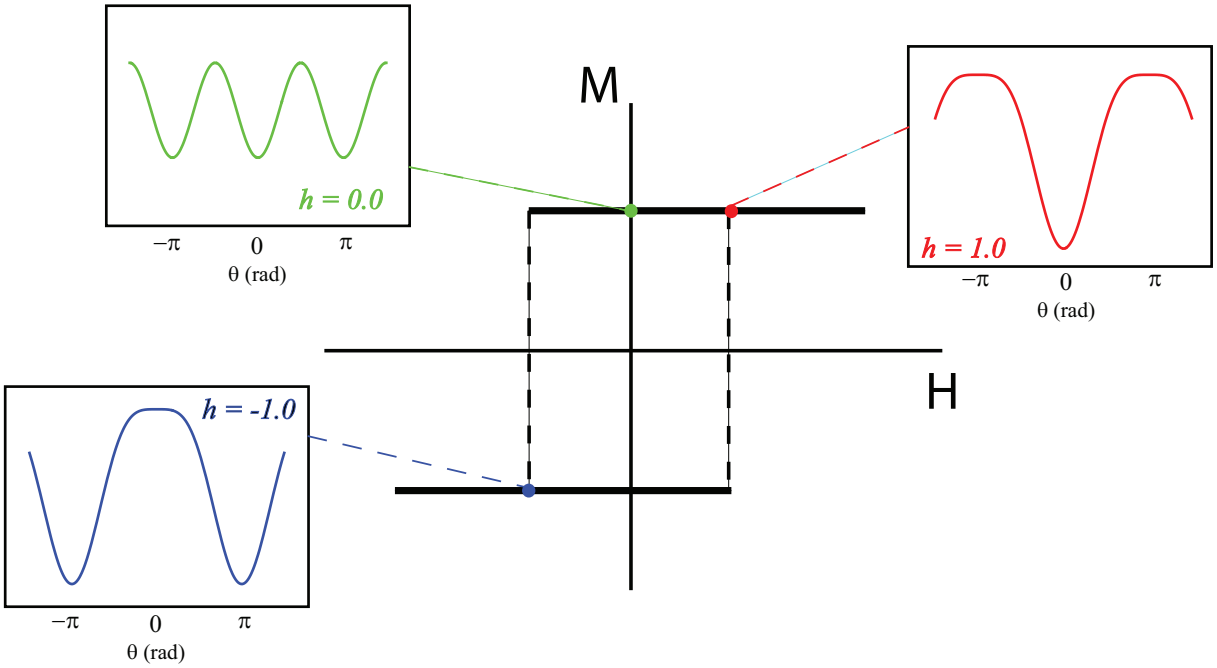

Figure 2.13: Origin of hysteresis in the Stoner-Wohlfarth model with the energy landscapes for some selected applied magnetic field.

From the Stoner-Wohlfarth it is also possible to account for the angular dependence of the applied field. Very often, the magnetic field can be applied in a direction other than the easy axis magnetization. The Figure 2.14 presents simulations performed for different directions of the applied field.

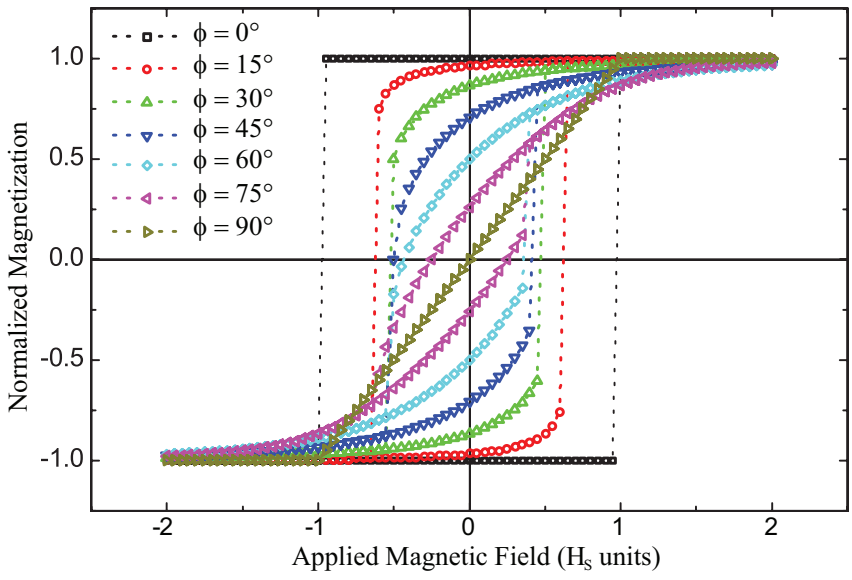

Figure 2.14: Hysteresis for a Stoner-Wohlfarth model for different angles of the applied magnetic field calculated with mathematica software.

The shape of the magnetic hysteresis loop depends on the direction of the applied magnetic field in relation to the easy magnetization axis. For parallel fields, the loop is square with an abrupt transition between the states when $H_{app} = H_S$. For larger angle, some reversible rotation occurs before the transition between states. For the applied field perpendicular to the easy axis, no jump occurs and the magnetization rotates continuously from one direction to the other.

The Stoner-Wohlfarth model is a simple approach useful as a starting point for the description of weakly interacting ensembles of small particles. In macroscopic real magnets structural inhomogeneities and magnetostatic flux closure often dominate the behavior and the predictions of Stoner-Wolfarth model overestimate the coercivity and the loop squareness.

2.3.2 Other reversal mechanisms

There are two basic coercitivity mechanisms, namely *nucleation* and *pinning*. Nucleation refers to the stability of the fully magnetized state in a reverse field while pinning describes the interaction of domain-walls with structural defects.

The nucleation process can be either localized or delocalized. Coherent rotation is delocalized because the magnetization all over the sample is $\boldsymbol{M}(\boldsymbol{r}) = M_S(\theta, \phi)$. Another delocalized reversal mechanism predicted theoretically is the *curling mode*. In curling mode the magnetization tends to form flux closure structures to minimize themagnetostatic energy. The Figure 2.15 presents the two mechanisms for an ellipsoid of revolution.

The coherent reversal (Stoner-Wohlfarth model, explained in the previous section) is energetically favorable only for very small defect-free particles. In such kind of system, it is expected that at the *nucleation field* equal to H_S, the magnetization state becomes unstable and the magnetization coherently flips to a new stable position.

With increasing size, the nucleation mechanism in perfect ellipsoids changes from coherent reversal to curling mode that presents a flux closure. This mode costs exchange energy but is magnetostatically favorable due to the flux closure. Both coherent rotation and curling greatly overestimate the coercivity of most magnetic materials as illustrated in Figure 2.16.

The strong disagreement observed in theoretical predictions can be explained by considering localized nucleation due to imperfections. The real structure of magnet

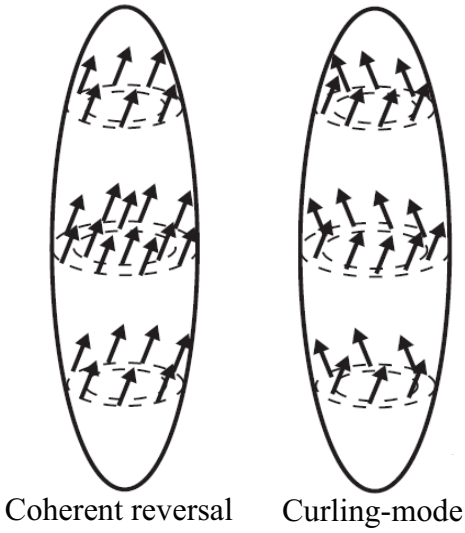

Figure 2.15: Representation of coherent and curling magnetization reversal modes in a prolate ellipsoid.

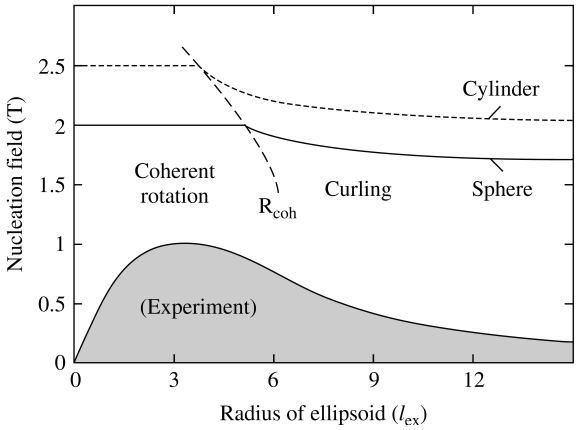

Figure 2.16: Nucleation field calculated considering delocalized nucleation in a sphere (solid line) and in a cylinder (dotted line) compared to experimental results. The dashed line is a guide separating coherent rotation from curling (Reprinted from (SKOMSKI, 2008)).

might contain defects, textures or grain boundaries. A localized reversal, in the vicinity of defects, costs exchange energy but is favorable from the anisotropy point of view, because it exploits local anisotropy minima. The magnetic behavior is then strongly linked to structural inhomogeneities present in macroscopic samples.

2.4 Temperature and time scale effects

Analyzing the origin of magnetic hysteresis as the consequence of local minima in the energy landscape, there will be energy barriers acting on the magnetic moment and preventing its rotation between two adjacent minima. Independently of the mechanism of reversal privileged by the free energy configuration, these energy barriers can be crossed by thermally activated process. This is why the magnetic hysteresis is a non-equilibrium process and hence it is time dependent. In a good approximation, the thermal excitation over energy barriers is described by the Arrhenius or Néel-Brown law(BROWN, 1963):

$$\tau = \tau_0 \exp\left(\frac{E_a}{k_B T}\right) \tag{2.42}$$

where E_a is the activation energy associated with the energy barrier and τ_0 is the inverse of an attempt frequency of the order of 10^{-11} s. This equation is a non-equilibrium analog of the Boltzmann factor $\exp(-E/k_B T)$.

Inverting (2.42) yields the energy barrier accessible after some waiting time t:

$$E_a = k_B T \ln\left(\frac{t}{\tau_0}\right) \tag{2.43}$$

This thermal activation will affect the behavior of magnetic materials as a function of time and temperature. The following section will describe these effects. The thermal activation gives rise, for sufficiently small Stoner-Wohlfarth particles, to a behavior named superparamagnetism.

2.4.1 Superparamagnetism

Let us consider a particle mono-domain with an effective anisotropy constant K_{eff} in the absence of applied field. The energy can then be written as $E_a = K_{eff} V \sin(\theta)$, where V is the volume of particle and θ is the angle between its magnetization and its easy magnetization axis. The particle has then two minima separated by an energy barrier of height $K_{eff} V$. If the value of the energy barrier is comparable with the thermal energy of the bath, the system presents superparamagnetism. The Figure 2.17 presents the energy landscape for this situation.

In this small particles in which the activation energy is of the order of $k_B T$ the magnetization fluctuates due to thermal excitation. A measure of the magnetic state will take a time τ_m depending on measurement technique. The comparison of the

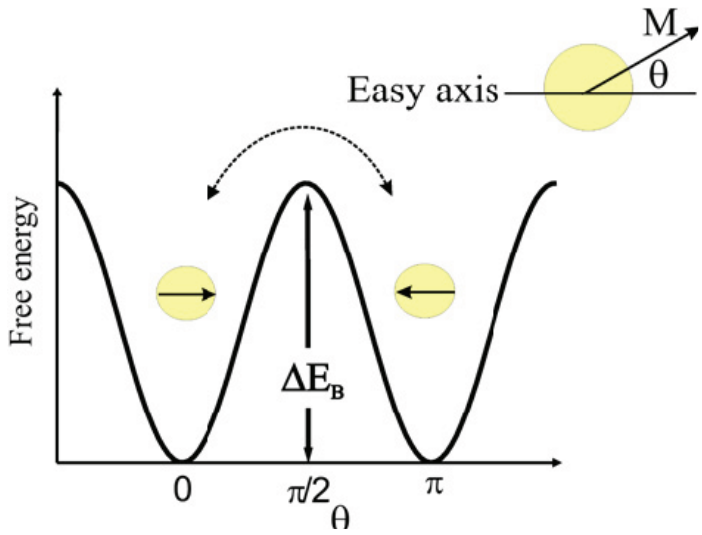

Figure 2.17: Origin of hysteresis in the Stoner-Wohlfarth model with the energy landscapes for some selected applied magnetic field. (Reprinted from (BEDANTA; KLEEMANN, 2009))

measurement time and the activation time of the particle defined by the Néel-Brown law (Equation (2.42)) will cause the superparamagnetism. This phenomena generally occurs for magnetic clusters embedded on a non-magnetic matrix.

The superparamagnetic system presents two magnetic states: *blocked* and *superparamagnetic*. A transition between two states is observed in the systems at a temperature named *blocking temperature* (T_B). For temperatures higher than T_B, the magnetization flips over the two minima faster than the measuring time. The magnetization then behaves as an paramagnetic material with a huge magnetic moment due to the large number of atoms in the magnetic cluster. For temperature below T_B the magnetic state is stable in time. Is important to stress then that the definition of the superparamagnetic state implies the definition of a measuring time.

The Figure 2.18 presents the typical set of experimental data on superparamagnetic systems. The principal graph present the magnetization as a function of temperature in procedures Zero Field Cooling (ZFC) and Field Cooling (FC). The ZFC curve present a peak that defines T_B. In the detail is presented the magnetization in function of the magnetic field for two temperatures, one above other below T_B. Below T_B the system present hysteretic behavior and above the system present a paramagnetic-like behavior and the magnetization behavior can be explained with the Langevin equation.

The ZFC procedure consists in warming the sample to a temperature higher than the transition to the disordered phase in the absence of applied magnetic field. After that,

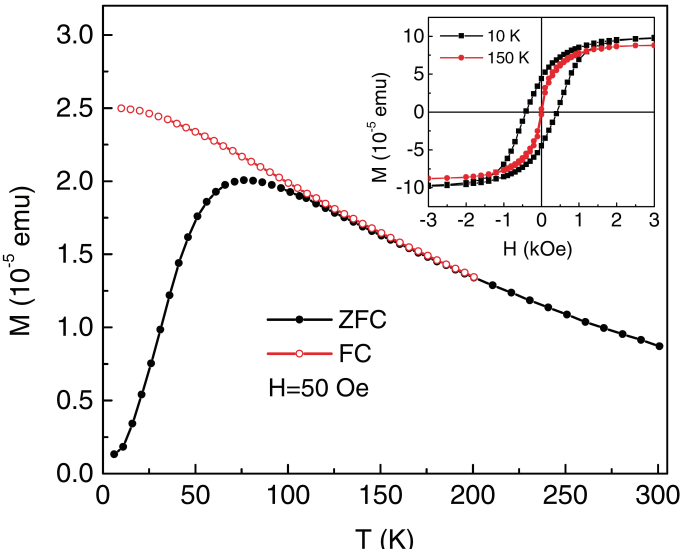

Figure 2.18: Origin of hysteresis in the Stoner-Wohlfarth model with the energy landscapes for some selected applied magnetic field. (Reprinted from (SUN et al., 2003))

the sample is cooled down to the lowest temperature still in the absence of magnetic field. At a given temperature a low field is applied and the magnetization behavior is measured raising the temperature (in a moderate rate of raising temperature). The FC procedure is similar, but the cooling process is performed with the applied magnetic field. In most cases, the FC process is reversible and can be performed after the ZFC process, measuring the magnetization while cooling down the sample with the same applied magnetic field.

For typical experiments, the time scale t is about 100 s. Comparing the activation time of the particle (Equation (2.42)) with this time of measurement one concludes that magnetization reversal occurs for energy barriers up to $25k_BT$ while local minima with energy barriers larger can be considered frozen. It is also possible to express the *blocking temperature* of the given system as:

$$T_B = \frac{K_{eff}V}{25k_BT} \tag{2.44}$$

This theoretical prediction can be compared with blocking temperature determined through curves ZFC. The equation can also be inverted and used to estimate the volume of particles $V_{Crit} = \frac{25k_BT}{K_{eff}}$ from the blocking temperature measured or, if this volume is known by some other method (as Transmission Electron Microscopy for example), is possible to estimate the anisotropy constant and then compare it with its bulk value.

2.4.2 Temperature dependence of the coercivity

The energy barrier that must be overcome by the magnetic moment depends on the applied magnetic field: if the field is sufficiently high then the magnetic moment can be reversed and E_a is overcome. This dependence of the activation energy on the external magnetic field is accounted for by the following phenomenological expression:

$$E_a(H) = KV\left(1 - \frac{H}{H_S}\right)^m \tag{2.45}$$

where K is the magnetic anisotropy of the system, H_S is the switching field and V is the switching volume.

In the case of aligned spherical Stoner-Wohlfarth particles, the exponent is m=2 (STONER; WOHLFARTH, 1948). This exponent is indeed valid for symmetric energy landscapes. For most magnetic systems having a real structure departing from such ideal situation, such as polycrystalline nanowires for example, m=3/2 (SKOMSKI, 2003; FRUCHART; THIAVILLE, 2005).

Combining Equations (2.42) and (2.45) gives the dependence of the switching field, H_S, on the temperature (SHARROCK, 1994):

$$H_S = H_0\left[1 - \left(\frac{k_B T \ln(\tau/\tau_0)}{KV}\right)^{1/m}\right] \tag{2.46}$$

Such behavior has often been observed for coercive field of ensembles of nanoparticles and also nanowires assemblies.

2.4.3 Time dependent reversal: magnetic viscosity

The study of the time dependence of magnetization is also an important tool to understand the behavior of magnetic systems. Considering a sample saturated in the positive sense, at a given time $t = 0$ a reversal field H_{rev} is applied. Then the magnetization dependence with time can be written as:

$$M(t) = -M_S + 2M_S \exp\left(-t/\tau^*\right) \tag{2.47}$$

where τ^* is given by Eq. (2.42) with E_a dependent on the applied reversal field.

This behavior can be found for systems having a single activation energy following the thermal activation described by the Neel-Brown model. Nevertheless, for real multi-

particle systems, it is hard to obtain such a behavior. In these real systems, a distribution in size and structural properties is generally present and it gives origin to a distribution of activation energies. It is then necessary to integrate on this activation energy to obtain the behavior for this kind of system. Considering $P(E_a)dEa$ the number of particles with energy barrier between E_a and $E_a + dEa$, the time dependence of the magnetization can be written as:

$$M(t) = -M_S + 2M_S \int_{-\infty}^{\infty} P(E_a) \exp\left((-t/\tau^*) \exp\left(\frac{-E_a}{k_B T}\right)\right) dE_a \tag{2.48}$$

Concerning only the integral, one has then:

$$I = \int_{-\infty}^{\infty} P(E_a) \exp\left((-t/\tau^*) \exp\left(\frac{-E_a}{k_B T}\right)\right) dE_a \tag{2.49}$$

From the relationship exp(ln(A))=A:

$$I = \int_{-\infty}^{\infty} P(E_a) \exp\left(-\exp\left(\ln\left(t/\tau^*\right)\right) \exp\left(\frac{-E_a}{k_B T}\right)\right) dE_a \tag{2.50}$$

$$I = \int_{-\infty}^{\infty} P(E_a) \exp\left(-\exp\left(-\frac{E_a - k_B T \ln\left(t/\tau^*\right)}{k_B T}\right)\right) dE_a \tag{2.51}$$

Looking carefully to the double exponential term in this integral, it is possible to simplify this expression. Figure 2.19 presents the behavior of this double exponential for various values of $k_B T$ and of the activation energy. The product $k_B T \ln\left(t/\tau^*\right)$ only shifts the behavior in the activation energy axis and was then fixed.

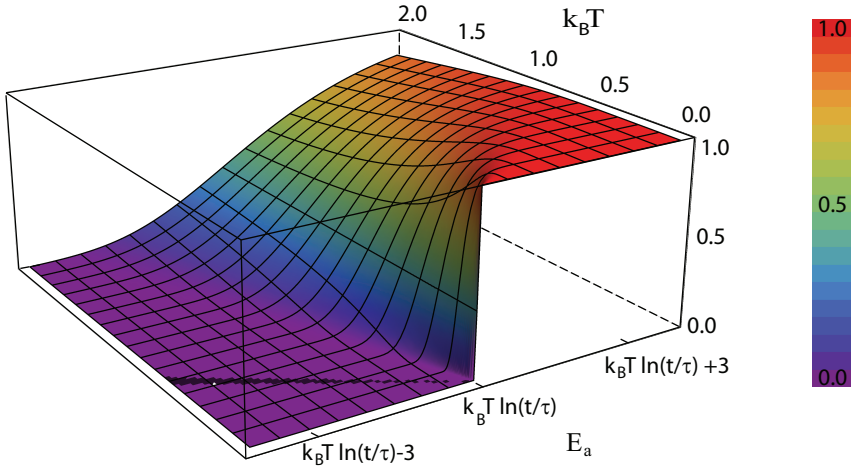

Figure 2.19: Behavior of the double exponential function as a function of the activation energy and of $k_B T$. For low values of $k_B T$, the exponential can be approximated as is explained in the text.

It can be seen in the graph that for low values of k_BT, the exponential behaves as a step function varying abruptly from 0 to 1 when the activation energy reaches a value given by: E_a=$k_BT\ln(t/\tau^*)$. Indeed, it is possible to take advantage of this approximation for magneto-viscosity problems, where k_BT is small compared with the activation energies. Using the approximation of a Heaviside step function ($\Theta(x)$), one gets:

$$I = \int_{-\infty}^{\infty} \Theta(E_a - k_BT\ln(t/\tau^*))P(E_a)dE_a \tag{2.52}$$

$$I = \int_{k_BT\ln(t/\tau^*)}^{\infty} P(E_a)dE_a \tag{2.53}$$

It is then possible to change the integral limits using:

$$\int_{-\infty}^{\infty} f(x)dx = \int_{-\infty}^{\xi} f(x)dx + \int_{\xi}^{\infty} f(x)dx \tag{2.54}$$

Then:

$$I = \int_{-\infty}^{\infty} P(E_a)dE_a - \int_{-\infty}^{k_BT\ln(t/\tau^*)} P(E_a)dE_a \tag{2.55}$$

The first integral, by normalization of the activation energy distribution, is equal to one. For the second integral, the negative energies correspond to the particles with instantaneous reversal with no waiting time. That means that these particles have already flipped their magnetization to the new state. Considering that these particles would not return to the previous state, we can then perform the integral considering only positive energies.

$$I = 1 - \int_{0}^{k_BT\ln(t/\tau^*)} P(E_a)dE_a \tag{2.56}$$

Considering that the width of the distribution of activation energies is higher than $k_BT\ln(t/\tau^*)$ one can approximately consider a constant value for $P(E_a)$ in the interval of integration. This approximation can be better visualized graphically as presented in Figure 2.20. The green box has a width of $k_BT\ln(t/\tau^*)$ in activation energy and the approximation for $P(E_a)$ constant in the interval neglects only a small part of the integral (red area).

Using the approximation of $P(E_a)$ constant, one gets:

$$I = 1 - P(0)k_BT\ln(t/\tau^*) \tag{2.57}$$

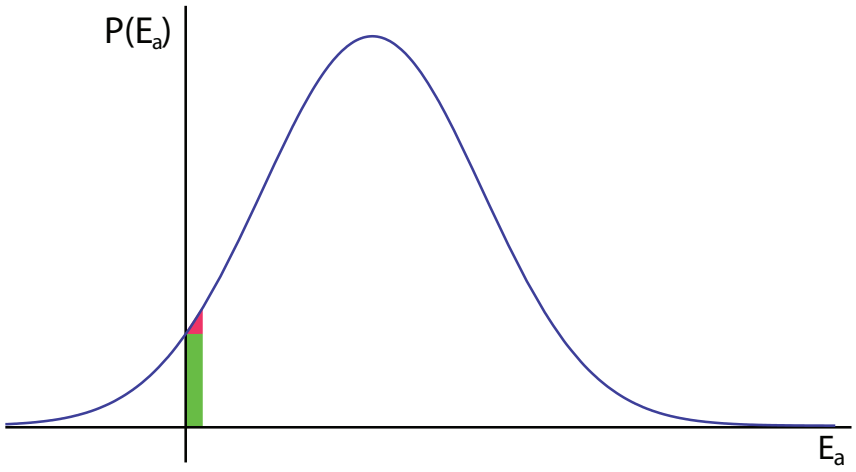

Figure 2.20: Scheme for the activation energy distribution dependence on energy and the approximation explained in the text.

Substituting (2.57) on Equation (2.48):

$$M(t) = -M_S + 2M_S(1 - P(0)k_BT\ln(t/\tau^*)) \tag{2.58}$$

$$M(t) = M_S - 2M_SP(0)k_BT\ln(t/\tau^*) \tag{2.59}$$

Writing $S = 2M_SP(0)k_BT$, on gets:

$$M(t) = M_S - S\ln(t/\tau^*) \tag{2.60}$$

The asterisk in τ in the previous approximations means that the characteristic reversal time depends on the applied field. One can assume instead this variation in the viscosity coefficient. Then:

$$M(t) = M(t_0) - S(H,T)\ln(t/\tau_0) \tag{2.61}$$

where $S(H,T)$ is the magnetic viscosity coefficient (SKOMSKI, 2003; GAUNT, 1986) that depends on the temperature and on the external magnetic field.

Therefore, for an ideal system composed of identical magnetic objects having the same activation energy, Equation (2.47) would explain the exponential decay of the magnetization with time, following a reversal of the external magnetic field. Such a behavior is rarely observed in real systems owing to structural inhomogeneities. This dispersion inherent to real structure does not generate a single energy barrier to cross but instead a continuous distribution, $P(E_a)$. Averaging over such distribution gives the logarithmic law for the magnetization decay. Indeed, the approximations made

previously are confirmed by the linear behavior of magnetization as a function of $\ln(t)$ for large time scales.

From this approximation, the viscosity can be related to the distribution of barriers as can be seen from $S = 2M_S P(0) k_B T$. Thus, S varies linearly with the temperature provided that M_S is constant and that the distribution of activation energies does not depend on the temperature. For the simplest model, supposing a rectangular distribution of energy barriers of width ΔE_a, modeling a broad and smoothly varying distribution, it can be shown that (SKOMSKI, 2003):

$$S = \frac{2k_B T M_s}{\Delta E_a} \tag{2.62}$$

Magnetic viscosity measurements are also interesting because it is possible to extract from them valuable information on the localized or delocalized nature of the reversal by extracting from magnetic measurements the activation volume involved in the process. An activation volume smaller than the physical size of the magnetic system is a clear fingerprint of a localized reversal. This activation volume can be defined as (STREET; WOOLLEY, 1949):

$$\mu_0 M_s V^\star = \frac{-\partial E_a}{\partial H} \tag{2.63}$$

Using Equations (2.45) and (2.46), the following expression $V^\star$ can be deduced:

$$V^\star = \frac{m}{2} V^{1/m} \left[\frac{k_B T}{K} \ln(\tau/\tau_0) \right]^{(m-1)/m} \tag{2.64}$$

The activation volume can be extracted from experiments measuring S and the irreversible part of the susceptibility χ_{irr}. Indeed, the magnetic viscosity can also be expressed as (GAUNT, 1986):

$$S = \frac{-k_B T \chi_{irr}}{(\partial E_a / \partial H)} \tag{2.65}$$

The name irreversible comes from a convention and it stands for field variation of the energy landscape. To rationalize this term convention let us assume a given energy barrier distribution arising from a distribution of effective anisotropies. At a given temperature T, the system has a given probability of crossing this barrier. Changing the magnetic field, each barrier changes and the probability of finding the system in a given state also changes. Performing usual hysteresis curves, the field is decreased sequentially from saturation to the measured field and at a given field H, the state of the system depends on its field but also on the field and time spent on each previous applied field (otherwise

speaking, on magnetic history). This way, the probability of finding the system in a given state depends on the field and magnetic history of the system. Another methodology, called remnant hysteresis loops, saturates the magnetization of the sample before each measurement. This way, the variation of the magnetization does not contain any time-dependent part related to thermally activated reversal (decay). The term irreversible express the fact that field-induced changes of the energy distribution lead to irreversible changes of the magnetization. Therefore, using Equation (2.63), the activation volume as a function of S and χ_{irr} reads:

$$V^{\star} = \frac{k_B T \chi_{irr}}{\mu_0 M_s S} \tag{2.66}$$

Thus, experimental values of $V^{\star}$ extracted from magnetic viscosity measurements using Equation (2.66) can be compared to Equation (2.64).

2.5 Magnetism in nanowires

Nowadays, there is a huge interest in studying nanomaterials due to their potential applications in diverse fields. The reduction of dimensions results in the modification of the materials properties and the control of these new properties may lead to applications. Specifically talking, ferromagnetic nanowires (FNW) have attracted much attention in scientific research (LI et al., 1999; SUN et al., 2000). Such kind of materials may be used in application in ultrahigh density magnetic storage devices. Also, from a more fundamental perspective, these objects offer an ideal testing ground for mechanisms of magnetization reversal in nanostructures because their dimensions fall in the range of magnetic lengthscales such as the *exchange length* and the *domain wall width* (SKOMSKI, 2003; GUIMARÃES, 2009).

Recently, a variety of methods has been applied in the fabrication of nanowires, as for example: chemical methods (UNG et al., 2007), electron-beam lithography (JUHASZ; ELFSTRM; LINNROS, 2005; TONG et al., 2009), use of vicinal surfaces as templates (ZACH; NG; PENNER, 2000; CHUNG et al., 2009), use of the vapor-liquid-solid (VLS) mechanism (WU; YANG, 2001; SONG; PARK; PAIK, 2010). Despite the several existing techniques, most of the studies of FNW were performed on arrays grown by electro-deposition into self-assembled porous alumina templates (SUN et al., 2005; HAN; SHAMAILA; SHARIF, 2010) since this technique is simple, effective, versatile and low cost(HAN; SHAMAILA; SHARIF, 2010). In this method, an assembly of ferromagnetic nanowires is electro-deposited into a self-assembled porous anodic alumina template.

This template has a quasi-hexagonal array of pores with diameters varying from 6 nm to 100 nm, lengths of about 1 μm and variable center to center spacing of the order of 50 nm.

2.5.1 Reversal mode as a function of the diameter

The magnetic properties of transition metals nanowires electro-deposited into self-assembled porous anodic alumina templates where studied by Skomskiet al. in the early 2000s (SKOMSKI et al., 2000; ZENG et al., 2002; SELLMYER; ZHENG; SKOMSKI, 2001). These studies concentrated on very small diameters ranging from 6 to 60 nm. As expected, the properties of the nanowires are governed by their shape anisotropy with a square cycle in the direction parallel to the FNW axis and close sheared cycles perpendicular to this axis.

Figure 2.21 presents the dependence of the coercive field (for field parallel to the FNW) with the length for Co nanowires and also the dependence of the extrapolated coercive field at T= 0 K for FNW of Fe, Co and Ni with the nanowire diameter. The figure is presented in cgs units as the original reference but in the discussion SI units will be used.

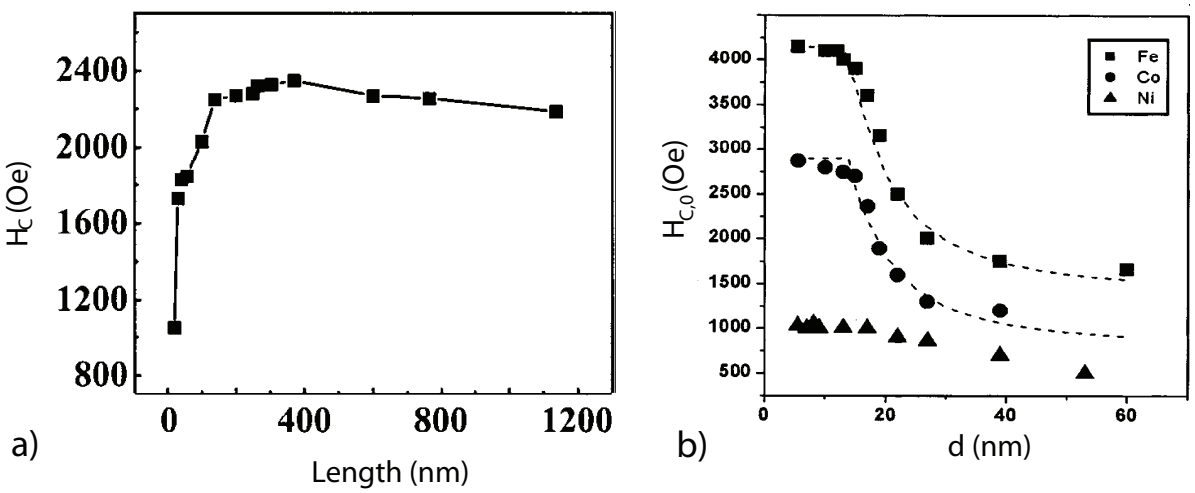

Figure 2.21: Results from Fe, Co and Ni FNW. In (a) the dependence of coercive field with the length for Co nanowires and in (b) the dependence of the extrapolated coercive field at T= 0 K for FNW of Fe, Co and Ni with the nanowire diameter (adapted from (SELLMYER; ZHENG; SKOMSKI, 2001; ZENG et al., 2002))

The coercivity depends strongly on the nanowires length(l), first increasing rapidly and then approaching saturation when $l/d = 5$. The dependence of the coercive field with the diameter of the objects (Figure 2.21(b)) presents a critical diameter where a transition

is observed. Below this critical diameter $H_{c,0}$ remains nearly constant while above it $H_{c,0}$ decreases monotonically. The critical diameter is the threshold diameter for transition between *curling* and *coherent reversal*. The theoretical diameters for this transition in Fe, Co and Ni are 12, 15 and 27 nm, respectively. The values found in the original work are quite near these values (13.8 nm for Fe and 14.5 for Co).

However, the value of the coercive field below the critical diameter is not what would be expected from anisotropy values. Supposing an infinite cylinder, the theoretical anisotropy field is $\mu_0 H_S = \mu_0 M_S/2$. Hence for Fe, Co and Ni the values are 1.1, 0.88 and 0.34 Tesla, respectively. The measured coercive fields are roughly one third of these values. Sellmyer et al. considered that this disagreement comes from localization in the reversal mechanism due to imperfections in the nanowires. In another work (SKOMSKI et al., 2000) the authors present a model on how morphological inhomogeneities present in FNW can cause a localization of the reversal. Figure 2.22 presents a scheme of the nucleation of the reversal in the vicinity of a defect in a wire.

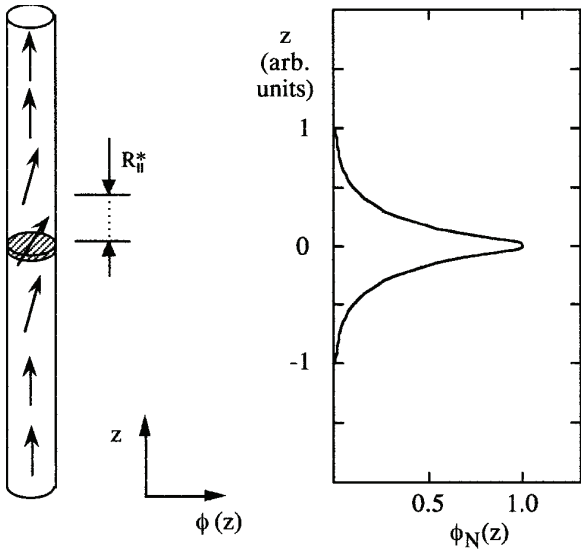

Figure 2.22: Nucleation mode localization in a nearly single crystalline wire. The dashed area is the perturbed region and, after nucleation, the magnetization reversal proceeds by propagation of domains walls (Reprinted from (SKOMSKI et al., 2000)).

The localization is a common phenomenon in nanowires caused by structural features such as polycrystallinity, wire thickness fluctuations, defects or impurities. The model of Skomski et al. allows them to explain the small activation volumes (much smaller than the physical volume of the wire) derived from viscosity measurements in long wires.

2.5.2 Dipolar interactions

Nielsch (NIELSCH et al., 2001) reported a study of electrodeposited Ni FNW systems having a constant inter-wire distance while the diameter of the wires was varied. They observed a deep change of the hysteresis loops when the diameter was changed from 55 to 30 nm. For high diameter, the hysteresis loops do not present any preferential orientation with a coercivity of 0.06 T and a normalized remnant magnetization of 30 %. For 33 nm diameter, the system clearly presents an easy axis parallel to the nanowire axis with a coercivity of 0.12 T and a normalized remnant magnetization of 98 % in this direction. Hertel (HERTEL, 2002) has simulated hexagonal arrays of nanowires mimicking Nielshs samples and showed that the coercivity decreases with increasing the density of nanowires in the system.

This result indicates that the dipolar interactions between the nanowires affect the magnetization state inside the wires and can even change the anisotropy of the system, with an easy plane perpendicular to the FNW axis. Vázquez et al. (VÁZQUEZ et al., 2004) suggested that the interaction between the nanowires is related with the ratio of their diameters over the distance between their centers. Encinas-Oropesa expressed the effects of the dipolar interaction as a function of the porosity of the system, that is the volume fraction occupied by the wires (ENCINAS-OROPESA et al., 2001).

3 Experimental techniques

This chapter introduces the principal techniques used in this study. The chapter begins with an introduction to Pulsed Laser Deposition (PLD), the technique used to elaborate the samples. The structural properties of the thin films produced were investigated by X-ray diffraction, Transmission Electron Microscopy (TEM) and X-ray Absorption Spectroscopy (XAS).

PLD growth and X-ray diffraction were performed at Institut des NanoSciences de Paris (ISNP - Paris - France) under the supervision of Yunlin Zheng and Franck Vidal, with the assistance of Dominique Demaille. TEM experiments were carried out by Dominique Demaille at the microscopy facilities of the Institut de Minéralogie et de Physique des Milieux Condensés (IMPMC Paris -France). X-ray absorption spectroscopy was performed at the SAMBA beamline of Synchrotron SOLEIL (St Aubin - France) in collaboration with Emiliano Fonda who has also performed the simulation of the results.

The chapter also contains brief descriptions of SQUID magnetometry, including the measurements procedures used, and of the Ferromagnetic Resonance (FMR) technique and its application to thin films containing a FNW assembly. I performed the SQUID measurements at INSP and at Grupo de Supercondutividade e Magnetismo - GSM of Universidade Federal de São Carlos (UFSCar) under the supervision of Adilson J. Ap. de Oliveira. The FMR measurements were performed at Instituto Balseiro (San Carlos de Bariloche - Argentina) under the supervision of Juliàn Milano.

3.1 Pulsed laser deposition

The technique used for the growth of thin films was Pulsed Laser Deposition (PLD). This technique consists in evaporating a material from a target by means of the energy furnished by a pulsed laser. A typical PLD setup is composed of a pulsed laser and a growth chamber in which targets and substrate are kept under specific conditions of temperature and pressure (EASON, 2007). The Figure 3.1 presents the typical scheme of a PLD setup with the laser specification used to produce the samples.

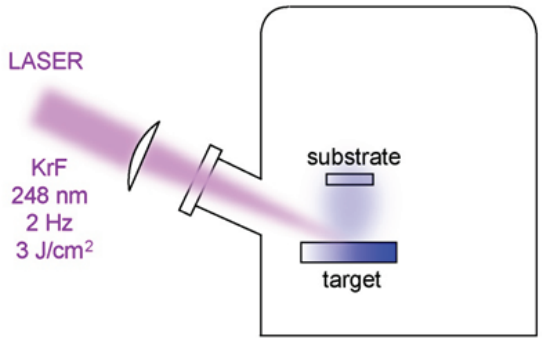

Figure 3.1: Scheme of deposition with pulsed laser deposition.

Despite the moderate average power (of the order 1 W) used in the technique, a high instantaneous power (between MW and GW) can be achieved due to the pulsed character of the laser (pulse duration from 100 fs to a few ns, depending on the laser). This high power causes evaporation and partial ionization of the target's material (EASON, 2007). The resulting plasma is called the plume. It contains atoms, molecules, electrons, ions and even agglomerate solid particles can be formed, depending on the delivered energy. Generally, the solid agglomerates are avoided since they cause loss in the crystalline quality of the deposited thin films. This plume is dense and strongly directed, expanding in a direction perpendicular to the target surface due to the temperature and electric repulsion effects.

The substrate is kept at a distance of the target in a way to receive the matter of the plume generated by the laser. The matter arrives with a kinetic energy from the plasma and extra energy can be furnished by the substrate temperature. The substrates temperature influences the diffusion length of atoms on the surface and thus plays an important role in the crystalline quality of the thin film. Generally, a high substrate temperature enables a better crystalline quality (CHRISTEN; ERES, 2008).

Besides the substrate's temperature, the atmosphere of chamber is also an important adjustable parameter of the growth (WILLMOTT, 2004). The atmosphere interacts physically with the plume, controlling the rate of matter arriving at the substrate. Furthermore, the atmosphere can also interact chemically with ions, changing their valence, or even reacting with ions and producing other materials. For oxides as an example, the growth is generally assisted by a controlled oxygen atmosphere in order to keep the desired stoichiometry (CHRISTEN; ERES, 2008).

The PLD technique is generally used for the preparation of materials with complex composition, principally oxides, because the growth method permits to maintain the target's stoichiometry in the growing film. Another advantage of PLD is the ability to easily evaporate all materials and the absence of electronic or mechanical connections with the targets allowing their easy storage, manipulation and replacement in the chamber. Among the disadvantages of the technique, one can cite the ejection of debris and droplets from the target at high laser power, the small surface of the thin films produced (typically 1 cm^2) and the low growth rates (of the order of Å per second), and last but not least, the non-scalability (WILLMOTT, 2004).

3.2 Transmission electron microscopy

Transmission electron microscopy (TEM) is an important technique for studying the structure, the morphology and the chemical composition of nanostructured materials and thin films. The basic principles of an electron microscope are the same as an optical microscope but as the wavelengths of electrons are shorter than visible light the electron microscope have much better resolutions (of the order of the Å). Such resolution permits the study of crystallographic structure at the atomic scale (REIMER; KOHL, 2008).

In a TEM microscope, an electron flux is generated and collimated in a very thin beam by the use of magnetic lenses. This high energetic electron beam then passes through a thin sample, interacts with the matter and - as the result of these interactions - information about the structure of the sample is obtained. The information can be projected on a fluorescent screen or be digitalized in a CCD camera. The Figure 3.2 presents the scheme of a typical TEM microscope.

Different operation modes are available in TEM microscopes by changing the lenses' strength or selecting either the transmitted or the diffracted beam. These modes may be used to extract information that is of particular interest to the investigator. In this thesis,

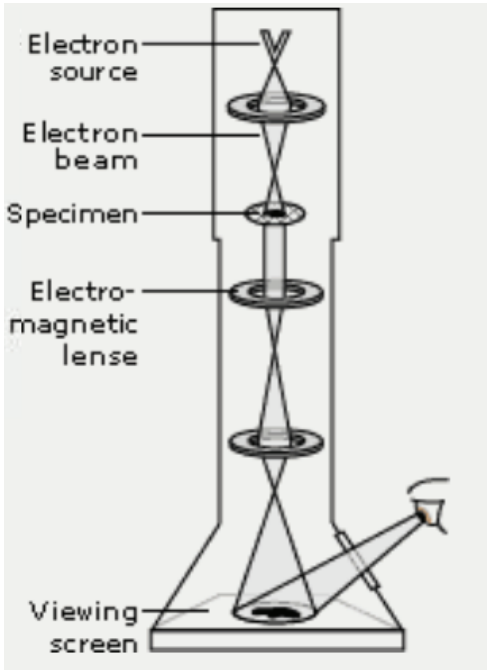

Figure 3.2: Scheme of a transmission electron microscope (adapted from http://www.nobelprize.org/educational/physics/microscopes/tem/index.html).

four of them were used and are briefly described in what follows:

HRTEM - High-Resolution Tunneling Electron Microscopy The electron beam is diffracted by atomic planes of a crystalline structure in a small selected area. This permits local characterization of the sample structure. In this technique, the resultant image is a pattern of interference between transmitted and diffracted electrons by the material. This pattern matches the crystallographic structure of the sample in real space, allowing one to obtain images of the crystallographic structure at the atomic scale. In this mode, it is possible to choose between two options *Dark Field* (only the diffracted electron beam is selected) and *Bright Field* (both diffracted and transmitted beam are selected).This permits to enhance the contrast between different materials.

SAED - Selected Area Electron Diffraction SAED and HRTEM are complementary techniques that give information about the crystallographic structure of the sample. To change between them, the intermediate lens of the TEM microscope is focused at different positions: for HRTEM, the focus is on the first image plane (defined by the objective) while for SAED the focus is the back focal plane of the objective (RODENBURG, 2004).

EELS - Electron Energy loss Spectroscopy When the electronic beam passes

through the sample, it loses energy due to inelastic scattering in the material (REIMER; KOHL, 2008). A channel of inelastic scattering of particular interest is inner-shell ionization of elements present in the sample. In this case, the energy loss of the beam will correspond to the energy of a particular electronic transition, characteristic of the element present in the sample. Therefore, this spectroscopic technique can be used to probe the chemical composition of a sample at the nanoscale. In order to obtain such information, a prism spectrometer (made of multipoles) is placed after the image plane and the electrons are projected on a CCD array (EGERTON, 2009). Figure 3.3 presents a scheme of the spectrometer separating the electrons by energy loss.

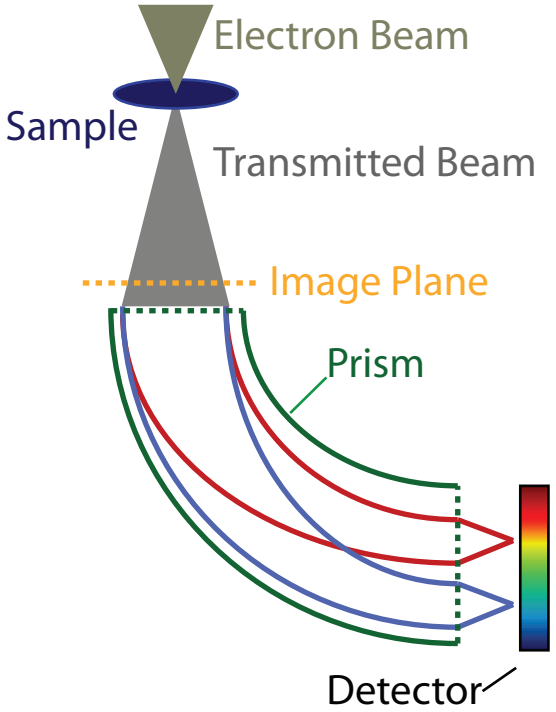

Figure 3.3: Scheme of a prism spectrometer that filters the electrons as a function of their energy loss. In the scheme, the image plane is where the HRTEM image is formed.

The analysis of the energy loss can be separated in regions of energy. The first peak appearing is the zero-loss peak and it is the most intense one. It is related with electrons that have no interaction with the sample or interact only elastically. The low loss region contains the plasmon losses and interband transitions and are characterized by $\Delta E \leq 50$ eV. At high energy losses ($\Delta E \geq 50$ eV) the inner-shell electron of materials are ionized and these peaks are used in elemental analysis. The higher the energy of the level, the smaller the probability of the ionization process, hence, in this region, the peaks are less intense (EGERTON, 2011). Typically, energies of the order of hundreds of electron volts can be probed in TEM microscope.

For example, transitions at the L-edge of transition metals can be probed.

EFTEM - Energy Filtered Tunneling Electron Microscopy Taking profit of a spectrometer and of the spatial resolution of the TEM, it is also possible to select an elements energy and obtain a chemical cartography. The process consists in taking three TEM images considering only the electrons that lose energy in a narrow range (usually 20 eV). Two energies are chosen just below the ionization edge of the element. An average is made on these first two images to evaluate the background. This background is then subtracted from the third image taken at energies just beyond the edge. In the resultant image, brighter regions indicate higher concentration of the chosen element. For this study, energies near the Co L-edge (780 eV) were selected in filtered TEM images presented in section 4.2.4.

The contrast in the images of a TEM microscope is profoundly dependent on the thickness of the sample. In order to obtain images with a reasonable contrast, the thickness must be typically of the order of a few tens of nanometers. A special procedure is needed to obtain a homogeneous piece of sample of this thickness. The procedure consists in:

1. **Choose the geometry** The preparation of the samples starts by the definition of the geometry of the measurement. In this study, two geometries were probed: cross section and plane view. In cross section, the (100) plane of the $SrTiO_3(001)$ substrate is imaged and in plane view, the growth plane is probed (the film surface).

2. **Mechanical polish** After cutting a piece in the appropriate geometry, the piece is fixed into a grid and a mechanical polish is performed using a powder of aluminum oxide (grain size in the micrometer range) in suspension in water in order to exfoliate the sample down to a thickness of approximately 100 μm

3. **Ions milling** The sample is then transferred to the argon ions milling equipment (Gatans Precision Ion Polishing System, TM). This equipment directs two beams of Ar ions in a low-angle with respect to the film plane while rotate the sample in order to produce a small hole in the sample. After this procedure, a region of growing thickness is observable near this hole. This region can be imaged in the TEM microscope.

3.3 X-ray absorption spectroscopy

X-ray absorption (XAS) is a technique that can give information on the electronic structure of matter. The basic principle consists in directing a monochromatic X-ray wave at the sample and measuring its absorption as a function of the energy of the beam. The technique requires an intense and tunable X-ray beam. Such experiment is usually performed at synchrotron sources.

The energy absorbed by the sample causes electronic states transition and the energies at which a transition occurs is characteristic of the material probed. This gives to the technique an elemental sensibility. Hence, the technique enables the determination of the electronic structure of each element present in a sample separately.

The X-ray interacts with the materials, causing transition of electrons from the core levels to unoccupied excited states. After the transition, a process is necessary in order to liberate the energy absorbed by the material. Then a photon is emitted or a photo-electron can be generated. This permits different detection system for the technique: transmission, fluorescence, and electron yield mode. The first is based on the difference of intensity of the incident and transmitted beams; the fluorescence mode is based on the measurement of the emitted photons; and the electron yield mode measures the quantity of photoelectrons generated by the absorption.

A XAS spectrum can be divided in two regions. The region near the absorption edge is called the XANES (X-ray Absorption Near-Edge Spectroscopy) region. The absorption at energies above the edge is named EXAFS (Extended X-ray Absorption Fine Structure). The XANES part of the spectra is where the absorption occurs and contains information on the absorber valence and density of states and also qualitative structural information. The EXAFS part is the interference pattern created by the crystal environment where the photon or the photoelectron is created over different crystal sites. This can then furnish detailed information about the local atomic structure and quantitative structural information. Figure 3.4 presents a panel in which a XAS spectrum is presented and explained.

A XAS spectrum, μ, is presented in Figure 3.4(a). In the figure two others functions μ_0 and μ_α are defined. These are the extrapolated backgrounds of the spectra, below and above the edge. From these three functions, it is possible to extract the EXAFS spectrum

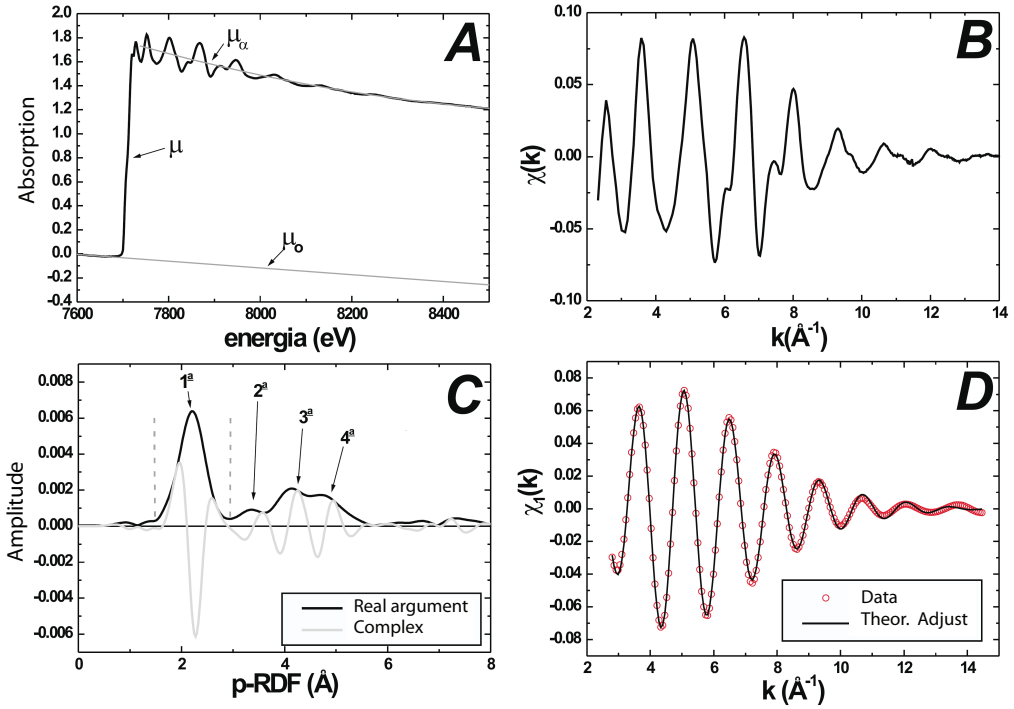

Figure 3.4: Panel presenting a XAS measurement. In (a) is presented a complete XAS spectrum and in (b) only the EXAFS part. In (c) is presented the Fourier transform of the EXAFS part with real and imaginary arguments. In (d) an inverse Fourier transform of the real argument of the result shown in (c) is compared with a simulated result (Reprinted from (CEZAR; VICENTIN; TOLENTINO, 2000).

$\chi(k)$, presented in 3.4(b), with the following relation:

$$\chi(k) = \frac{\mu - \mu_\alpha}{\mu_\alpha - \mu_0} \tag{3.1}$$

It is important to note that the XAS spectrum dependence is in energy while the EXAFS is in wave vector. This change of variables is trivial by the use of the relation:

$$k = \sqrt{\frac{2m(E - E_0)}{\hbar^2}} \tag{3.2}$$

where m is the electron mass, E_0 is the binding energy of the excited electron (edge energy), E is the photon energy and $\hbar$ is the reduced Planck.

Then, performing a Fourier transform of the EXAFS signal, one obtains a radial distribution characteristic of the neighborhood of the absorber atom. If the sample has a crystalline order, the n order neighbors are always at a given distance, as presented in 3.4(c) where the order of the neighbors is given and the signal is separated in real and imaginary parts. Performing an inverse transform of the real signal, a distribution is obtained that can be fitted with some atomic parameters of the material studied (CEZAR;

VICENTIN; TOLENTINO, 2000). Such a simulation is presented in 3.4(d).

3.4 Magnetic measurements

In order to measure the magnetization of a sample, it is possible to use techniques based on force, on torque, on induction or optical effects. One of the most common method used is by the induction of an electric potential in a set of coils by the movement of the sample next them. The induced electric potential is proportional to the total magnetic moment of the sample; hence it is necessary to normalize this value by the volume or the mass of the sample to obtain the magnetization.

Mainly two techniques of induction are possible: the extraction (the sample is moved once over the extension of the coil set) and vibration (the sample vibrate at a defined frequency with a small amplitude around a given position in relation to the coil set) (CULLITY; GRAHAM, 2009). The electric potential generated on the coil set is given by the Faraday's induction law and is proportional to the flux variation and to the number of coils.

The coil set presents generally a specific geometry engineered to carry out the magnetic measurements and this ensemble is called a gradiometer. For magnetic moment measurements, a second-order gradiometer, as presented in Figure 3.5(a), is generally used (AUBERLECHNER; KASPERKOVITZ; STEINER, 1998). As the sample is moved through the gradiometer, the induced voltage is measured. The variation of the voltage as a function of the sample position is presented in Figure 3.5(b), for a positive magnetization.

The magnetic measurements reported in the thesis were performed using a Quantum Design SQUID magnetometer. The measurements were carried out in the extraction mode. The equipment is called SQUID because the magnetic flux probed by the coils set is measured by a Superconducting Quantum Interference Device. A SQUID sensor consists in a superconducting loop containing Josephson junctions that enable the measurement of magnetic moments with a very high sensitivity (CULLITY; GRAHAM, 2009). As the SQUID sensor operates at low temperature, a second order gradiometer collects the flux generated by the sample and transfer it to the SQUID sensor immersed in liquid helium. The conversion of the induced voltages to magnetic moment values is made automatically by the equipment software, through a fit of voltage-position curves such as the one depicted in Figure 3.5(b). Details about the fitting procedure can be found in (STAMENOV; COEY,

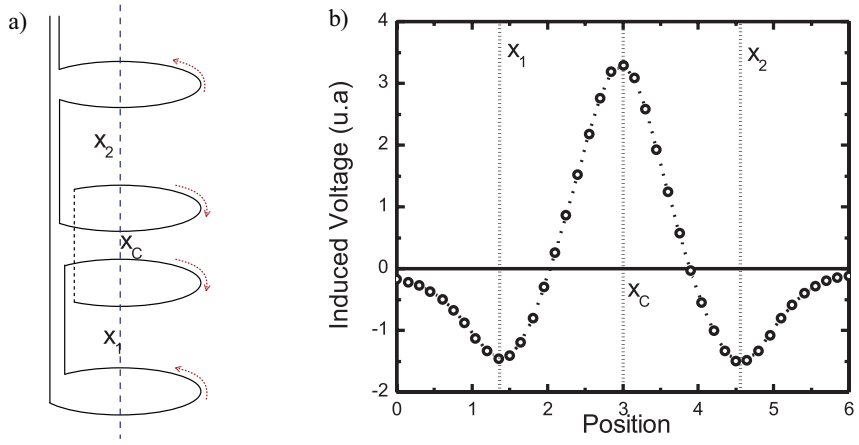

Figure 3.5: A second order gradiometer composed of four centered coils with the relative sense of current as indicated by the red arrows in (a). In (b), the induced voltage as a function of the sample's position.

2006).

For measurements as a function of the magnetic field, three scans of the position were performed and averaged at each field step. For measurements as a function of the temperature and viscosity measurements, only single scans were done in order to avoid the influence of thermal effects on the results.

Magnetization measurements as a function of the temperature were carried out following Zero-Field Cooling (ZFC) and Field-Cooling (FC) procedures. The ZFC procedure consists in warming the sample to a temperature higher than the transition to the disordered phase in the absence of applied magnetic field. After that, the sample is cooled down to the lowest temperature still in the absence of magnetic field. At a given temperature, a low field is applied and the magnetization behavior is measured while the temperature is raised at a rate of 2 K/min. The FC procedure is similar, but the cooling process is performed with an applied magnetic field.

3.5 Ferromagnetic resonance

Ferromagnetic resonance (FMR) is a very sensitive technique to probe the magnetic properties of materials and, more precisely, to investigate the magnetic anisotropy of a system. The usual configuration of a FMR measurement system is composed of a magnetic DC field generator, a microwave generator, a microwave detector, and a resonant cavity. The resonance of the cavity lies in the frequency range of the microwaves delivered by the generator and the absorption of the microwave in the cavity can be monitored by the detector.

Figure 3.6 shows a scheme of a typical FMR setup.

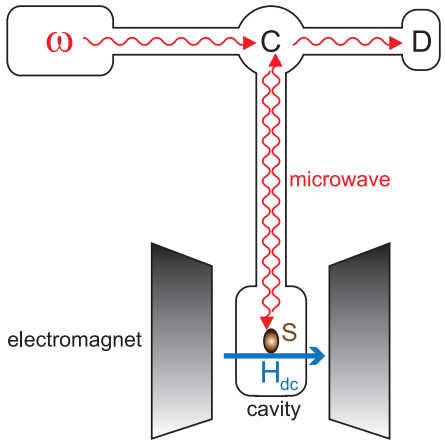

Figure 3.6: Scheme of a typical FMR setup. ω: microwave generator, C: circulator allowing to direct the input microwave towards the cavity and the output microwave towards the detector. D: detector. S: sample.

The FMR technique is mostly used to measure the values of the magnetic anisotropies constants in magnetic systems. To do this, the resonance field of the sample is measured as a function of the angle of the applied magnetic field. For thin films, two geometries can be investigated: θ-scan and ϕ-scan as shown in figure 3.7. In ϕ-scan geometry we probe the resonances in the plane of the sample and in the θ-scan geometry we probe the resonance in a plane perpendicular to the surface of the film. The θ-scan geometry can be performed for different initial ϕ angles.

The measurement consists in monitoring the microwave absorption of the sample as a function of the applied static (DC) magnetic field. When a magnetic field is applied in a given direction, the magnetization of a domain present in the sample will precess around this direction at a given frequency (called Larmor frequency) that depends on

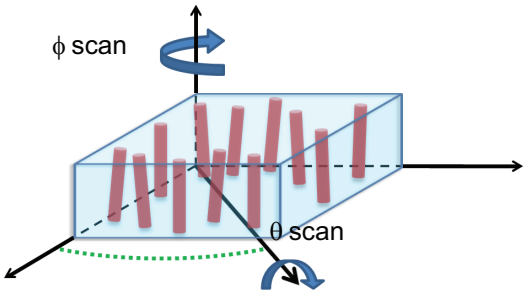

Figure 3.7: Axis of rotation in the two possible geometries: for ϕ-scan the axis is perpendicular to the film surface and for θ-scan it lies in the plane of the sample. For θ-scan, it is possible to perform measurements for various values of ϕ.

the intensity of the applied magnetic field and on the magnetic free energy of the system. The microwave insert in the cavity has a RF magnetic field component that points perpendicular to the DC applied magnetic field, thereby inducing a precession. When the frequency of the microwave and the Larmor frequency are equal, the condition for the ferromagnetic resonance is fulfilled. In the experiments, this resonance conditions are met by tuning the intensity of the magnetic field while maintaining the microwave frequency constant. Figure 3.8 presents the configuration of the magnetic moment, the applied field and the plane probed in ϕ and θ scans for the case of nanowires grown perpendicular to the surface of thin films. The DC and RF magnetic field are always in the plane probed and are perpendicular to each other. The configuration with $\theta = (\pi/2)$ at a given ϕ^* angle is practically[1]the same as the configuration for ϕ-scan geometry at the same ϕ^* angle.

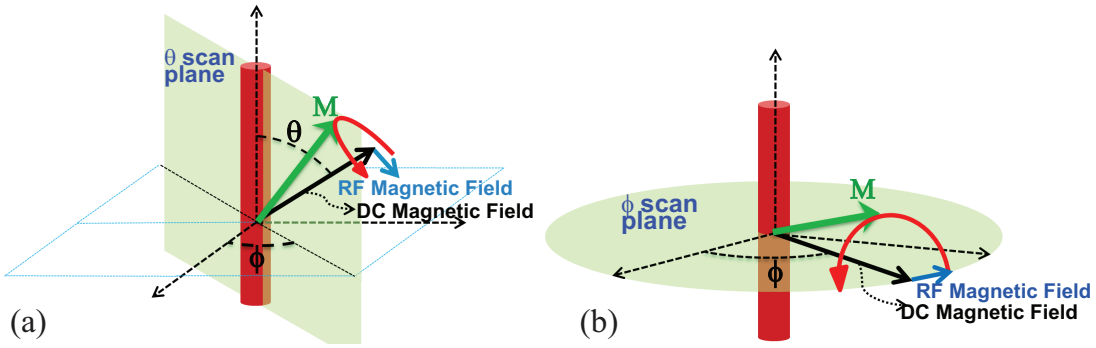

Figure 3.8: Scheme of ferromagnetic measurements for our samples exhibiting the two geometries of measurements: (a) θ-scan and (b) ϕ-scan. For θ-scan, it is possible to perform measurements with different ϕ angle.

[1]The difference lies in the direction of the applied RF field. For ϕ-scan the RF field points perpendicular to nanowires and for θ-scan it is parallel to the nanowires. This does not alter the resonance field measured but can influence the amplitude of the signal.

4 Self-assembly of Co nanowires in CeO_2 thin films growth on $SrTiO_3(001)$

This chapter reports the experimental results obtained on structural and magnetic properties of Co doped CeO_2 thin films produced via the pulsed laser deposition technique.

4.1 Growth conditions

Co doped CeO_2 thin films were produced by PLD at Institut des NanoSciences de Paris. The experimental setup of this PLD growth system is composed of an excimer KrF laser and a growth chamber. The laser has a wavelength of 248 nm, pulse duration of 20 ns, a fluency of 3 J/cm^2 and a frequency of 2 Hz. An optical setup permits to focus the laser on targets inside the growth chamber. The growth chamber can be kept under specific pressure conditions varying from 10^{-7} mbar of residual pressure to some mbar. It is also possible to control an oxygen pressure in the range of some mbar to 10^{-3} mbar due to a laminar flux of gas in chamber.

Inside the growth chamber there is a substrate holder with a heater controlling the substrate temperature during the growth from ambient up to 800°C. Also inside the growth chamber is kept a rotating target holder with capacity for up to 5 different targets and allows shooting sequentially on the targets during the growth procedure. Two substrates were used for the deposition of thin films: undoped $SrTiO_3(001)$ and n-doped Si(001). Before the growth procedure, a thermal annealing of the substrate is performed in the growth chamber in order to clean the $SrTiO_3(001)$ surface. The treatment consists in keeping the temperature at 670°C during one hour under an oxygen pressure of $5x10^{-2}$ mbar. This treatment allows us to clean the surface of the substrate and guarantees subsequent epitaxial growth of CeO_2 thin films on $SrTiO_3(001)$, as was shown in previous work (ZHENG et al., 2008; VODUNGBO, 2008).

The growth is performed on both subtrates ($SrTiO_3$(001) and Si) at the same time an annealing is then carried out for both, but it has no effects on Si subtrate oxidized surface.

After the thermal annealing, the substrate is cooled down to the growth temperature (∼650°C). The first step is to grow a buffer of pure cerium oxide under pressure of 5x10^{-2} mbar. This buffer layer has ∼4 nm of thickness and allows to start the growth of CeO_2 with the desired epitaxial relationship with respect to $SrTiO_3$(001). This step is therefore important for the crystalline quality of the thin films.

After the buffer layer growth, the procedure consists in shooting alternately on targets of cerium oxide and cobalt oxide (CeO_2 and CoO). The ratio between the shots on two targets gives the nominal concentration of dopant. For a given concentration a sequence of tenths of shots in each target is calculated and after is repeated in order to attain ∼20000 shots. A set of samples were grown with the sequence of shots indicated in Table 4.1. The extrapolated concentration shown in the table was determined as ∼85% of nominal concentration using Rutherford backscattering calibration.

Table 4.1: Recipe of a series of samples grown. The columns Co $\%^{nom}$ and Co $\%^{ext}$ refer respectively to nominal and extrapolated Co concentrations in samples.

Co ($\%^{nom}$)	Shots		Repetitions	Co ($\%^{ext}$)
	CeO_2	CoO		
5	57	3	333	4
10	18	2	1000	8
15	17	3	1000	12
20	12	3	1000	17

4.2 Structure of thin films

4.2.1 Crystalline structure of thin films

The crystalline structure of the thin films was investigated by x-ray diffraction and transmission electron microscopy. A PHILIPS diffractometer X'Pert MRD with four circles was used in the investigation using a Cu K-α_1 X-Ray source with wavelength of 0.154056 nm.

The Figure 4.1 presents typical patterns for samples grown on $SrTiO_3$(001)

substrates. Figure 4.1(a) shows different ϕ-scans and contains information on the crystalline arrangement of thin films in the plane of the substrate. Figure 4.1(b) presents a typical θ-2θ scan that contains information on the orientation of the film (lattice spacing in the out of plane direction).

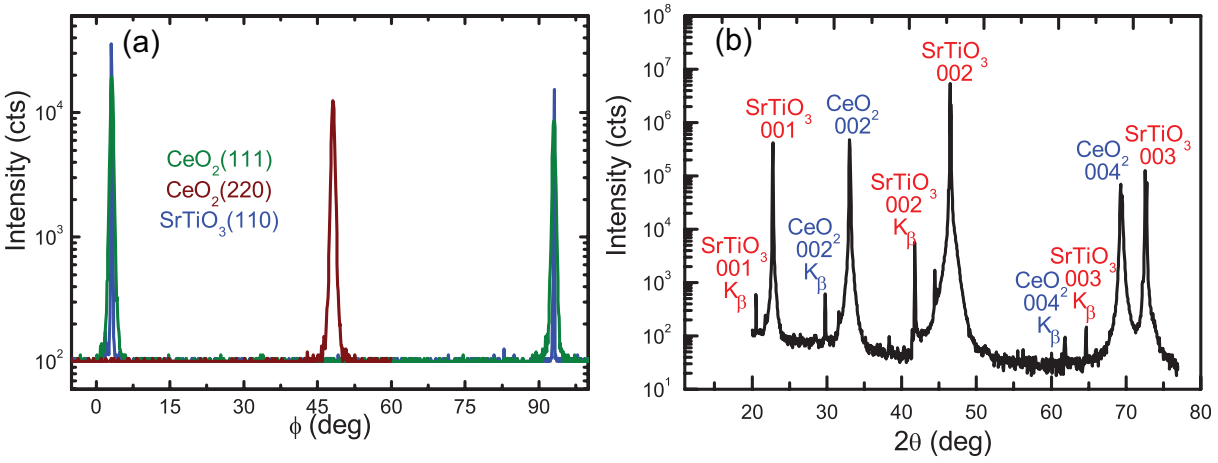

Figure 4.1: X-ray diffraction pattern for a 5 % Co doped $CeO_2/SrTiO_3(001)$ thin film in (a) ϕ-scan and (b) θ-2θ scan geometries.

The diffraction patterns show that the Co-doped CeO_2 films have a good epitaxy with orientation relationship $CeO_2(001) \parallel SrTiO_3(001)$ and $CeO_2(110) \parallel SrTiO_3(010)$. This indicates that the crystalline unit cells of CeO_2 and $SrTiO_3$ are rotated by 45 degrees.

Figure 4.2 presents a scheme of this epitaxy. It occurs because the lattice parameter of CeO_2 (a_{CeO_2}=0.5411 nm) is very close to the distance between planes (110) of $SrTiO_3$ ($d_{(110)}$=0.5523 nm). Thus, this epitaxy strongly reduces the lattice mismatch to about 2 %. In this scheme, it is possible to see that, due to the unit cells rotation, the oxygen sub-lattice is continuous at the film/substrate interface.

The results presented in Figure 4.1 were obtained for a sample with 5 % nominal Co content and the patterns are roughly the same for other concentrations. Increasing Co contents leads to an increase of the structural disorder as could be attested by a decrease of the intensity and a broadening of CeO_2 004 reflections (not shown here) (ZHENG et al., 2008). The presence of Co could, however, not be detected by means of X-ray diffraction.

Samples grown on Si substrates are oriented in the (100) direction but are textured in the plane of the thin film. The texture is dependent on the growth conditions, especially on the oxygen pressure. Due to better quality of thin films grown on $SrTiO_3$, the following investigations were made only on samples grown on this substrate.

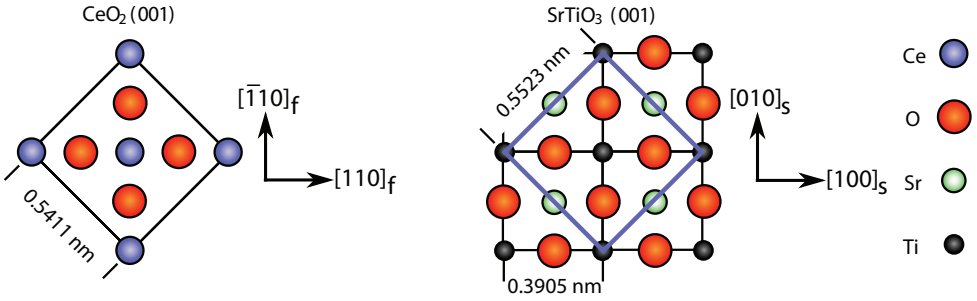

Figure 4.2: Scheme of the orientation relationship of CeO_2 and $SrTiO_3$ unit cells. The CeO_2 unit cell in the (001) plane is shown in the left part and the $SrTiO_3$ unit cell in the (001) plane is shown in the right part. The subscript f and s stand for film and substrate, respectively.

4.2.2 Internal structure of thin films

The internal structure of thin films was investigated by means of transmission electron microscopy techniques (TEM). Figure 4.3 presents a typical TEM image for samples with low Co content in cross section.

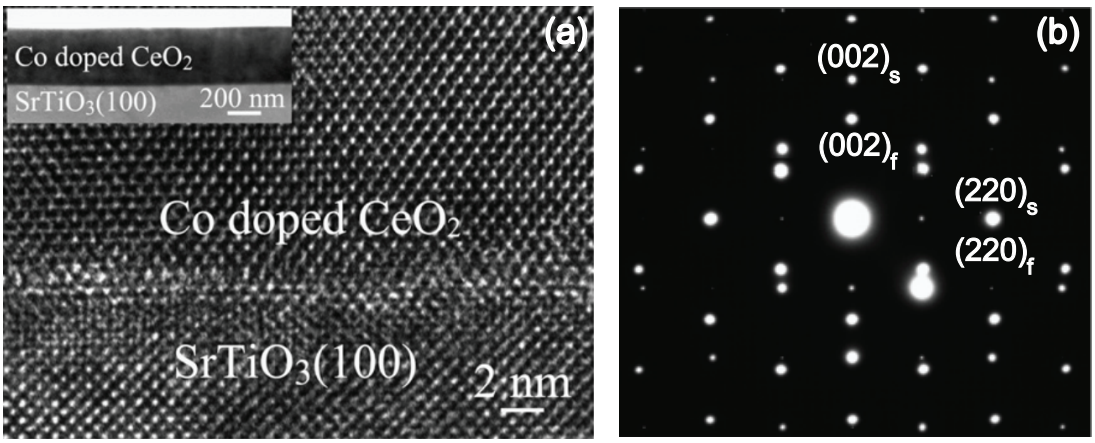

Figure 4.3: (a) High resolution transmission electron microscopy of a thin film grown with 5% Co content in cross section showing the sharpness of the interface. Inset: low resolution image showing the whole film thickness. (b) Electron diffraction attesting the high crystalline quality of the samples.

Figure 4.3(a) shows a HRTEM image of the $CeO_2/SrTiO_3(001)$ interface. The image attests the sharpness of the interface between the substrate and the film for samples with absence of dislocations perpendicular to the plane of the substrate. The inset shows a low resolution image of the film that can be used to measure the growth film thickness.

Information about the crystalline structure obtained by x-ray diffraction was confirmed by electron diffraction performed in the TEM microscope. The diffraction pattern is shown in figure 4.3(b) with the indexation of the electron diffraction spots

confirming the epitaxial relationship.

For low Co content no signal associated to Co was found in TEM images. However, for images (TEM) obtained on samples with a higher concentration, some elongated-shape regions with a crystalline structure different from that of CeO_2 appear as shown in Figure 4.4.

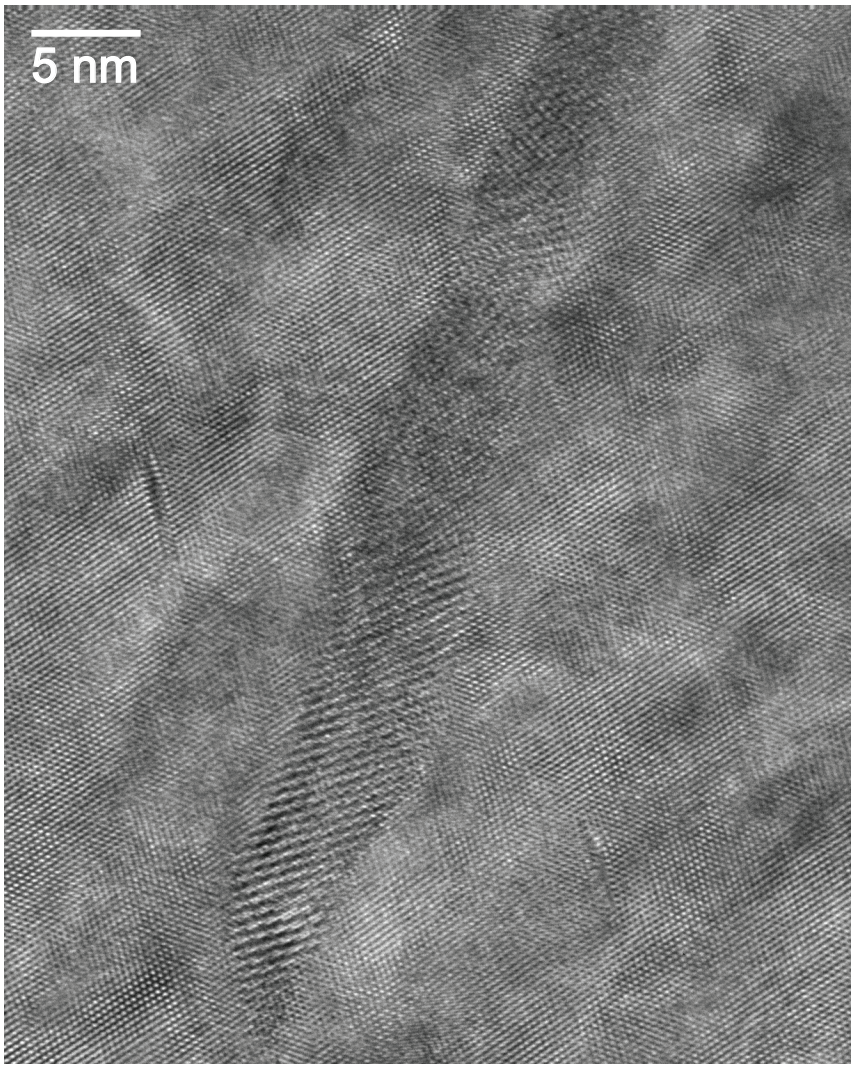

Figure 4.4: HRTEM image in cross section geometry for a thin film with 10 % of nominal content.

These elongated-shape regions have a width of ∼5 nm and lengths of the size of the images. They are oriented parallel to the growth direction with a narrow distribution in angle. The crystalline structure of these regions could not be indexed for any known composite with the elements presents in sample. The inter-planar distance estimated for these regions would be larger than any other existent composite. In fact, the complex structure present in such regions is due to the phenomenon of multiple diffraction that will be discussed further in section 6.1.

4.2.3 Cobalt valence state

Electron energy loss spectroscopy (EELS) was performed during TEM experiments in order to obtain information about the Co valence in thin films. Figure 4.5 presents the results obtained for a thin film with 15 % of cobalt nominal content (symbols) and for a reference Co sample (line).

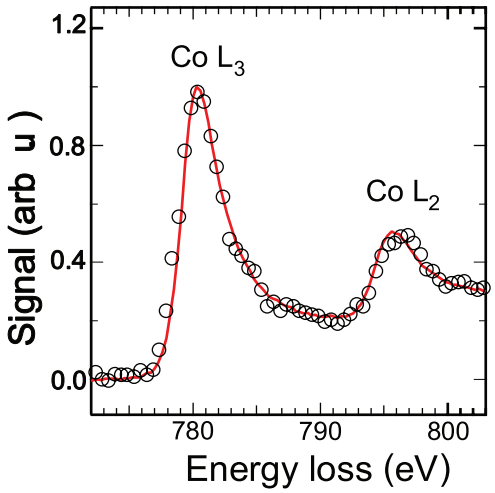

Figure 4.5: EELS spectra for a thin film with 15 % of cobalt nominal content (symbols) and for a reference Co sample (line) .

The EELS signal at Co L-edge indicates that Co is metallic in the thin films. However, EELS performed with the TEM has a rather low spectral resolution of the order of the eV. To confirm the EELS results, x-ray absorption spectroscopy (XAS) was performed at SAMBA beam-line in synchrotron SOLEIL (St Aubin - France). The measurements of x-ray absorption were carried out in fluorescence mode, thereby allowing bulk detection, without enhanced sensitivity to the surface. The energy range probed was that corresponding to absorption at the Co K-edge (7725 eV). The results are separated in two regions: extended x-ray absorption fine structure (EXAFS shown in Figure 4.6) and near-edge spectroscopy (XANES shown in Figure 4.7).

The Figure 4.6(a) present EXAFS spectra for CeO_2 thin films with 15% of Co content. The thin film spectrum is quite similar to the one of a Co metallic reference sample. The Fourier transform of this signal and also a simulated signal considering a Co single shell surrounding the Co absorber is displayed in figure 4.6(b). This way is shown that Oxygen is not detected on Co environment and this proves that Co is not diluted in the CeO_2 structure, i.e. the Co is in metallic state in the thin films.

Figure 4.7(a) shows XANES spectrum for CeO_2 thin film with 15 % Co content. The XANES signal of the epilayers is again quite similar to the reference one obtained with a

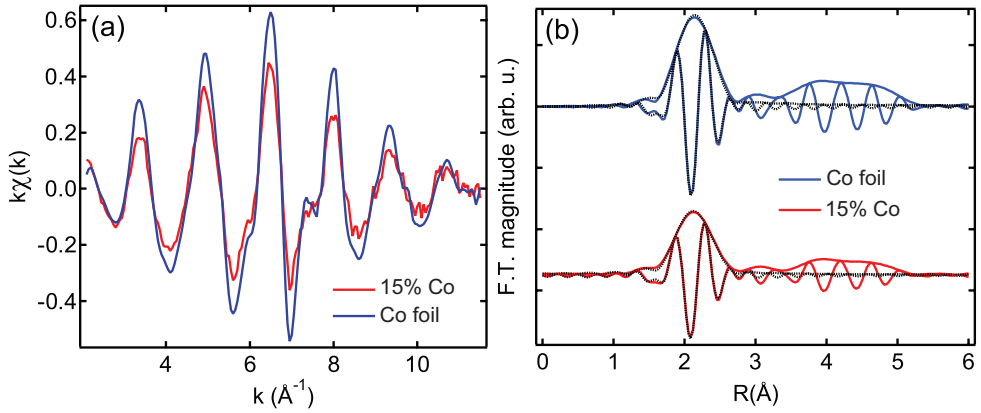

Figure 4.6: (a) EXAFS spectra for a thin film with 15 % cobalt nominal content compared with a reference sample. (b) Fourier transform of EXAFS signal (lines) and simulation considering Co bulk parameters (dotted lines).

metallic Co foil in the same figure indicating the metallic character of cobalt in the films, as characterized by the pre-edge feature in the 7710-7720 eV spectral range.

Metallic Co can be present in two crystalline structures: hexagonal close-packed (hcp) and face-centered cubic (fcc). The effect of the fcc/hcp phase transition is not much visible in the EXAFS especially if it is not possible to analyze an epitaxial growth and take advantage of x-rays polarization to undercover the anisotropy of hcp with respect to fcc. In our case, all the signals are isotropic. On the other hand, for the XANES region the difference between hcp and fcc is much more evident, even for disordered or statistically oriented systems and it is due to the difference in the arrangement of multiple scattering paths.

This difference is illustrated in Figure 4.7(b) and (c) where two *ab initio* calculated[1] XANES spectra for hcp and fcc structures are depicted. The peak marked by an arrow (in 4.7(c)) is much more pronounced in the fcc form than in the hcp in agreement with other studies (MIYAWAKI et al., 2007). Comparing such simulated spectra with the one obtained on our samples and on the reference, we deduce that Co crystallizes mainly in the hcp arrangement. Nevertheless some possible minority fcc regions cannot be totally excluded.

[1]The *ab initio* calculationhas been carried out by Dr. Emiliano Fonda, scientific of the SAMBA beamline at SOLEIL synchrotron.

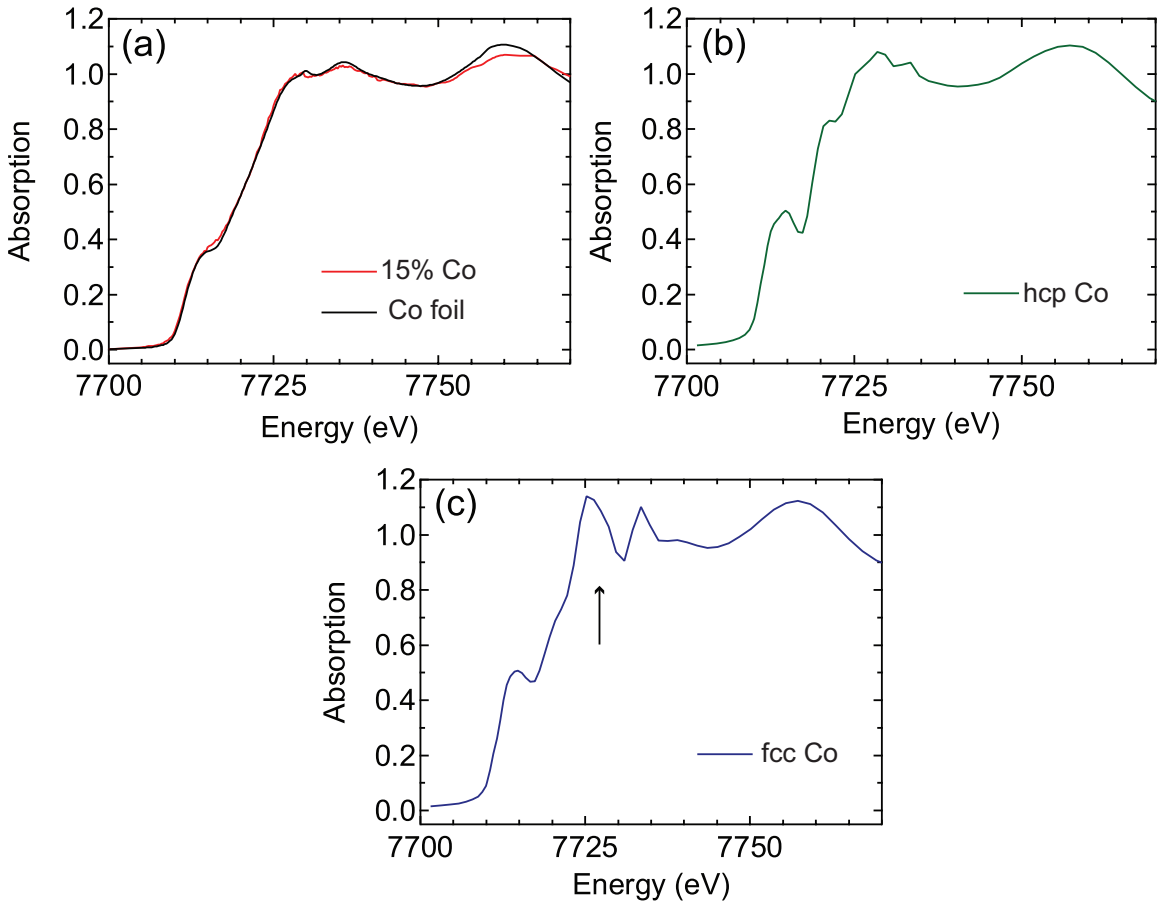

Figure 4.7: XANES spectra at Co K-edge. In (a) the spectra for thin film with 15 % cobalt nominal content and, also for a Co metallic reference sample. In (b) and (c) *ab initio* simulations for Co with crystalline structure hcp (b) and fcc (c).

4.2.4 Localization of Co in the matrix

The spectroscopic results indicate that, under the growth conditions, the cerium oxide reduces CoO in metallic Co. This means that phase segregation occurs during the growth in our Co doped CeO_2 thin films. Having attested this segregation and the valence state of Co in the epilayers, we have turned our attention to the localization of this secondary phase of metallic Co.

In order to answer this question, energy-filtered transmission electron microscopy (EFTEM) techniques were carried out on the samples. As discussed in section 3.2 this technique allows us to filter the images at element-specific energy loss of the electrons. In this way, it is possible to obtain a chemical map of our sample for a given element, depending on the selected energy. Here, the selected energies are tuned near Co L-edge ($\sim$ 780 eV) and the bright regions indicates a high Co concentration. Figure 4.8 shows EFTEM images (cross sections) for samples with different Co content.

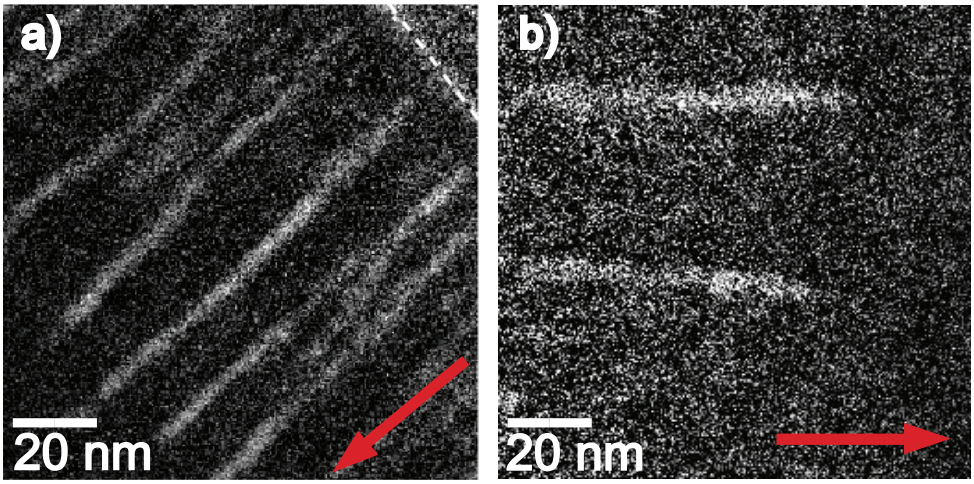

Figure 4.8: EFTEM showing cobalt-rich regions for samples with cobalt content of 20% (a) and 10% (b). The red arrows indicate the growth direction in each case and the dotted line in the right-up corner of image (a) shows the frontier between film and substrate.

The images suggest that the Co is accumulated in elongated regions with the same dimensions as the regions previously detected in HRTEM (presented on Figure 4.4). These regions have width in the range of 3 to 7 nm and lengths up to the film thickness. In order to prove the existence of Co agglomeration also for low Co content samples, EFTEM was also performed in plane view geometry as presented in Figure 4.9. The images show that Co rich regions appear as disks in plane view. From these images one can see that the diameter of these regions is roughly the same, independently of the Co content in the samples.

From these EFTEM results, combined with the XAS data, we conclude that cobalt nanowires (FNW) form spontaneously during sample growth. Nevertheless, it is important to note that for concentrations below 10%, it is hard to find regions exploitable for EFTEM images in cross section. This is mainly due to the low density of FNW in the samples. The Co content in the thin films controls the density of the objects formed during the growth (this can be seen in Figure 4.9), with the density of NW being proportional to the Co content. Then, detection of FNWs in cross section for diluted samples with Co content below 5% is highly improbable.

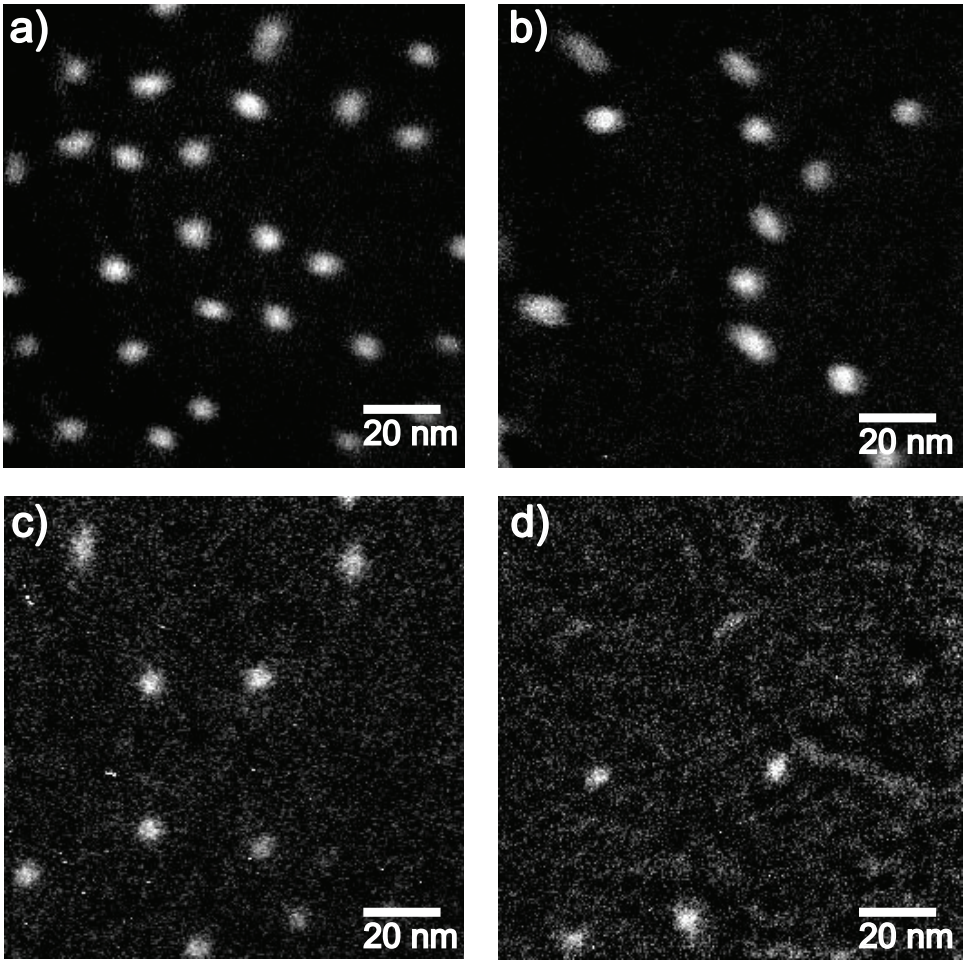

Figure 4.9: EFTEM in the plane of growth for thin films with (a) 20%, (b) 15%, (c) 10% and (d) 5% Co content growth at T=650°C.

4.3 Diluted magnetic oxide or phase segregation

The previous section presented the structural and spectroscopic results of Co-doped CeO_2 thin films produced by PLD. The results enable us to conclude the formation of a secondary phase in the form of Co nanowires. Nevertheless, the detection of FNWs in diluted samples with Co content below 5% is highly improbable, principally in cross section geometry. The difficulty to detect such kind of objects can induce some premature conclusions about the origin of the magnetic properties in some materials claimed to be diluted magnetic semiconductors or diluted magnetic oxides systems.

After the theoretical prediction of the coexistence of ferromagnetic and semiconducting properties for some p-doped semiconductors (DIETL et al., 2000) a lot of scientific efforts have been directed to this subject. The challenge consists in inducing long-range ferromagnetic order in a nominally non-magnetic system by replacing a minor fraction of its cation by 3d magnetic species. This has been successfully performed in

the case of $Ga_{(1-x)}Mn_xAs$, with a Curie temperature below room-temperature.

Concerning oxides, many reports appeared during the last decade claiming ferromagnetism above room-temperature (RT-FM) in diluted magnetic oxides. However, there are still contradictory reports evidencing clustering of the magnetic elements inside the oxide matrix (COEY; CHAMBERS, 2008). If ferromagnetic clusters formation takes place, the magnetic signal comes from the presence of such secondary phase.

The first argument commonly used in literature to rule out clustering in the materials exhibiting ferromagnetism at room temperature relies on the evaluation of the blocking temperature (T_b) of a superparamagnetic clusters assembly. Let us consider spherical clusters and the magneto-crystalline anisotropy (K_{cry}) as the main source of magnetic anisotropy. Then, using $K_{cry}V = 25k_BT_b$[2], $T_b \simeq 500$ K results in cluster diameters above 8 nm for cobalt. This diameter is *large* enough to be easily detected in HRTEM images. Then, a sample presenting no blocking temperature up to $T = 400K$ (temperature limit for typical magnetic measurements) and with no traces of clusters in HRTEM images may be interpreted as a diluted magnetic system.

This criterion is not reliable because the two main assumptions (spherical shape and K_{cry} dominating the magnetic anisotropy) that support it are not necessarily fulfilled. An example is the case where the shape of the objects constituting the secondary phase has a high aspect ratio as is the case for nanowires. Therefore, the $K_{cry}V$ criterion should be used quite cautiously in order to rule out the presence of superparamagnetic clusters in the matrix from magnetic measurements.

Our Co-doped CeO_2 produced by PLD do not present blocking temperature below 400 K. Figure 4.10 presents the typical behavior of the magnetic moment for a sample containing 15% Co as a function of the temperature following ZFC (Zero Field Cooling - hallow symbols) and FC (Field Cooling - Solid Symbols) procedures.

In Figure 4.10(a) the behavior is presented for different applied magnetic fields and even for low applied fields no blocking temperature is observed. In Figure 4.10(b) the curve for an applied field of 0.8 T is presented in detail with a fit assuming the expected Bloch ferromagnetic behavior in which the magnetization decays with a $T^{\frac{3}{2}}$ law (DYSON, 1956). The fit performed considers only the experimental data above 100 K (FC curve). In the case of a superparamagnetic system, the high temperature asymptotic behavior would be a T^{-1} decrease of the magnetization (following the Langevin equation). Therefore, the good agreement of the $T^{\frac{3}{2}}$ law is a clear ferromagnetic signature.

[2]With V the volume of the cluster and k_B the Boltzmann constant

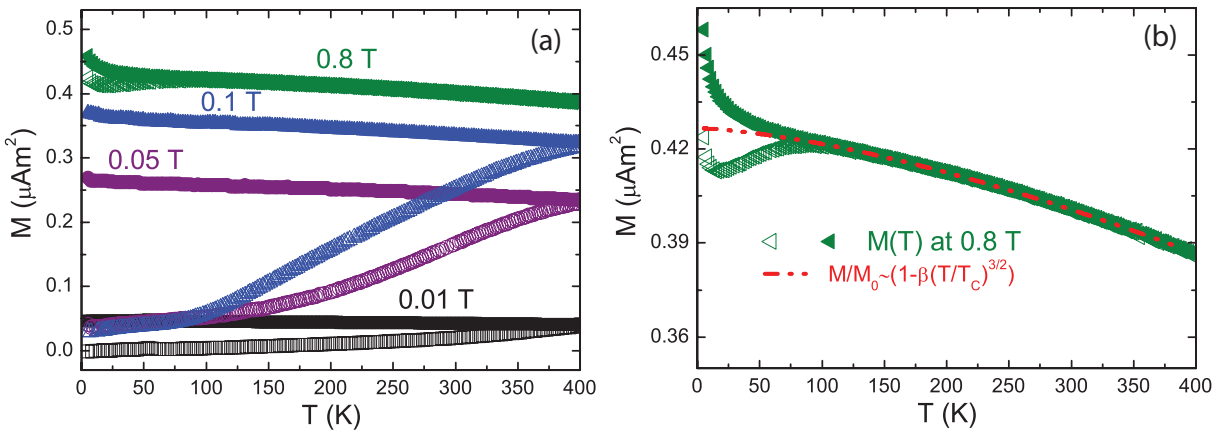

Figure 4.10: (a) Total magnetic moment in function of temperature for a 15% Co sample following the ZFC (open symbols) and FC (solid symbols) procedures at different applied fields . In (b) the detail of the M(T) curve for 0.8 T with a fit of the data to $a - bT^{\gamma}$, giving γ=1.55±0.01

.

For low temperatures ($T < 30$) a paramagnetic behavior is observed, in both ZFC and FC curves, with increasing intensity when the magnetic field increases. This signal, only observed at low temperature, has been associated to paramagnetic impurities present in the substrate.

Normalizing the magnetic moment value of the sample by a Co volume estimated from TEM images leads to the saturation magnetization of Co bulk indicating that the magnetic moment measured in our samples is mainly due to Co nanowires. Moreover, with the volume estimate, it is possible to calculate the ratio between Co and CeO_2 atoms. Similar calculation has been performed for samples with different concentrations and the evaluated content is approximately the nominal content (the difference can be explained by the error propagation on the volume estimated by TEM images). This result indicates that the vast majority of the Co atoms are present in the FNWs.

4.4 Size and angular distribution of nanowires

Taking benefit from the range of reduced diameters that can be reached with this new approach, the magnetic properties of two samples will be investigated. The magnetic properties of FNW assemblies are profoundly dependent on the diameter and the relative orientation of the objects. In this section we will focus on the distribution of sizes of two samples that were grown with the same 15% of Co content but containing FNW with different diameters: sample d_5 is an assembly of 5 nm wires and sample d_3 an assembly of 3 nm wires.

Figure 4.11 shows HRTEM images of the two samples grown with 15% Co nominal content. The images show that the FNW diameter in these two samples is different. This difference in the diameter of the wires is related to the growth conditions. Indeed, it was shown that reducing the growth temperature led to a reduction of the diameter (BONILLA, 2010). With growth temperature T_{Growth}=650°C a 5 nm wires assembly is formed and reducing the growth temperature by 50°C (with the same growth sequence) leads to the formation of a 3 nm wires assembly. This is probably related to the reduced diffusion in the growth plane that leads to the nucleation of smaller metallic Co clusters with a higher density at lower temperature.

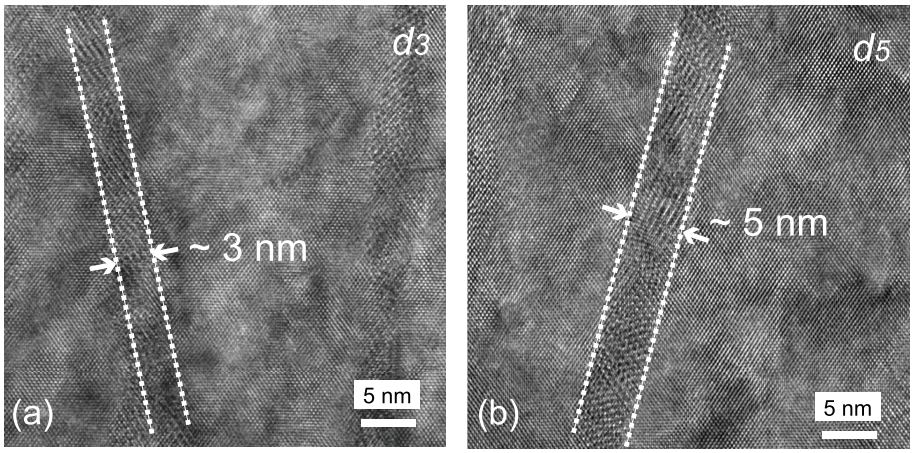

Figure 4.11: HRTEM in cross section geometry for two samples with diameter size distribution centered on 3 and 5 nm.

In order to analyze the distribution of diameter size in the samples, EFTEM images from different sample regions were recorded. The measured diameters are presented in Figure 4.12. The results are not shown as a distribution because the resolution in EFTEM mode is of the same order as the width of the distribution (± 0.5 nm). The results clearly show that the diameter of the wires is centered on 3 nm (5 nm) in d_3 (d_5) with a small width of the distribution.

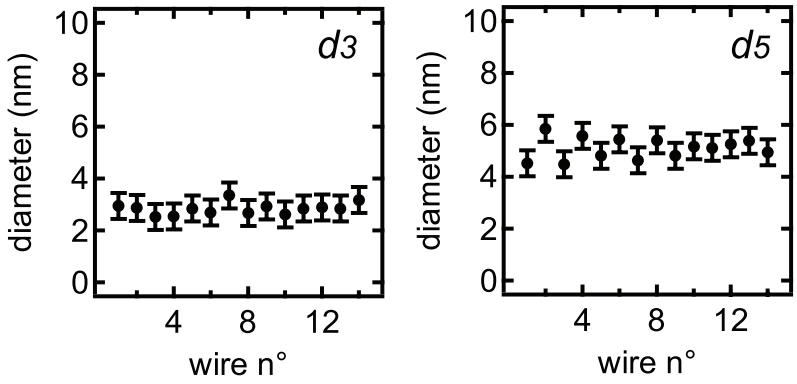

Figure 4.12: Measured diameter in different sample regions showing a very narrow distribution for samples d_3 and d_5.

From the TEM images, one can also see that the FNWs are not perfectly aligned along the growth direction. We have measured this misalignment and its distribution for the two samples, defining θ as the angle between the axis of a nanowire and the growth direction. The results are presented in Figure 4.13.

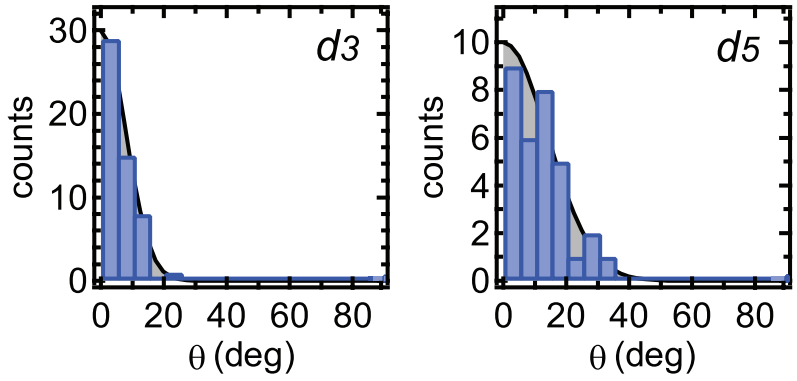

Figure 4.13: Misalignment distribution for the two NW assemblies d_3 and d_5.

4.5 Preliminary conclusions

The results of spectroscopy and microscopy combined together allow us to conclude that Co metallic nanowires (FNW) form in the Co-doped CeO_2 thin films. These self-assembled FNW are monodisperse in diameter with a very narrow distribution centered in the 3-7 nm range, depending on the growth conditions (especially on the growth temperature). They are mostly aligned in a direction perpendicular to the surface of the substrate with a narrow angular distribution.

Such objects can be hard to detect at low densities and we have discussed this point in the framework of the research on Diluted Magnetic Oxides. The difficulty in the detection of secondary phases formation can lead to some premature conclusions about the origin of magnetic response in some proclaimed Diluted Magnetic Oxides. For our Co-doped CeO_2 samples, the formation of ferromagnetic nanowires is responsible for the ferromagnetic behavior of the system. This result illustrates the role of shape anisotropy of magnetic inclusions in Diluted Magnetic Oxides. Besides, it also stresses the importance to monitor out of plane magnetic response of DMO and suggests that some previously reported results on DMO systems might be reexamined.

The formation of nanowires with diameter in the 3-7 nm range is of great interest considering the reduced diameter of the objects, lying in a range unattainable by conventional methods of nanowires preparation. In the next chapter, two samples with diameter distribution centered on 3 and 5 nm will be used as a testing ground to study the impact of size reduction and crystallinity on the magnetization reversal.

5 Study of the magnetization reversal of Co nanowires

The magnetic properties of two samples, labeled d_3 and d_5, were investigated using a SQUID magnetometer. Static and viscosity measurements were performed and the observed properties were analyzed in connection with the structural properties of the wires. These results are discussed in what follows.

5.1 Hysteresis and coercivity

The structural and spectroscopy results of the samples reported in the previous chapter allow us to make the following conclusions:

- The FNWs are made of metallic Co.
- They have a polycrystalline structure with a vast majority of hcp grains and possible trace of fcc ones.
- The samples d_3 and d_5 have narrow distributions of FMW diameter, centered on 3 nm and 5 nm, respectively.
- The FNWs axis are oriented in average along the growth axis with a misalignment distribution (this distribution is more narrow for d_3 than for d_5).

Having determined the presence of FNWs in our samples, we have turned our attention to the specific magnetic properties of such a system, concentrating our studies on the d_3 and d_5 samples.

In what follows, IP orientation corresponds to a field applied in the film plane (i.e. perpendicular to the wire axis) and the OP orientation corresponds to a field applied

perpendicular to film surface (i.e. along the axis of the wires) as can be seen in the scheme shown in Figure 5.1.

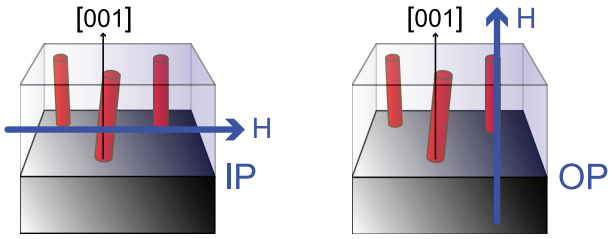

Figure 5.1: Schema for field applied direction of the IP and OP configuration.

The theoretical prediction of the magnetic behavior of a magnetic NW following a coherent reversal (Stoner Wohlfarth model) is a square loop for applied field parallel to the NW axis with the coercive field H_c equal to the anisotropy field H_a. For a field applied perpendicular to the axis of the wire, the loop should be closed and linear between $-H_a$ and H_a. This prediction fails for real samples for several reasons: distribution of diameter in FNWs; the misalignment of the objects; and also due to structural defects as granularity inside FNW and inhomogeneities (SKOMSKI et al., 2000). Indeed, for both d_3 and d_5 samples, this had also been observed. Figure 5.2 present the hysteresis loops for the samples at low temperature and for applied field direction in the two referenced directions.

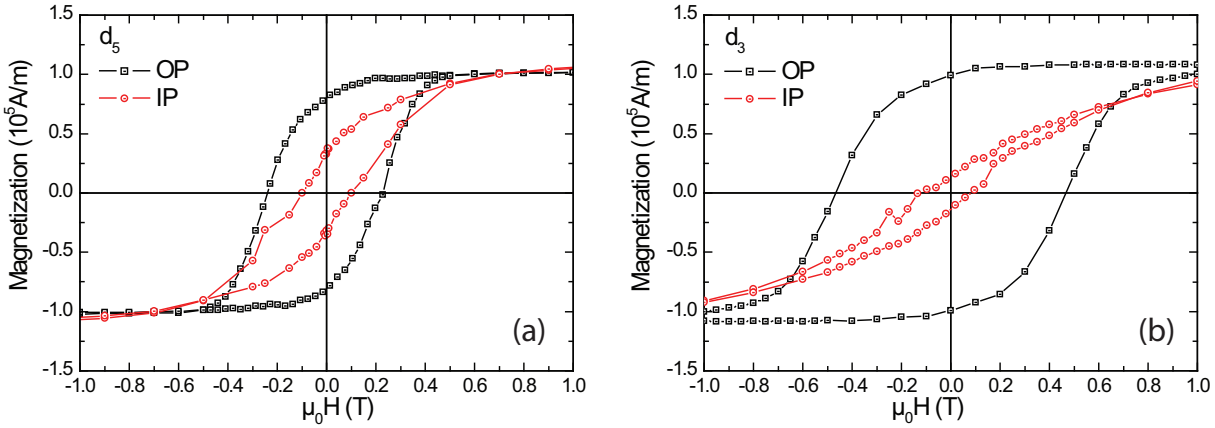

Figure 5.2: Hysteresis loop for d_5 (b) and d_3 (c) samples at 20 K for field applied in plane (IP) and out of plane (OP) of thin films.

In Figures 5.2(a) and (b) it can be seen that both samples have a highly anisotropic behavior with an easy axis perpendicular to the film plane (and a hard plane in the IP orientation). For OP measurements (field parallel to the wires axis) the cycle has a trapezoidal shape presenting a high coercive field and high remnant magnetization. For in plane measurements, the cycle is much less squared and present smaller remnant

magnetization and coercive field. Defining squareness as the ratio between remnant and saturation magnetizations (M_r/M_s), a summary of the magnetic data at 20 K is presented in Table 5.1.

Table 5.1: Summary of magnetic measurements at 20 K where the squareness is defined as M_r/M_s and H_c is the coercive field.

Sample	Squareness		$\mu_0 H_c$ (20K)	
	OP	IP	OP	IP
d_5	0.8	0.31	0.25	0.1
d_3	0.92	0.13	0.5	0.1

The magnetic behavior is highly anisotropic as is expected for assemblies of FNW with higher coercive field for applied field parallel to their axis. The squareness of cycles is related to the misalignment θ distribution in the two samples. For d_5 the misalignment is higher than in d_3 and this causes a lower (higher) squareness for field applied in OP (IP) direction. This can be rationalized considering the fact that any misorientation of the wires with respect to the OP direction (applied field direction) will lead to a lowering of the switching field with respect to the anisotropy field. Hence, a wider θ distribution leads to a more pronounced shearing of the magnetization curve and a lower squareness. The anisotropic behavior of the d_3 and d_5 wires assemblies is coherent with the contribution to the magnetic energy that arises from the FNWs' shape. These objects have a very large c/a (length/diameter) aspect ratio that induces a strong shape anisotropy. This anisotropy favors the alignment of magnetic moments along the FNWs longer axis. Most of FNWs in our thin films have lengths of the order of the film thickness (as was observed on TEM images). Then the aspect ratio of these objects is above 10. For such objects the condition of single domain is supposed to be fulfilled. In this case the superparamagnetism is not observed at ambient temperature. In fact it is possible to evaluate the blocking temperature, T_b, using $KV = 25 k_B T_b$, where K is the dominant shape anisotropy depending on the c/a ratio through the demagnetizing factor (SUN et al., 2005). Performing the calculation one obtains a blocking temperature larger than the Curie temperature of cobalt. This means that the NWs are long enough to avoid the superparamagnetic regime, as observed.

However, the hypothesis that the FNWs can be considered as single domains should be taken with care at this point: if it is the case, at room temperature we would have k_BT$<< k_B\ T_b$ and then the coercive field should be the same that the one measured at

low temperature. We will see in the next section that this is not the case.

Thermally activated reversal

Turning back to the magnetization loops shown in Figure 5.2, the coercive field along the easy axis at low temperature is smaller than the anisotropy field related to shape anisotropy in Co ($\mu_0 H_a = 2\pi M_s \sim 0.89$ T). This indicates that the magnetization reversal does not proceed through a pure coherent rotation of the entire wire. Localization of magnetization reversal is probably due to the internal structure of the FNW. In this localized regions, the aspect ratio is smaller reducing the shape anisotropy and then reducing the anisotropic field. In other words, the reversal would not occur in the entire wire, but in localized regions the magnetization flips at lower fields than in other regions. In what follow, we will present and analyze hysteresis loops at different temperatures and such measurements allow us to extract a mean energy barrier for reversal in the FNW assemblies. Knowledge of such parameter and its temperature dependence could enable us to draft the reversal process phenomena in d_3 and d_5 samples.

Figure 5.3 shows the magnetization as a function of the applied magnetic field for d_5 and d_3 samples, at different temperatures and with field applied perpendicular (OP) and parallel (IP) to the film surface.

For both samples a highly anisotropic behavior is observed, with the easy axis in the OP direction at all measured temperatures. For IP magnetization loops, a high saturation field, a low coercive field is observed and they are less dependent on the temperature. The out of plane magnetization loops have trapezoid shape with high remnant magnetization and large coercive field principally at low temperature.

The origin of the trapezoid shape in the magnetization curve can be rationalized taking into account that in the sample there exist a distribution of grain sizes and imperfections. The existence of such a distribution leads to a distribution of local energy barriers, leading to a distribution of switching fields. A quantitative way to have access to the distribution of switching fields is to take the derivative of the hysteresis cycles with respect to the applied field, along the easy axis.

Figure 5.4 show the curves obtained in such method. They present a bell shape and are very similar for d_5 and present two distinct behaviors for d_3. The curves were fitted with a Gaussian function and the parameters of the fit are presented in Table 5.2. The Gaussian distributions are centered at a value approximately equal to the coercive field for both

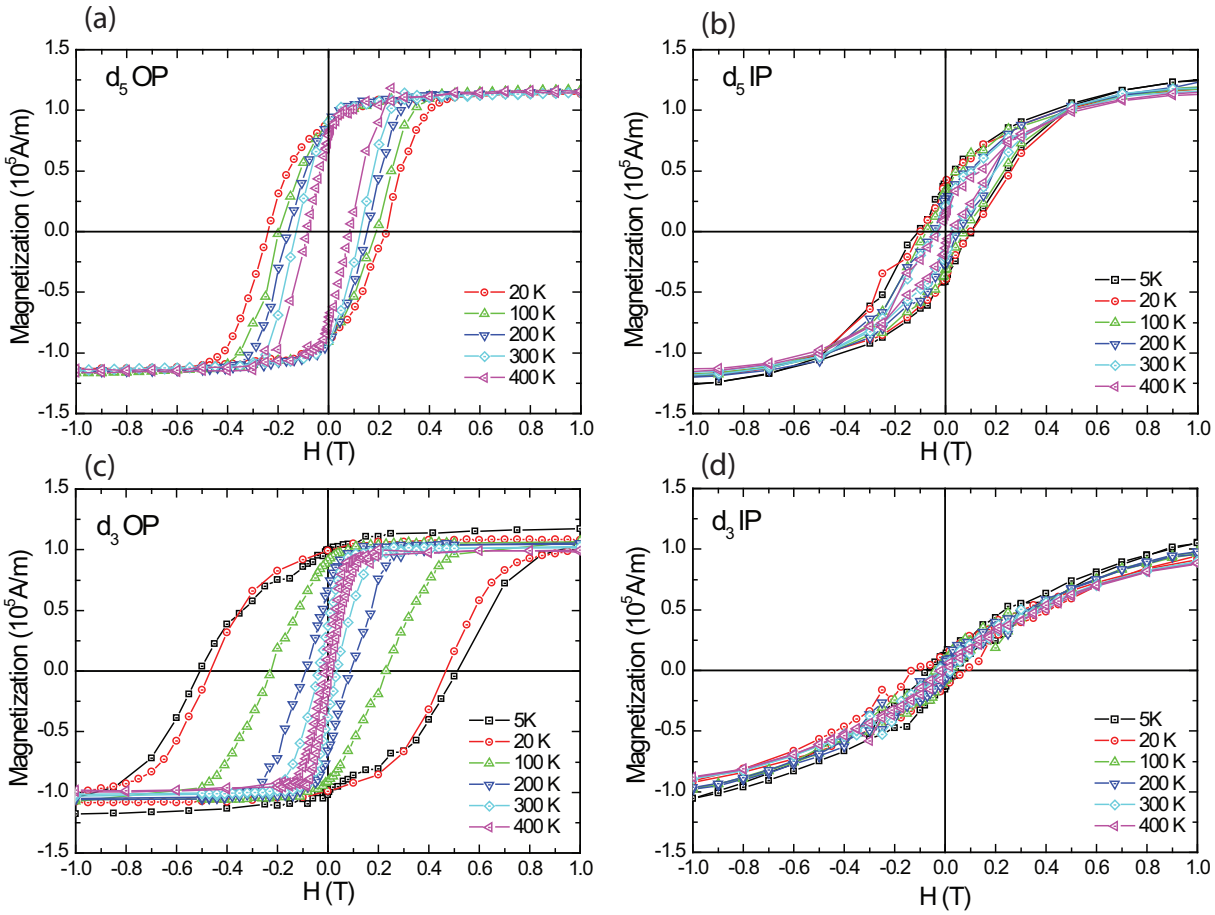

Figure 5.3: Hysteresis curves for field applied perpendicular (a) and parallel (b) to the film plane at different temperatures for d_5 sample and in (c-d) the same as (a-b) but for the d_3 FNW assembly.

samples. The width of the distribution is almost constant as a function of the temperature for d_5. For d_3 this is not the case: the width of the switching field distribution drops sharply beyond 100 K. This feature indicates that the barrier for reversal magnetization is not constant with the temperature and will be extensively discussed in next sections.

Let us try to rationalize the behavior of the magnetization. For the case of FNW the anisotropic behavior observed in magnetization curves can be mainly associated to shape anisotropy that is given by $K_S=(\mu_0/4)M_s^2$ for high aspect ratio objects. Considering the magnetization value of cobalt, the value of the shape anisotropy is $K_S=6.6\times10^5$ J.m^{-3}.

Another magnetostatic contribution that might be present is related to the dipolar interactions between wires. In the case of a regular array of FNWs, it can be shown that dipolar coupling leads to a contribution

$$K_{dip} = -3.15(\mu_0/4)M_s^2\rho^2 L/\delta \tag{5.1}$$

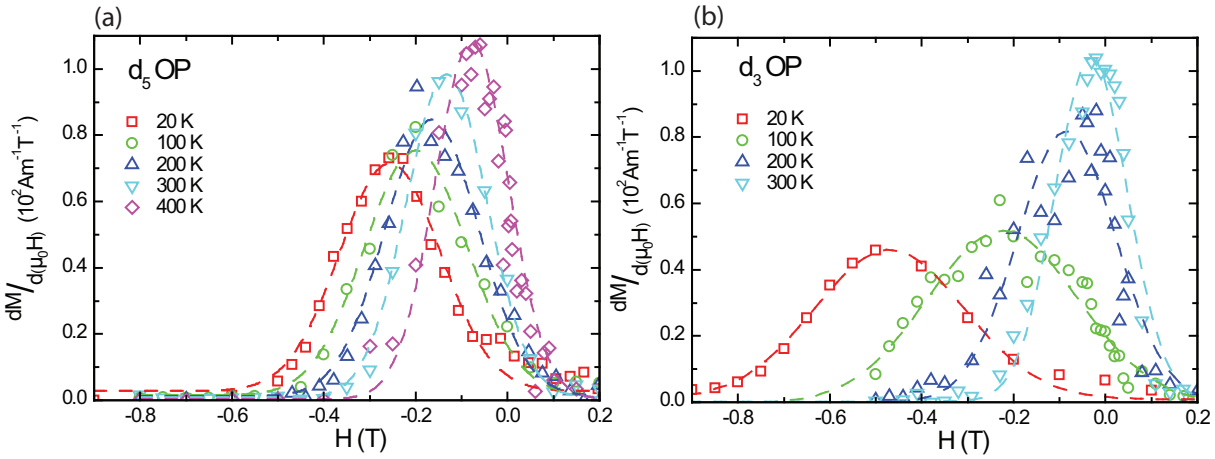

Figure 5.4: Derivative of magnetization curves ($\frac{\partial M}{\partial \mu_0 H}$) for sample d_5 in (a) and for sample d_3 in (b). The solid symbols are experimental data and dotted lines are Gaussian fits.

Table 5.2: Fitting parameters of $\frac{dM}{d(\mu_0 H)}$

Sample	T (K)	μ_0 H_{sw}(T), OP	μ_0 Δ H_{sw}(T), OP
d_5	20	0.256	0.221±0.010
	100	0.199	0.223±0.010
	200	0.165	0.203±0.005
	300	0.131	0.198±0.005
d_3	20	0.470	0.327±0.011
	100	0.224	0.329±0.016
	200	0.085	0.215±0.016
	300	0.031	0.158±0.007

where L is the length of the wires, ρ is the radius of wires, and δ the mean distance between neighboring wires (STRIJKERS et al., 1999). In our samples this simple formula probably overestimate the dipolar interactions because the d_3 and d_5 FNWs assemblies are not ordered in the plane and there is some orientation distribution. As K_S and K_{dip} have the same dependence with respect to M_s they can be merged in a single contribution as $K_m = K_S + K_{dip}$. From this expression, one can see that strong dipolar coupling (for large L and small δ) would induce a switching of the easy axis into a hard one (if $K_m < 0$). In the present case, the magnetostatic contribution K_m is positive and is overall still dominated by shape effects since the easy axis is oriented along the average axis direction of the FNWs assemblies. Moreover taking L as the thickness of the films and using δ values obtained for d_3 and d_5 gives a $|K_{dip}|/K_S$ ratio of the order of 20 % to 30 %. A more precise estimate would require taking into account the orientation distribution

and the effect of in-plane disorder. Another important point is that both magnetostatic contributions do not depend on the temperature in the range where M_s is constant.

The global magnetic behavior for both samples is similar but some peculiarities can be observed. For d_5 the coercive field in the IP direction is higher than for d_3 at all temperatures. As has already been discussed above, this can be associated to a higher misalignment found for the objects in the d_5 sample. The coercive field in OP direction is small for d_5 at low temperature but its drop with the temperature is smaller than the one observed for d_3. The decay of the coercive field for sample d_5 is shown in Figure 5.5 and can be explained considering thermally activated reversal of magnetization.

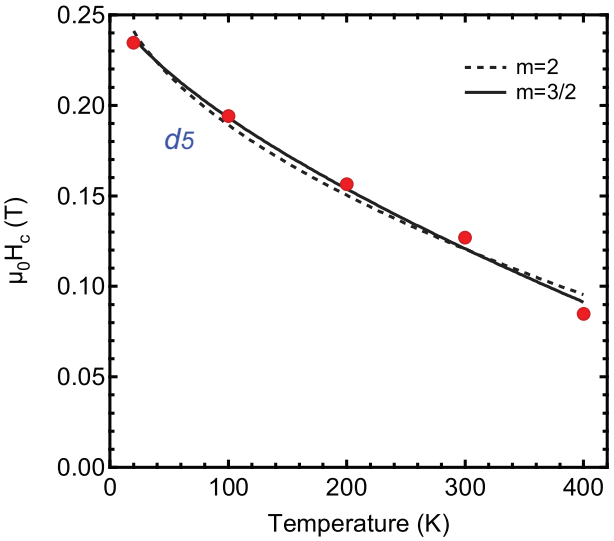

Figure 5.5: Coercive field (OP) as a function of temperature (red ∘) and its fit to equation (5.2) for d_5 sample considering two values for the m parameter.

As discussed in the previous section, in a case of coherent reversal of an entire FNW as a single magnetic domain the coercive field would not depend on temperature. This would happen because the energy barrier acting against the reversal is too high compared with thermal energy. Inserting inhomogeneities or defects existent in real structures we have a different picture. As developed in section 2.4.2 it is possible to account for the temperature behavior of coercive field with the following relationship:

$$H_c(T) = H_{c,0}\left[1 - \left(\frac{25k_BT}{E_0}\right)^{1/m}\right] \tag{5.2}$$

where $H_{c,0}$ is the coercive field at T=0 K, k_B is the Boltzmann constant, E_0 is the energy barrier that acts against the reversal of magnetization and m is a parameter that accounts for the symmetry of energy landscape of the reversal mechanism. Figure 5.5 also presents the fits considering the Equation (5.2). The fits give satisfactory results with the evolution

of the coercive field quite well reproduced both for m=$\frac{3}{2}$ and m=2. Both exponents lead to roughly the same values as presented in Table 5.3.

Table 5.3: Summary of magnetic measurement at 20 K where the squareness is defined as M_r/M_s and H_c is the coercive field.

m	$\mu_0 H_{c,0}$ (T)	E_0 (eV)
$\frac{3}{2}$	0.26	1.6
2	0.28	1.9

The good agreement indicates clearly that the evolution of H_c can be reproduced by considering a temperature independent energy barrier related to K_m. The values obtained for E_0 and $H_{c,0}$ are also in quite good agreement with previous measurements by Zeng *et al.* for FNWs with diameter below d_{crit}=15 nm down to 5.5 nm ($E_0 \simeq$3 eV for 5.5 nm diameter and $\mu_0 H_{c,0}$=0.32 T, roughly one third of the anisotropy field) (ZENG et al., 2002). The major difference in our case lies in the fact that both m=$\frac{3}{2}$ and m=2 power laws fit the data in contrast to the clear failure of the quadratic law reported by Zeng *et al.* We will return to this point in the discussion of the magnetic viscosity measurements performed on this sample. Figure present the coercive field behavior as a function of the temperature and also the fits for both m=2 and m=$\frac{3}{2}$(dotted and dashed line). As can be seen in the figure, the coercive field for sample d_3 as a function of the temperature could not be fitted considering equation (5.2).

To fit correctly the experimental behavior, we must consider another source of magnetic anisotropy, like the magnetocrystalline anisotropy. The assumption that magnetocrystalline might be important to explain the magnetic behavior of samples is related with the presence of majority hcp grains, as was attested by the structural characterization described in section 4.2.3.

The magnetocrystalline anisotropy of Co hcp is such that the c-axis of the hexagonal structure is an easy axis. Contrary to the previous magnetostatic contributions to anisotropy (shape and dipolar coupling), the magnetocrystalline anisotropy may depend strongly on the temperature (ONO; MAETA, 1989). The first term of the uniaxial magnetocrystalline anisotropy for bulk hcp Co, $K_{1,u}$, is roughly constant below 100 K and decreases beyond this limit, as shown in Figure 5.6(b). Depending on the crystalline orientation of hcp Co within the wires, this term can enhance the total anisotropy or compete with the magnetostatic term: if the c axis of cobalt is along the wire axis, then both contribution add; if the c axis lies perpendicular to the wire axis, then $K_{1,u}$ plays

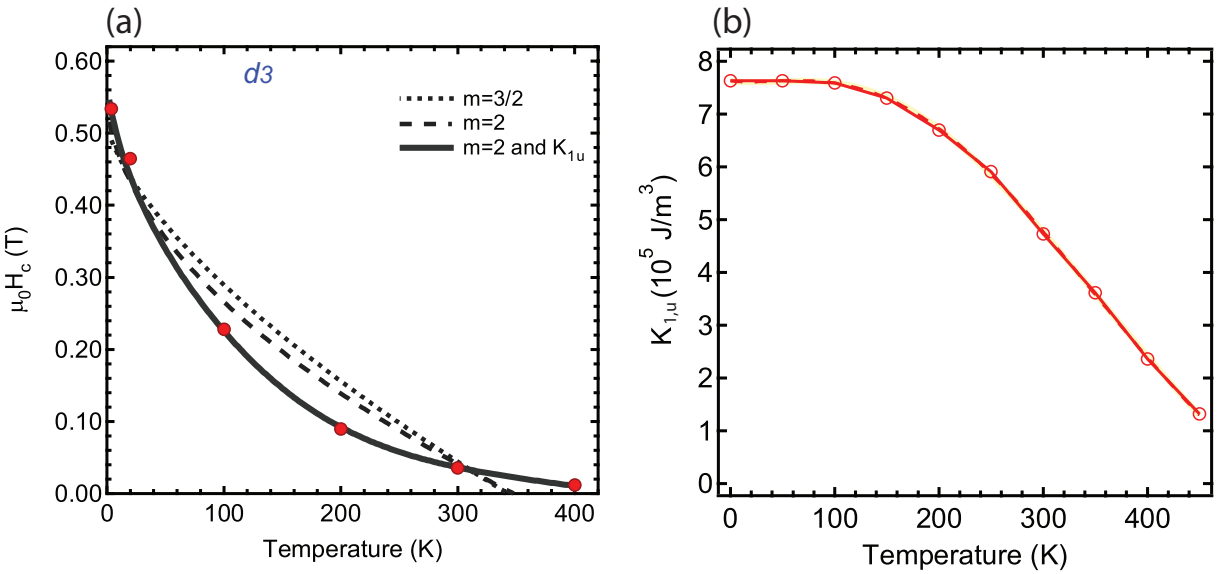

Figure 5.6: (a) Coercive field (OP) as a function of temperature (red ∘) and its fit to equation (5.2) for d_3 sample. (b) The temperature dependence of the first anisotropic constant $K_{1,u}$ for cobalt adapted from (ONO; MAETA, 1989)

against the magnetostatic term. To account for magnetocrystalline anisotropy contribution in the reversal, the energy barrier E_0 used in equation (5.2) was substituted. The new energy barrier is the sum of the constant term accounting for shape anisotropy and another term accounting for magnetocrystalline anisotropy. This second term carries the temperature dependence of $K_{1,u}$ shown in Figure 5.6(b). The new energy is written as $E^* = E_0 + \eta\ K_{1,u}$ where the parameter η scales as a volume and account for the mean volume of magnetic domain and also for a geometrical angular factor. The signal of this parameter η will then reflect the orientation of the c-axis of hcp Co. If it is negative there exists a competition between magnetostatic and magnetocrystalline contributions. Fitting the data with a $K_{1,u}$-related contribution gives quite good results as can be seen in Figure 5.6(a)[thick line]. For m=2, we obtain E_0=1.1±0.1 eV, $\mu_0 H_{c,0}$=0.63 T and η=-110 nm^3. As $E_0 > \eta K_{1,u}$, K_m is still the leading term in the magnetic anisotropy. Fitting the data with $m=\frac{3}{2}$ gives similar values of the parameters.

From the energy barrier extracted from the fit, one can deduce the effective activation volume $V^\star$ for magnetization reversal, if it occurs coherently, through $E_0 = \mu_0 H_{c,0} M_{s,0} V^\star$. For the d_3 sample, the estimated activation volume is $V^\star$=190 nm^3. This volume is smaller than the volume of the entire FNW, indicating that the magnetization does not reverse coherently in the whole FNW. Therefore the reversal is localized in regions of volume $V^\star$.

This volume corresponds to cylindrical sections having the same diameter d=3 nm as

the NWs and a length ℓ ∼27 nm, i.e. rods with an aspect ratio ℓ/d=9. It is important to note that the activation volume is bigger than the fit parameter η that has also volume units. This difference is related to an angular factor related to the mean direction of the hcp c-axis in the inner structure of Co FNW. These and other parameters derived from the fitting procedure of H_c for both samples are summarized in Table 5.4. The coercive

Table 5.4: Parameters deduced from fitting of H_c behavior as function of temperature for d_5 and d_3 samples.

	$\mu_0 H_{c,0}(T)$	E_0 (eV)	m	$V^\star$ (nm^3)	η (nm^3)	ℓ (nm)
d_5	0.26	1.6	1.5	700	0	30
d_3	0.63	1.1	2	-190	110	27

field at low T approaches the value predicted for rotation in unison. This combined with the fit to a quadratic law of $H_c(T)$ are strong indications in favor of a localized reversal mode following the Stoner-Wohlfarth model. Globally, the above analysis supports the idea that magnetization reversal in the 3 nm diameter FNWs occurs through a coherent rotation in localized sections of ∼27 nm length. The fact that $\eta K_{1,u}$ reduces the value of $E^\star$ indicates that, for the d_3 sample, the misorientation of the hcp grains in the FNWs is not random and that, furthermore, the c axis is oriented in average (over the localization volume) in a direction lying closer to the plane of the substrate than to the axis of the wires. This leads to an effective contribution of $K_{1,u}$ that tends to decrease the energy barrier imposed by the shape anisotropy in the plane perpendicular to the NWs axis. The magnetocrystalline anisotropy plays against the shape anisotropy.

According to this interpretation, the competition between $K_{1,u}$ and K_m is important at low temperatures in the interval where $K_{1,u}$ takes high values and is roughly constant. The effects are less pronounced above ∼ 200 K, where $K_{1,u}$ drops while the shape anisotropy remains constant. This is in line with the observed sharp drop of $\mu_0 \Delta H_{sw}$ between 100 and 300 K discussed in the previous section (Figure 5.4 and Table 5.2). Indeed the existence of a distribution of grains with different sizes and orientation of the c axis may result in a broad distribution of local effective anisotropy. This would result in a broad switching field distribution in the temperature range where $K_{1,u}$ is large as will be further discussed. After discussed the case of d_3 sample in details, we come back to d_5 sample case and the question that arises naturally is the following: How to council these results with the fact that η=0 works well in the case of 5 nm diameter FNWs?

The activation volume of d_5 was estimated in the same way and the value obtained

is V^*=700 nm. This volume corresponds to cylindrical sections having diameter d=5 nm as the NWs and a length ℓ ∼30 nm, i.e. rods with an aspect ratio ℓ/d=6. The fact that the reversal volume for d_5 is bigger than for d_3 is related with the higher energy barrier and explains the lower drop of H_c with the temperature. On the other hand the aspect ratio estimated for the d_3 sample is higher than for d_5. This results in a higher shape contribution and thus in a higher anisotropy field H_a. Therefore, d_3 has a higher H_c at low temperature.

Concerning the values of H_c and its variation with temperature, for d_5, the behavior is analogous to those reported previously for polycrystalline Co nanowires grown by electrodeposition (ZENG et al., 2002). The magnetic behavior of such samples could be described by invoking shape anisotropy only. In order to council the results for both samples the hypothesis that the polycrystalline character of the wires – more precisely, the reduced grain sizes and the grain orientation distribution – may be responsible for the absence of $K_{1,u}$-related contribution in d_5 is put forward.

In regions with typical size below the exchange length, the magnetic moments are aligned in order to minimize the exchange energy. In such regions, the magnetocrystalline anisotropy contribution would then be averaged by exchange. This latter contribution can be averaged out as the grain size and fraction of well-crystallized matter (inside the grains, as opposed to disorder in grain boundaries) tend towards zero. Such effect has been thoroughly studied previously in the framework of random anisotropy description of polycrystalline magnets (HERZER, 1991). In the case of very small grains with multiple orientations, as illustrated schematically in Figure 5.7(a), the contribution of $K_{1,u}$ will tend to vanish, leaving K_m as the only source of magnetic anisotropy. Alternatively, in the case of grains with lateral dimensions equal to the wire's diameter, the contribution of $K_{1,u}$ is not averaged out effectively [Figure 5.7(b)].

Another possible explanation for the distinct behavior of 3 nm and 5 nm diameter FNWs could be the influence of a possible temperature dependent term related to surface anisotropy. Indeed, in the present case, the surface/volume ratio evolves as $1/\rho$ with ρ the radius of the FNWs. Therefore, one expects a more pronounced influence of the surface term – if present – in the case of lower diameters. More precisely, the surface/volume ratio should be 5/3 times larger in the case of 3 nm diameters FNWs than for 5 nm diameter FNWs. This ratio is rather low and one can thus conclude that a surface-related contribution may not explain the strikingly dissimilar behavior observed. However, further studies on the effect of size reduction will be necessary to track a possible surface effect. It

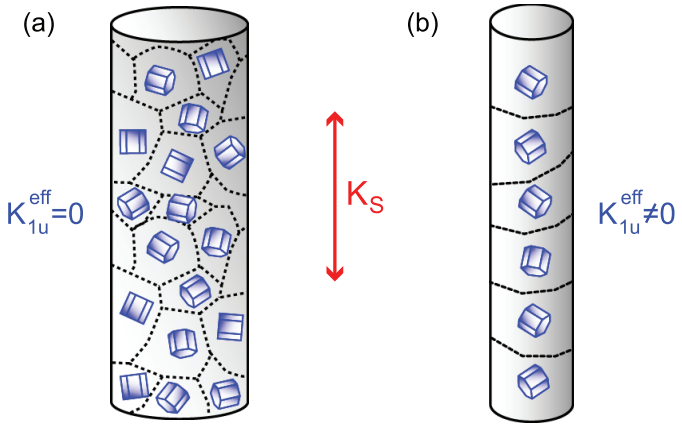

Figure 5.7: Schemes of polycrystalline FNWs with local orientation of the grains leading to (a) an effective averaging of $K_{1,u}$ and (b) a contribution of $K_{1,u}$ to the total magnetic anisotropy energy. The local magnetocrystalline anisotropy axis is the c axis of the hexagonal unit cell. The shape anisotropy axis is indicated by the double arrow.

is important to note that in this diameters range, the magnetic properties depend strongly on the crystalline quality of the wires and on the size of the grains. As a consequence, finding ways to enhance the crystalline quality of embedded Co wires is a prerequisite to further study on the magnetization reversal and dynamics in such objects.

We close this section by a comment on the fitting procedure used in the case of d_3 sample.

We emphasize the fact that this is a simplified approach that indicates a clear influence of the magnetocrystalline anisotropy on the observed magnetic behavior of d_3. However, the way this contribution is taken into account may be too simple. In particular, it neglects exchange coupling between grains and thus overestimate the impact of the magnetocrystalline anisotropy.

5.2 Magnetic viscosity

Magnetic viscosity (also known as magnetic after effect) is another phenomenon that permits to probe the thermally activated reversal of magnetic entities. This measurement technique consists in probing the sample's magnetization as a function of time after a step change of the applied magnetic field. This technique can give information about the reversal energy landscape present in the sample. Such experiments have been performed in bulk materials (GAUNT, 1976; COLLOCOTT; DUNLOP, 2002), thin films (ENDERS et al., 2005; LEIGHTON; SCHULLER, 2001) and also in ferromagnetic nanowires (GAO et al., 2006, 2007; MAURER et al., 2009; PAULUS et al., 2001; WEGROWE et al., 1997).

The magnetic viscosity measurements reported here were performed in a Quantum Design SQUID magnetometer (MPMS - 5S) and consist in monitoring the magnetization variation as a function of time after preparing the system in a given state. For each experiment, the procedure consists in saturating the sample with a high magnetic field (2 T) in a given sense (example in Figure 5.8(a)). After this step, the applied field is reversed to a given value (reverse field, see Figure 5.8(b)) and then the magnetization decay in time is probed. For the measurements reported here the waiting time was approximately 2400 seconds and the reverse fields vary between 0.1 and -0.9 T (the negative signal here means that the field is applied in the opposite sense of the initial saturating field). The direction of the applied field is along the axis of the nanowires, i.e. perpendicular to the plane of the film.

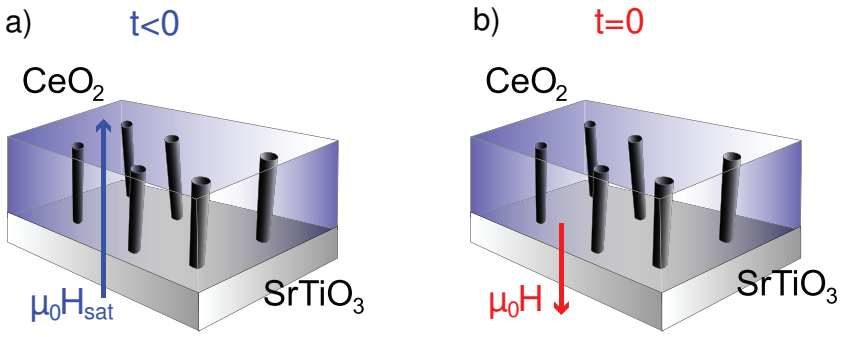

Figure 5.8: Procedure used for magnetic viscosity measurements in Co nanowires assemblies embedded in $CeO_2/SrTiO_3(001)$.

The measurements were performed for d_3 and d_5 samples at different temperatures always with the magnetic field applied along the easy axis direction, corresponding to the mean direction of the wires axis. The Figure 5.9 shows the time evolution of the magnetization for both samples after saturating the sample in one sense (2 T) and

subsequently applying a reverse field at t=0. Similar behavior were obtained for both d_3 and d_5 samples over the range of applied fields and temperatures studied. In all cases, the decay of the magnetization could be satisfactorily fitted by a logarithmic decay following Equation:

$$M(t) = M(t_0) - S(H,T)\ln(t/\tau_0) \tag{5.3}$$

where $S(H,T)$ is the magnetic viscosity coefficient already discussed in Section 2.4.3. The good agreement of the fit can be seen in Figure 5.9 where $M(t)$ is plotted as a function of t and $\ln(t)$.

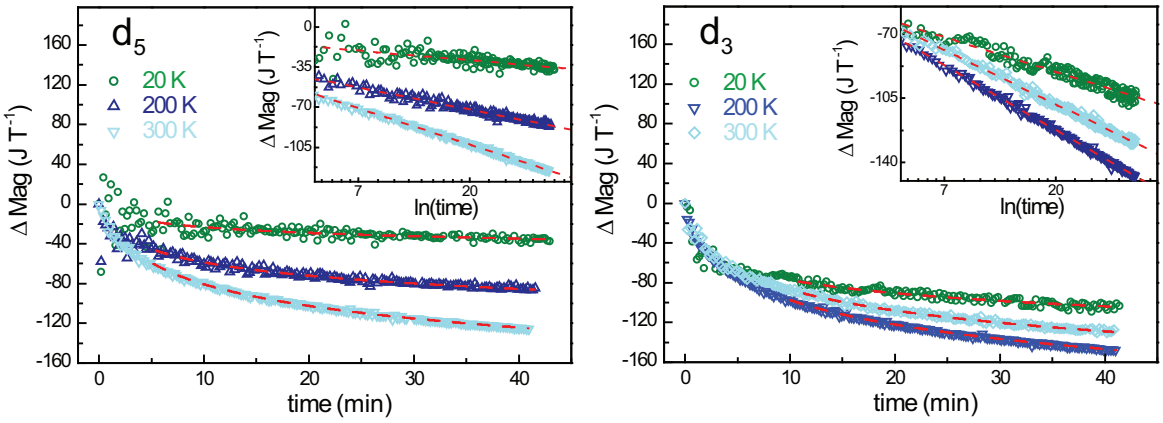

Figure 5.9: Typical measurements of time decay of the magnetization for both samples. The data have been obtained after reversing the field from 2 T to a reversal field to H_c(T) for both samples. The dashed red lines are the logarithmic fit. The inset present the magnetization decay plotted as a function of $\ln(t)$ and the dashed red lines are a linear fit allowing for straightforward extraction of the magnetic viscosity parameter.

From the results shown in Figure 5.9, it is possible to see that the variations of magnetization with time are higher for d_3 sample. This is in agreement with the lower energy barrier for the reversal in this sample discussed in the previous section. Moreover, even at low temperatures, it is still possible to measure magnetization decay and the values of viscosity parameter. Nevertheless an anomalous behavior is observed considering the thermal evolution for both samples. While the viscosity increases with T in the case of the d_5 sample, for the d_3 sample the behavior is totally different and a higher viscosity is obtained for intermediate temperature.

Going further, from these measurements the magnetic viscosity $S(H,T)$ was obtained in a broad range of fields and temperature for d_3 and d_5 samples. The results are summarized in Figure 5.10 that shows the evolution of S as a function of the applied

magnetic field for temperatures in the 20-350 K range.

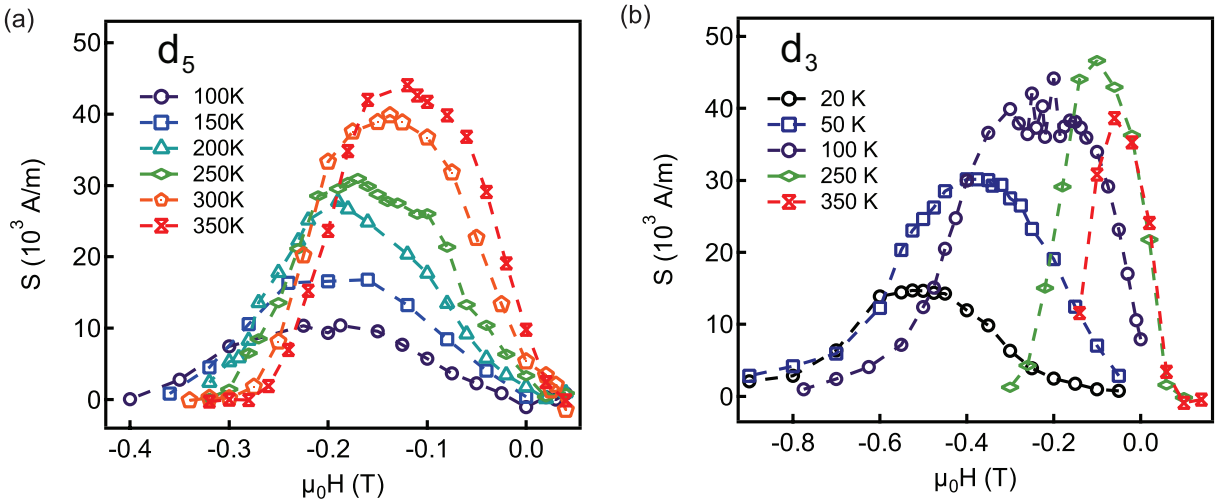

Figure 5.10: Magnetic viscosity coefficients $S(H,T)$ as a function of the applied field at various temperatures for samples d_5 (a) and d_3 (b).

At a given temperature, the $S(H)$ curve exhibits a bell-shaped curve. The maximum value of viscosity coefficient is located near the coercive field of the samples (reported in the previous section). This coincidence can be understood by considering the dependence of energy barriers on the magnetic field. Considering a homogeneous system with a single energy barrier, the barrier for reversal is zero when the applied field matches $\mu_0 H_0$ that corresponds to the switching field in this case. Now, considering a FNWs assembly that has a broad energy barriers distribution due to inhomogeneities, the coercive field is the field for which the highest proportion of barriers can be crossed. As consequence the magnetic viscosity peaks at $\mu_0 H = \mu_0 H_c$.

For d_5 sample, the $S(H)$ curves gain in intensity and the position of their maximum shifts towards lower applied fields (in magnitude) as the temperature increases. The shift of the field at which the viscosity is maximum is consistent with the evolution of $\mu_0 H_c$ reported in the previous section.

The evolution of the $S(H)$ curves is much more complex in the case of d_3. The position of the maximum follows the coercive field reported $\mu_0 H_c$ as occurs for d_5 but the maximum itself does not vary in a monotonous way with the temperature. Moreover, a decrease in the width of $S(H)$ is observed beyond 100 K, as could be deduced from Gaussian fit if the $S(H)_T$ curves. The width of curves found from the fit is shown in Figure 5.11 as a function of temperature for both samples.

The width behavior of d_3 contrasts with the constant width observed in the case of d_5. This clearly indicates the existence of two different regimes at low and high temperature.

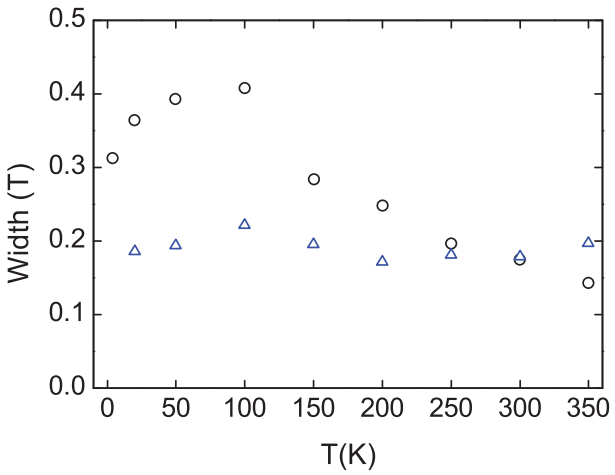

Figure 5.11: Full width at half maximum of $S(H)$ as a function of the temperature for d_3 (circles) and d_5 (triangles).

This width variation is similar to the one observed for the switching field distribution obtained by static measurements and indicates that the barrier distribution for d_3 sample varies with temperature, being wider at low temperatures.

In what follows, we will label $S_{max}(T)$ the maximal value of the magnetic viscosity at a given temperature T. Information on the nature of the energy barriers can be gained by analyzing the variation of $S_{max}(T)$. From the viscosity parameter, it is possible to extract the activation volume as was developed in section 2.4.3. The maximum value of the viscosity at a given temperature $S_{max}(T)$ corresponds to the most probable energy barrier. This would then correspond to the most probable value of the reversal volume $V_m^\star$ given by:

$$V_m^\star(T) = \frac{k_B T \chi_{irr}(T)}{\mu_0 M_s S_{max}(T)} \tag{5.4}$$

In order to use this relation and deduce $V_m^\star$ values from the data, the irreversible part of the susceptibility, χ_{irr} was determined from remnant magnetization loops. The procedure to access the irreversible part of susceptibility consists in measuring a hysteresis curve saturating the sample before each measuring. The obtained loop is then differentiated numerically. The $S_{max}(T)$ and $V^\star(T)$ data obtained for samples d_3 and d_5 are plotted in Figure 5.12.

Let us discuss first the results obtained for the d_5 FNW assembly. As shown in Figure 5.12(a), $S_{max}(T)$ varies linearly with the temperature. Such a linear variation is expected in the case of a temperature independent energy barrier distribution as can be seen by $S = 2M_S P(0) k_B T$ derived on section 2.4.3. From the linear fit and using a simple

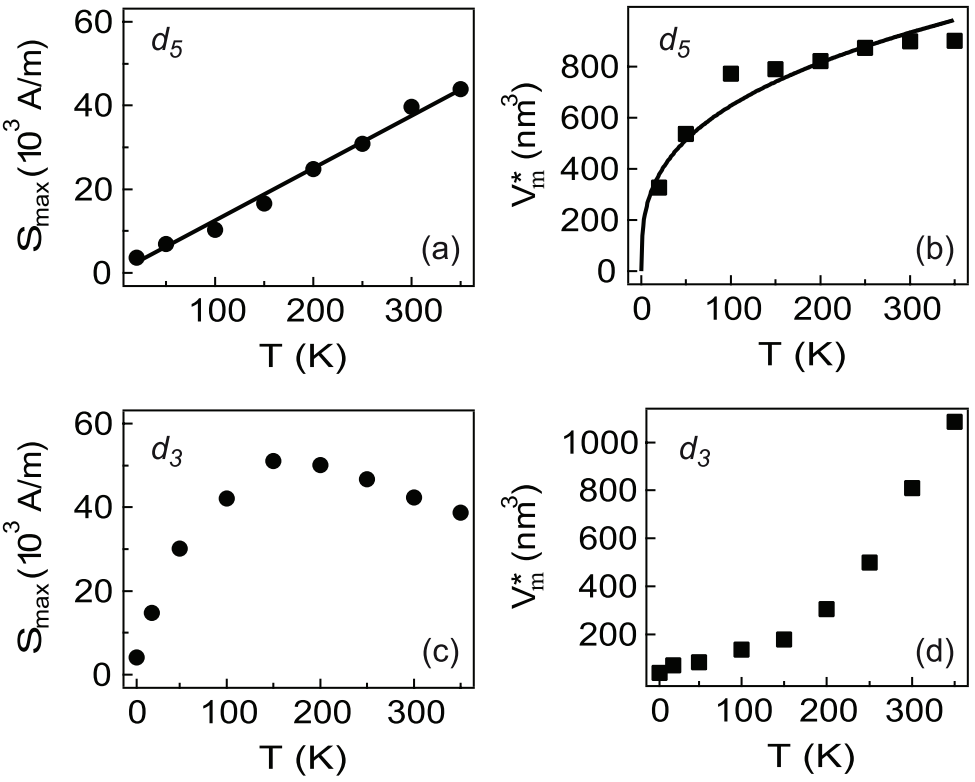

Figure 5.12: (a) Magnetic viscosity coefficient S_{max} of d_5 as a function of the temperature. The line is a linear fit. (b) Activation volume $V_m^\star$ of d_5 as a function of the temperature. The line is a fit according to Equation (5.4) with m=3/2. (c) Magnetic viscosity coefficient S_{max} of d_3 as a function of the temperature. (d) Activation volume $V^\star$ of d_3 as a function of the temperature.

squared barrier model (Equation (2.62)), the width of the distribution, ΔE_a could be extracted from the data. It is found that ΔE_a=2 eV. This width also corresponds to the highest value of the energy barrier present in the distribution in the framework of the rectangular approximation. Thus, the present value of ΔE_a is fully consistent with the mean value of E_a=1.6 eV determined on previous section by fitting the coercive field variation with Sharrock's formula (Equation (5.2)).

The variation of $V_m^\star$ could also be reproduced in the framework of a thermally activated reversal of the magnetization. The data could be fitted quite satisfactorily using the following expression:

$$V^\star = \frac{m}{2} V^{1/m} \left[\frac{k_B T}{K} \ln(\tau/\tau_0) \right]^{(m-1)/m} \tag{5.5}$$

with m=3/2, yielding a $T^{1/3}$ dependence of $V_m^\star$, as shown in Figure 5.12(b).

Using static measurements, fitting the $\mu_0 H_c(T)$ variation with Sharrock's formula

did not allow us to discriminate clearly between m=2 and m=3/2, both values giving comparable agreement of the fit with the data. In the present case, fitting $V^{\star}(T)$ with Equation (5.5) and m=2 (not shown) gives a clearly much poorer agreement than m=3/2. This 3/2 value is expected for systems with inhomogeneities and was also reported in previous studies of FNW grown in porous alumina templates (SELLMYER; ZHENG; SKOMSKI, 2001; ZENG et al., 2002).

Typical values of $V^{\star}$ is of the order of a few hundreds of nm^3, reaching 900 nm^3 at 300 K. The previous estimated value from statics measurements was 700 nm^3 and the difference between this two values is consistent with the difference between the energy barriers in the two cases discussed above. Such values are also comparable to activation volumes previously reported. Again, the fact that these volumes are smaller than the physical volume of a FNW indicates that the reversal is localized. Summarizing the results obtained for the d_5 FNWs sample, we observe the typical behavior expected for a system with thermally activated localized reversal and no dependence on the temperature of the energy barriers. This indicates that the barrier is related to magnetostatic terms, i.e. to the resultant from shape anisotropy (favoring an easy axis along the wires' axis) and dipolar coupling (favoring an easy axis in the plane perpendicular to the wire's axis). Here shape dominates over dipolar interactions and the resulting easy axis lies along the wires' axis. These two magnetostatic contributions to the anisotropy scale as M_s^2. In the temperature range studied, M_s is fairly constant and, thus, the anisotropy of the system does not depend on the temperature.

We now turn to the d_3 assembly results. The overall behavior is strikingly dissimilar, both for the viscosity and for the activation volume, when compared to the case of d_5 sample.

First of all, $S_{max}(T)$ does not vary linearly and do not even present a monotonous behavior with the temperature: it decreases beyond 150 K. Secondly, the variation of $V^{\star}$ cannot be described by Equation (5.5), neither with m=2 nor with m=3/2. The values of $V^{\star}$ indicate that the reversal process is strongly more localized in d_3 at low temperature. Beyond 150 K, the activation volume starts to increase much more rapidly than what is expected from a $T^{1/3}$ dependence. There is thus a progressive weakening of the localization of the reversal as the temperature increases. The magnetization reversal cannot be described with a temperature independent distribution of energy barriers for d_3 sample. The decrease of the $S(H)$ width with increasing temperature indicates a clear change in this distribution of reversal energy of system. As discussed previously,

such distribution is closely related to inhomogeneities in system. In the present case, a possible explanation is that the internal structure of the wires is the key to explain the observed changes in the variation of S and $V^\star$ with the temperature.

Let us then try to rationalize the observed behavior and explain weakening of the localization of the magnetization reversal. We consider wires made of hcp Co grains having their c axis strongly misaligned with respect to the axis of the wires, as illustrated in Figure 5.13. As the uniaxial magneto-crystalline anisotropy of hcp Co, $K_{1,u}$, is of the same order of magnitude than the shape anisotropy of the wires, a distribution of hcp grains, with varying size and/or orientation, within the wires will lead to a broad energy barrier distribution. Therefore, due to the competition of shape and magnetocrystalline anisotropies, an induced local variation of the anisotropy along the axis of the wires would occur, as depicted in Figure 5.13.

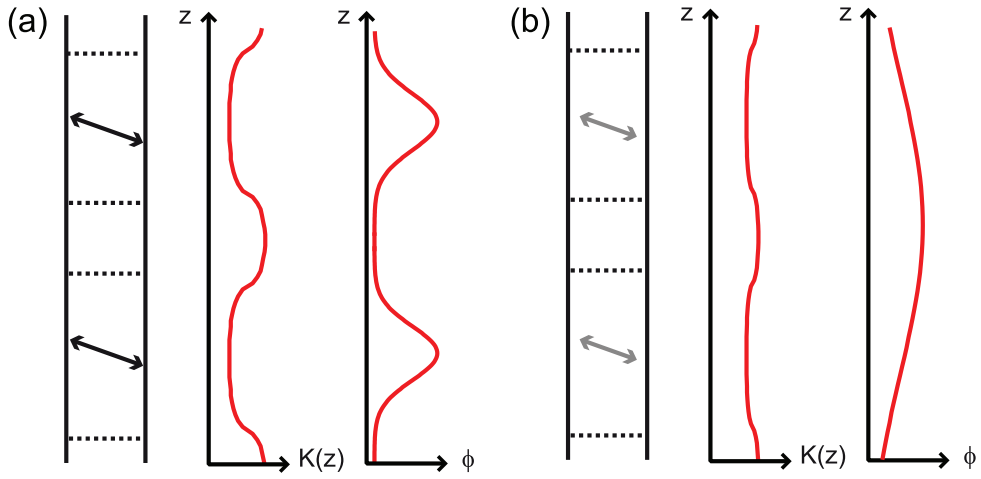

Figure 5.13: (a) Scheme illustrating the effect of local competition between magneto-crystalline and shape anisotropies, leading to a localized reversal of the magnetization. $K(z)$ is the local anisotropy constant that is reduced in grains having their c axis oriented along the direction indicated by the double arrows. ϕ is the angle between the local magnetization and the axis of the wire. (b) Same than (a) with a reduced value of the magneto-crystalline anisotropy.

Local variation of the anisotropy tends to induce the localization of the reversal in nanowires (SKOMSKI, 2003). Therefore, in wires having an inner structure such as the one schematized in Figure 5.13, such localization of the reversal process is expected. Again this is coherent with the reduced values of $V_m^\star$ at low temperature. As the temperature increases, $K_{1,u}$ drops as discussed in previous section (ONO; MAETA, 1989). This has two consequences: the local variation of the anisotropy are damped and the width of $P(E_a)$ decreases (the system can be considered as more homogeneous than at low temperature from a magnetic point of view) . Smaller variation of the anisotropy then leads to a

weakening of the localization of the reversal, as illustrated in Figure 5.13(b). Thus, the observed increase of $V^\star$ at higher temperatures may be a consequence of a weakening of the localization effects because of the drop of $K_{1,u}$.

5.3 Preliminary conclusions

Having determined the presence of self-assembled Co ferromagnetic nanowires, we turned our attention to their specific magnetic properties. Two ferromagnetic nanowires assemblies were used in this study with narrow diameters distribution centered on 3 nm (d_3 sample) and 5 nm (d_5 sample). The reversal mechanism has been investigated and distinct behaviors were evidenced in the two systems. In both samples, the magnetic anisotropy is dominated by the shape anisotropy contribution and the reversal is localized. Nevertheless, for d_5 the temperature dependence of the coercive field can be described by a thermally activated reversal over a temperature independent energy barrier. For d_3, the independent barrier model cannot explain the behavior. It was proposed that this failure is associated to a competition between magnetocrystalline and shape anisotropy, leading to an effective temperature dependent anisotropy.

In order to obtain a more detailed picture of the magnetization reversal, viscosity measurements have been carried out in a broad range of applied reversal field and temperature. For d_5 the results corroborate the preceding conclusions of thermally activated reversal over an energy barrier distribution that is independent of the temperature. Moreover, the activation volume could be estimated and its behavior is quite well fitted by the expression expected for a temperature independent energy barrier. For d_3, we put forward the hypothesis that competition between magnetocrystalline and shape anisotropies leads to an effective temperature dependent energy barrier distribution. The magneto-viscosity measurements permitted the observation of two different behaviors of the energy barriers distribution. This can be rationalized in the framework of our hypothesis: at low temperature, the magnetocrystalline anisotropy induces a strong localization, with small activation volumes and a broad energy barriers distribution due to inhomogeneities. Increasing the temperature, the contribution of the magnetocrystalline anisotropy is less important, resulting in a more narrow energy distribution.

6 *Inner structure of nanowires and anisotropy*

The previous chapter discussed the magnetic properties of the FNW assemblies and stressed a different behavior when comparing the samples. This different behavior has been tentatively linked to a strong influence of the magnetocrystalline anisotropy for one of the FNW assemblies. To verify this hypothesis, the internal structure of wires was investigated.

6.1 Inner structure: analysis of HRTEM images

In order to get information about the grain structure inside the FNWs, the HRTEM images were analyzed by Fast Fourier Transform (FFT) and filtering. The FFT process gives information about repetition patterns occurring in an image. In HRTEM images, these patterns permit to obtain information about the crystalline structure of the samples. In practice, the FFT of HRTEM image is analogous to the electron diffraction and can indicate the crystalline arrangement of the sample.

Figure 6.1 presents the theoretical diffraction patterns for CeO_2 fluorite crystalline structure and for the hexagonal structure of Co. The zone axis has been chosen to correspond to the geometry of HRTEM images. The blue lines represent the [111] direction of CeO_2 and [0001] direction of hcp Co. We will justify the fact that we are indexing the pattern considering the hcp structure of Co *a posteriori*.

In Figure 6.2(a), a HRTEM image of d_3 is shown in which two nanowires can be distinguished. The FFT of this image is presented in Figure 6.2(b). The presence of nanowires results in additional spots in the FFT that cannot be associated to any composite considering single diffraction. A scheme identifying the spots corresponding to CeO_2 in green and the additional spots in blue is presented in Figure 6.2(c). In order to index these spots, their distances to the center of the FFT pattern were measured.

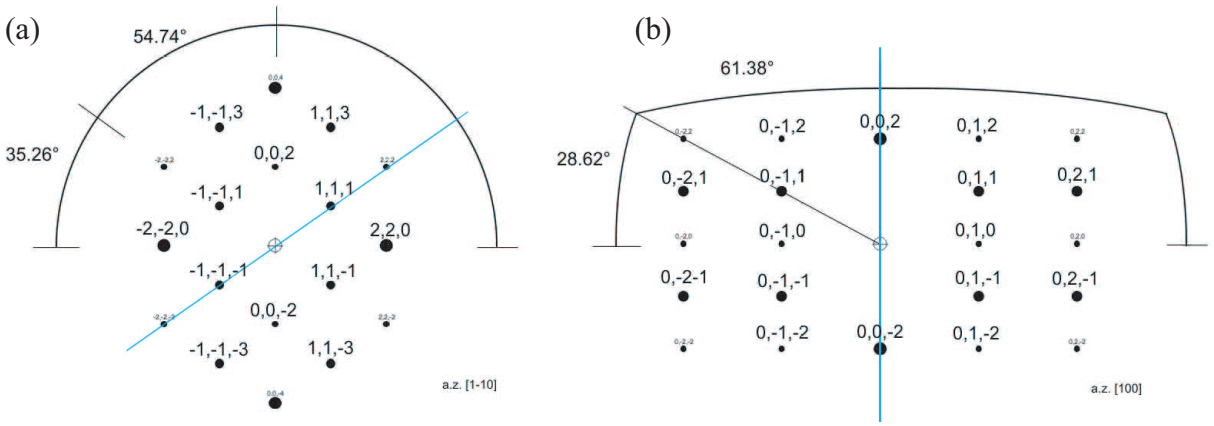

Figure 6.1: Diffraction patterns of cubic CeO_2 (a) and hexagonal Co (b) at a zone axis corresponding to the geometry of HRTEM images. The blue lines represent the [111] direction of CeO_2 and [0001] direction of hcp Co (Adapted from (BONILLA, 2010)).

For example, along the [111] direction, the distance between the CeO_2 spots on FFT is d_{FFT} =3.16 nm^{-1}. This corresponds to an inter-planar distance on real space of d_{Real} = 3.16 Å , closely matching with the CeO_2 distance along [111], $d_{CeO_2;[111]}$ = 3.12 Å.

The additional spots are located at a shorter distance than the CeO_2 spots. This would correspond to a structure with inter-planar distance bigger than 3.12 Å, what do not match with any known composite. These spots can only be indexed considering the multiple diffraction process. As its name suggests, multiple diffraction means that the electron beam is diffracted several times, but in different crystalline structures. A multiple diffraction pattern is much more complex than the simple superposition of two diffraction patterns. In order to account for the multiple diffraction spots appearing in the FFT, one must consider each diffracted spot of the first structure as a new incident beam for the second crystalline structure. This simulation was performed with Francisco Bonilla (INSP), considering the two diffraction patterns presented in Figure 6.1. It was assumed that the [0001] direction of hcp Co is parallel to the one of the [111] directions of CeO_2. The resulting patterns obtained for this case considering simple superposition of patterns(a) and double diffraction process (b) are presented in Figure 6.3. For the simulation, diffraction was considered to occur first in CeO_2 with a second diffraction step in Co. For this last step, only the (0002) plane of hcp Co was considered.

Comparing the FFT (shown in Figure 6.2(b)) with the simulated double diffraction pattern (shown in Figure 6.3(b)), it can be seen that the assumption that the c-axis of hexagonal Co is parallel to one of the CeO_2 [111] direction can explain the additional spots appearing in the FFT.

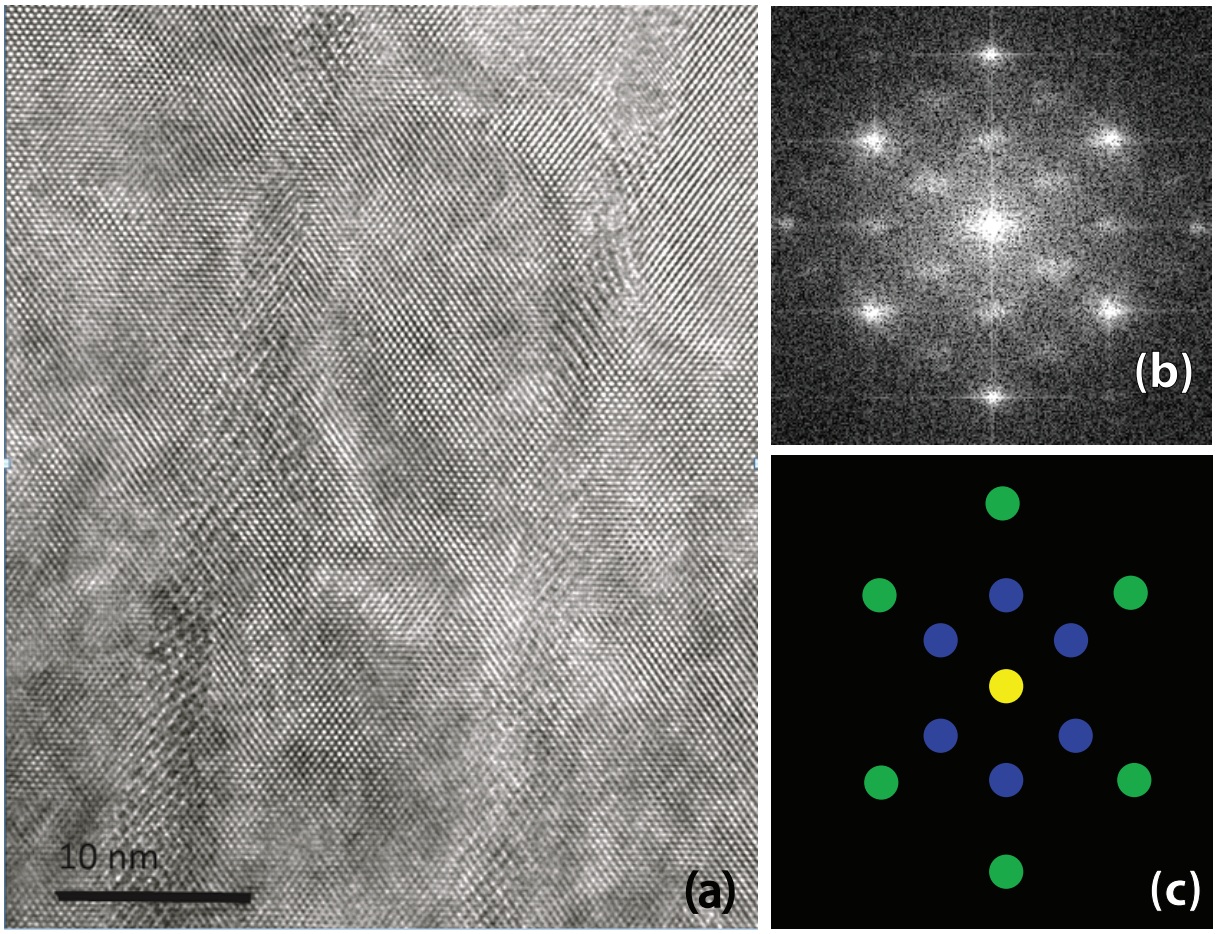

Figure 6.2: (a) HRTEM image of a region of d_3 sample containing two nanowires. (b) FFT of the HRTEM image. (c) Scheme showing in yellow the transmitted beam, in green the spots corresponding to the CeO_2 matrix and in blue the additional spots corresponding to double diffraction.

Recent experiments, not reported in this manuscript, show that it is also possible to form Ni nanowires in CeO_2 using the same recipe as the one used for Co FNWs. In this case, Ni, that has fcc structure, grows epitaxially in the matrix. More precisely, a cube on cube epitaxy is observed with the cubic unit cell of Ni aligned with the cubic unit cell of CeO_2. Taking this information into account, the assumed arrangement for hcp Co can be rationalized supposing the following picture. The cobalt has a hexagonal structure at temperatures up to 420°C when it suffers a transition to a cubic structure (fcc). Hence, the growth temperature is high enough to guarantee the cubic structure of Co during the growth. Moreover, the lattice parameter of fcc Co and fcc Ni are nearly identical. Therefore, we make the assumption that during the growth, Co forms in the fcc structure with its unit cell aligned with the one of the CeO_2 matrix.

After the growth, during the cooling step down to room temperature, the Co passes through the transition to a hexagonal structure. During this transformation, a [111]

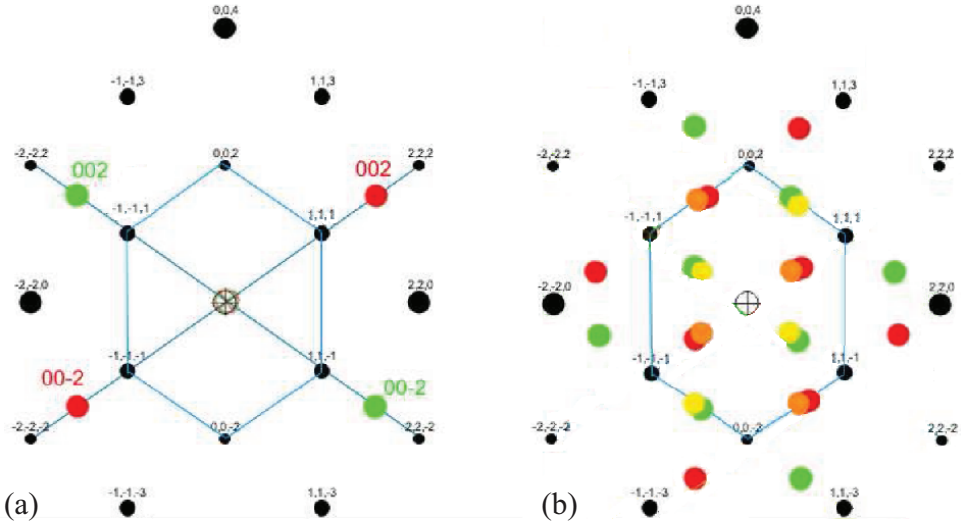

Figure 6.3: Diffraction patterns: (a) simple diffraction and (b) double diffraction. Red and orange spots corresponds to $[111]_{CeO_2} \parallel [0001]_{Co}$ and green and yellow corresponds to $[\bar{1}\bar{1}1]_{CeO_2} \parallel [0001]_{Co}$ (Adapted from (BONILLA, 2010)).

direction of cubic Co can transform in the [0001] direction of hexagonal Co. As this transformation is also accompanied by a change in the unit cell volume, the strain caused by the matrix induces the formation of grains. These grains will be mostly textured with c-axis of hexagonal Co parallel to one of the four possible [111] directions of the matrix. Indeed, the existence of such texture is in agreement with the absence of fcc Co related peaks in X-ray diffraction of thin films. Considering the grains formation, it is then expected that the grains formed have equal probability of pointing parallel to one of the four [111] matrix directions. In the geometry of HRTEM images, only two [111] directions are accessible and other two are perpendicular to the image plane. It is thus expected that grains with two different orientations can be observed. From the simulation of the double diffraction patterns, it is possible to differentiate the grain orientations as can be seen in Figure 6.3(b) by the different colors.

It is important to note that the FFT presented in Figure 6.2(b) contains information about the matrix and also about the different grains inside the FNWs. In order to differentiate the grain directions in the images, the FFT process was realized in selected small regions of the HRTEM images. In some selected regions, the FFT presents only double diffraction spots linked to one of the possible grain directions. After performing the FFT in some of these selected regions, an inverse FFT is performed using a mask to consider only the information contained in the double diffracted spots. With this process, one obtains an image in which fringes appear in localized regions inside the nanowires. These regions can then be identified as grains of well-defined orientation of the c-axis. The

Figure 6.4 presents the results of the filtering process for the two possible directions of the grains. The images presented are zooms from different regions of the HRTEM presented in Figure 6.2(a).

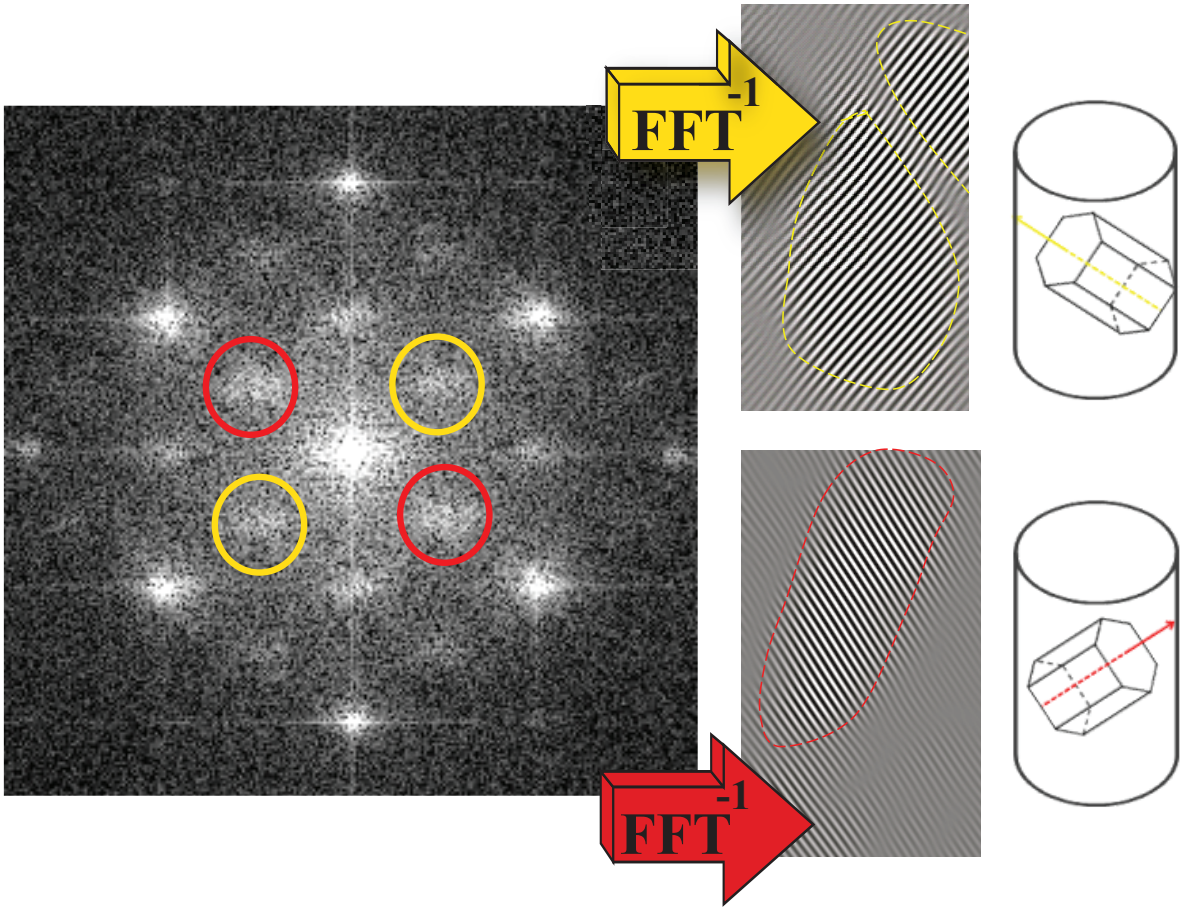

Figure 6.4: Inverse FFT image considering only the double diffraction spots inside the yellow and red circles for the two possible directions of the hexagonal c-axis of hcp Co inside the nanowires.

The process described above was performed for the two FNW assemblies. The FFT is performed for small regions of one HRTEM image and the FFT presenting double diffraction are selected. Applying a filter on FFT and performing an inverse FFT conserving only the double diffraction spots, the grains with a given direction are evidenced. Performing this process in different regions, one can extract a map of the grains inside the FNWs. The Figure 6.5 shows the results of the filtering of images for d_3 and the Figure 6.6 for d_5.

The results for both samples corroborate some conclusions of the previous sections. For instance, considering the d_3 FNW assembly, the grains are bigger and have a higher aspect ratio than for d_5. For d_5, the domains do not have the same diameter as that of the wire, are smaller and are more numerous. Moreover, for d_5 grains with different directions

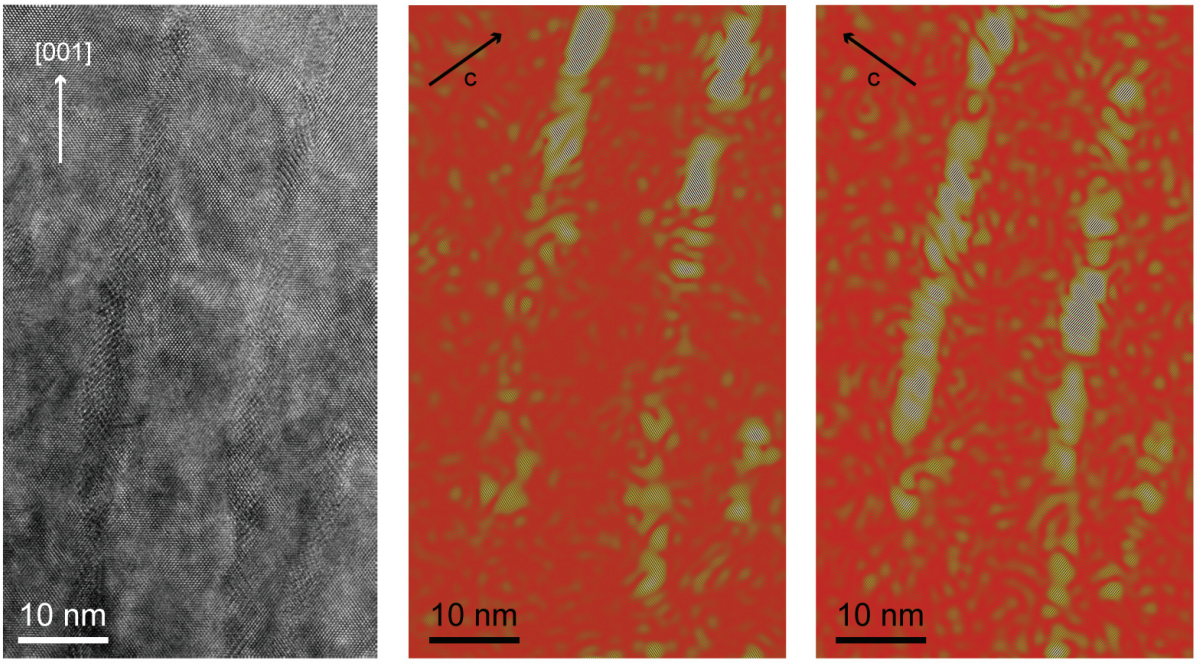

Figure 6.5: HRTEM image for d_3 showing two FNWs and the hexagonal grains pointing in two of the <111> directions of the matrix.

are superposed to each other. This does not occur in d_3. This picture is in agreement with the hypothesis that the magnetocrystalline anisotropy contribution is averaged to zero in the d_5 FNW assembly.

It is important to stress here that the crystallographic grains and magnetic domains are not the same. In the previous sections, we discussed the size and size variation of magnetic domains where the localized reversal occurs. Indeed, the magnetic domains are the result of an energy balance taking into consideration the crystallographic domains, the anisotropies and the coupling between different grains.

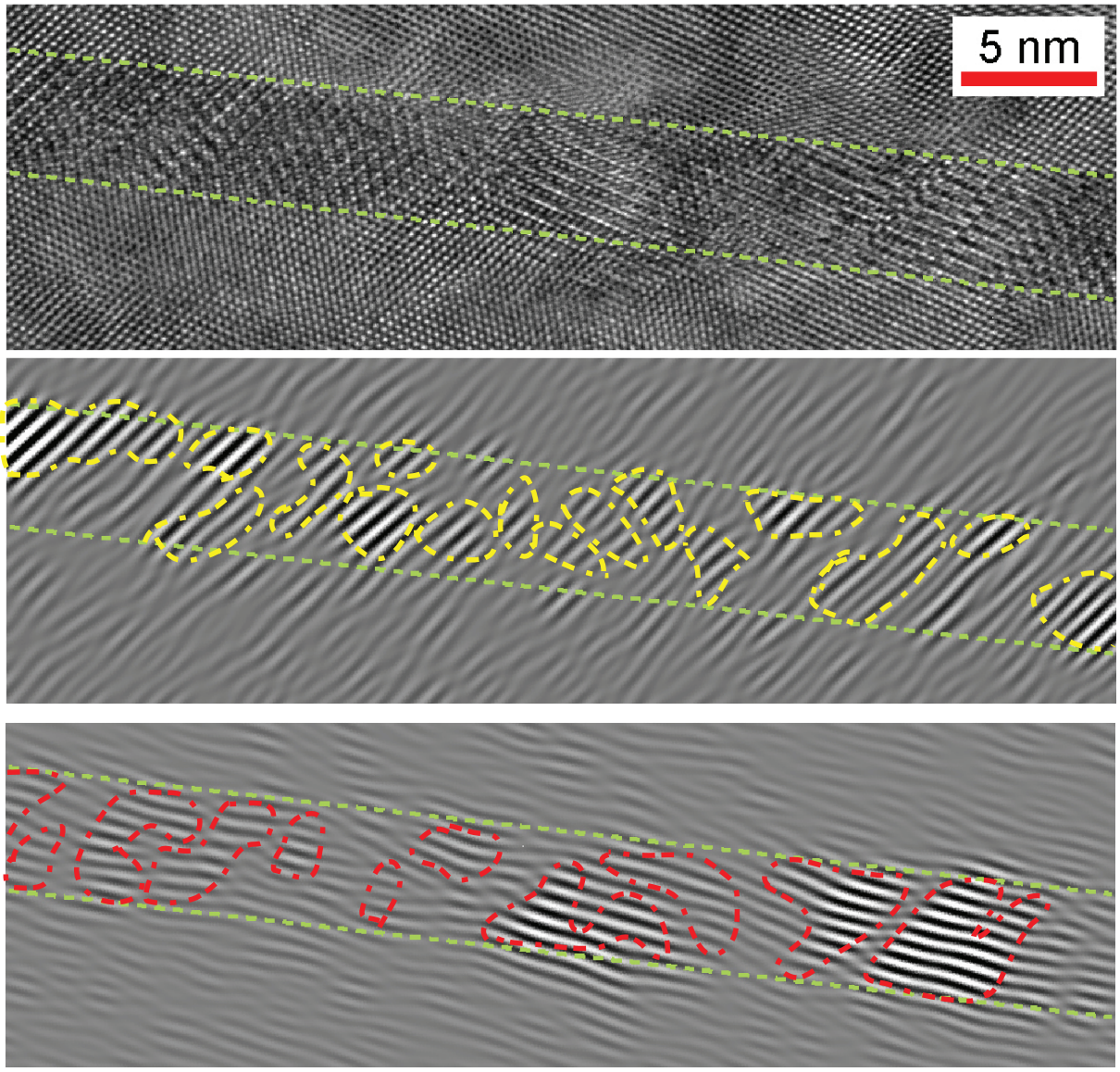

Figure 6.6: HRTEM image for d_5 and the hexagonal grains pointing in two of the <111> directions of the matrix.

6.2 Magnetic anisotropy: a FMR study

From the preceding results, the nanowires in d_3 are made of oriented hcp Co grains. Because hcp Co has uniaxial magnetocrystalline anisotropy of the same order of magnitude as the shape anisotropy, the internal structure of the wires should have a profound impact on the effective magnetic anisotropy of d_3.

In order to get more insight into the anisotropy, the systems were investigated by means of ferromagnetic resonance (FMR). FMR is a very important technique to probe the magnetic properties of materials and, more precisely, to investigate the magnetic anisotropy of samples (LINDNER; FARLE, 2088). The usual configuration of a FMR experiment and some details of the application of the technique for FNW are described in section 3.5.

FMR experiments were performed in order to verify the existence of an anisotropic behavior in the plane of the d_3 sample as would be expected considering the texture of grains described in the previous section. Besides that, FMR is also a handy tool to evaluate the values of the magnetic anisotropy constants. Before reporting a more detailed analysis of the spectra, some general trends about the data is summarized here.

The ferromagnetic resonance spectra were measured in Q-band (34 GHz). This condition is necessary to reach the resonance in ferromagnetic Co FNW because this kind of system has a large anisotropy field (CHIPARA et al., 2011). Generally, the shape of the microwave absorption as a function of the applied magnetic field is expected to be the derivative of a Lorentzian peak (SLICHTER, 1990). In the results reported here, it was possible to fit the experimental spectra using the superposition of a Lorentzian peak derivative and a linear background only for the θ-scan geometry. For the ϕ-scan geometry, the spectra are more complex, in some cases with the presence of more than one resonance and it was not possible to fit the data satisfactorily with a Lorentzian shape.

The resonance fields were extracted by a fitting procedure or by graphical determination. The values obtained vary from 0.3 T with applied field parallel to the FNW axis to 1.6 T with field perpendicular to them for the d_3 sample. The width of the observed resonances vary with angle and displays a minimum width of $\sim$0.2 T and maximum width $\sim$0.8 T. In order to account for the errors due to misalignment of the films and also for the errors in the resonance field determination, errors bars are inserted in the results reported. The values of errors bar are $\pm$10% of the minimum resonance

width (∼200 Oe) for the resonance fields and ±5° for the angles.

6.2.1 Ferromagnetic resonance for the d_3 sample

FMR spectra of d_3 sample were recorded at room and low temperature in θ-scan and ϕ-scan. At low temperature, for H_{app} perpendicular to the wires, the resonance field was beyond the upper limit of the applied field. Thus, it was not possible to monitor the complete angular dependence of the resonance field at low T. In what follows, the room-temperature set of data is discussed first.

Room temperature resonance experiments have been performed in θ-scan for different ϕ angles. Selected spectra for θ-scan at $\phi = 0°$ and 45° are presented in Figure 6.7 (a) and (b) respectively.

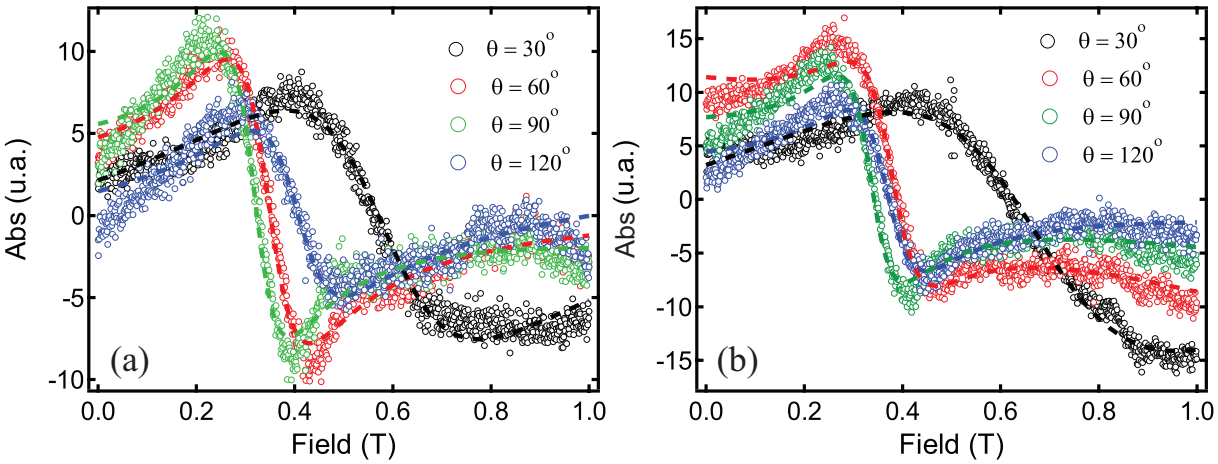

Figure 6.7: FMR spectra of d_3 sample for selected values of θ, as indicated, for ϕ=0° (a) and ϕ=45° (b). The symbols are the experimental data and the dashed lines are the fits considering a Lorentzian peak derivative.

Figure 6.8 presents the resonance fields extracted from the FMR spectra. The same results are in Figure 6.8(a) and 6.8(b) but they have different zoom in order to show more clearly that the resonance field does not change with the ϕ angle. The difference observed between the curves is most likely due to a small misalignment of the sample and lies in the expected error range.

For some ϕ angles in Figure 6.8(a), the resonance were measured only for θ between 20° and 160° but this resonance can be observed at high field. The high difference of resonance for applied field parallel or perpendicular to the plane of thin films allows us to confirm the existence of a large anisotropy in the system with an easy axis perpendicular to its surface. Such anisotropy is expected considering the high aspect ratio and orientation of

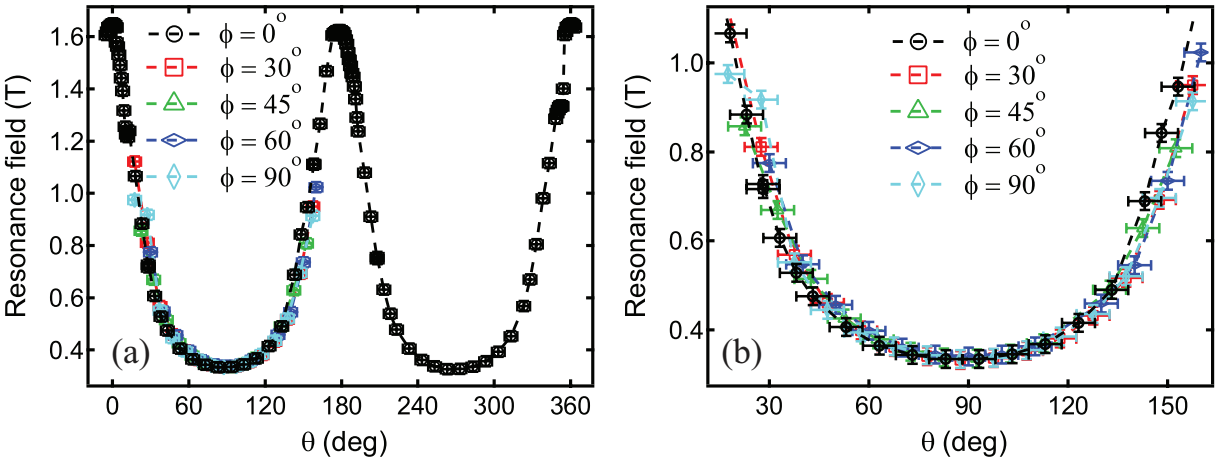

Figure 6.8: Resonance field for θ-scan for different ϕ angles. In (a) results are presented for the full 360 degrees range and (b) shows the same data in a zoom.

the FNW (CHIPARA et al., 2011).

The results obtained in the ϕ-scan geometry are presented in Figure 6.9. The spectra recorded at different ϕ angles are displayed in Figure 6.9(a). These spectra have a shape approaching that of a Lorentzian derivative, but it was not possible to fit these spectra with such a function and a more careful inspection reveals that the two lobes of the curve profile are not symmetric. This asymmetry is probably due to the fact that the saturation field of the sample in this geometry is of the same order of the resonance field. Therefore, for the first lobe, the sample is not saturated and one observes a sheared behavior.

The resonance field variation in the plane of the thin film is presented in Figure 6.9(b). The observed variation indicates the presence of an additional source of anisotropy (the uniaxial anisotropy related to shape is not the only source of anisotropy). This anisotropy has a 4-fold symmetry in the plane and seems to correspond to the presence of an anisotropy typically observed in cubic materials. This anisotropy can be explained based on the peculiar structural properties of the system. As described in the previous section, the cobalt in the FNWs is crystallized in the hexagonal structure with the c-axis of the hexagonal pointing preferentially in a <111> direction of the matrix. The projection of this anisotropy in the plane of sample thus produces easy in-plane directions along <110> and harder directions along <100>.

Simulation

Simulations have been performed in the framework of the Smith-Beljers formalism (LINDNER; FARLE, 2088) in order to estimate the resonance fields, using

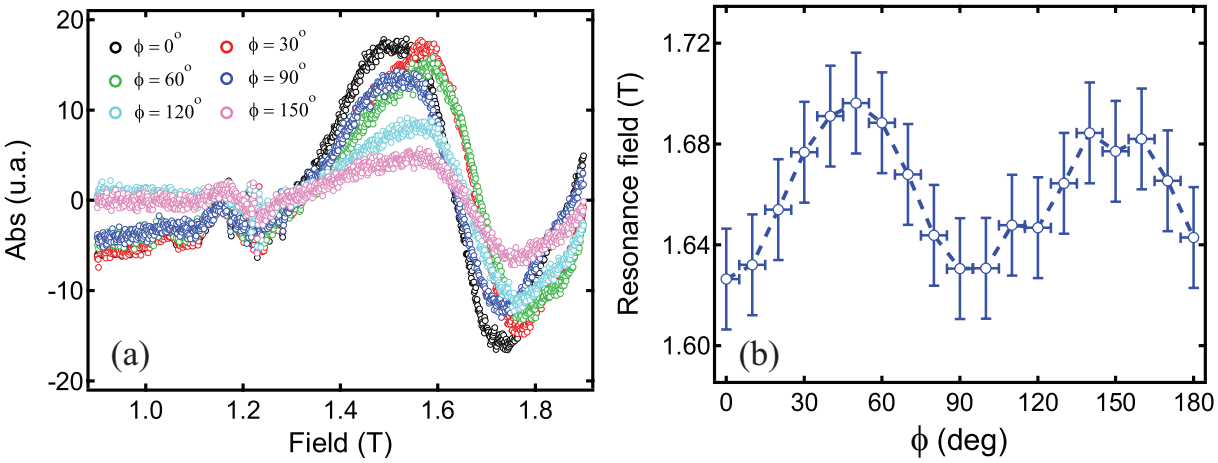

Figure 6.9: Spectra for the d_3 sample taken in the plane of the film (a) and resonance field variation with ϕ angle (b).

Mathematica software. In the simulations, the specific texture of the grains determined by HRTEM analysis of d_3 is accounted for. For this, it was considered that the magnetic domains have cylinder shape and are formed by only one crystallographic domain out of the 4 possible considering that the c-axis of hcp Co is parallel to a <111> direction of the matrix. Therefore the three energetic contributions for the magnetic free energy of the system are:

- Zeeman effect, i.e. the interaction between magnetization and applied magnetic field;
- shape of magnetic domain (assuming the magnetic domain as a cylinder with a given aspect ratio);
- magnetocrystalline anisotropy (considering that in the above-mentioned magnetic domain, the Co hcp grain is oriented in one of the $< 111 >$ directions of matrix). The resonance field for each of the four possible directions of Co c-axis was calculated separately.

The magnetic free energy used in the simulation was then:

$$F(\theta,\phi) = -\mu_0 \mathbf{M}.\mathbf{H} + \frac{\mu_0 M_S^2}{2}\left(\frac{(1-N_Z)\sin^2\theta}{2} + N_Z\cos^2\theta\right) - \frac{K_{1,u}}{M_S^2}(\mathbf{G}.\mathbf{M})^2 \qquad (6.1)$$

where $\mathbf{M} = M_S(\cos(\phi)\sin(\theta), \sin(\phi)\sin(\theta), \cos(\theta))$ is the magnetization vector and M_S the Co bulk magnetization saturation; μ_0 is the vacuum magnetic permeability; $\mathbf{H} = H(\cos(\phi_B)\sin(\theta_B), \sin(\phi_B)\sin(\theta_B), \cos(\theta_B))$ is the applied magnetic field with intensity H; N_Z is the demagnetizing factor on the direction of the wire axis; $K_{1,u}$ is the

magnetocrystalline constant and **G** is a director vector of hcp c-axis that assumes in our case the values $\frac{1}{\sqrt{3}}(1,1,1)$, $\frac{1}{\sqrt{3}}(-1,1,1)$, $\frac{1}{\sqrt{3}}(1,-1,1)$, $\frac{1}{\sqrt{3}}(-1,-1,1)$ for each one of the four possible grain directions.

Using the Smith-Beljers formalism, the resonance frequency ω_R can be extracted from (LINDNER; FARLE, 2088):

$$\left(\frac{\omega_R}{\gamma}\right)^2 = \frac{1}{M\sin\theta}\left[\frac{\partial^2 F(\theta,\phi)}{\partial\theta^2}\frac{\partial^2 F(\theta,\phi)}{\partial\phi^2} - \left(\frac{\partial^2 F(\theta,\phi)}{\partial\theta\partial\phi}\right)^2\right] \tag{6.2}$$

where γ is a constant defined as $\gamma = \frac{g\mu_B}{\hbar}$ with g being the gyromagnetic factor, μ_B being the Bohr magneton and $\hbar$ being the reduced Plank constant; $F(\theta,\phi)$ is the magnetic free energy of the system that depends on magnetization angles θ and ϕ.

In the simulation, the Co bulk value for saturation magnetization was used (1.424×10^6 A/m at room temperature). The value for demagnetizing factor N_Z and for the magnetocrystalline constant $K_{1,u}$ are the adjustable parameters of the simulations. For simulations of θ-scan, the ϕ angle was chosen in a way that the plane probed is the plane containing a <111> direction.

The values for demagnetizing factor and magnetocrystalline constant used in simulations were varied in order to find out the better agreement with the experimental results. The bulk value of the leading magnetocrystalline constant of hcp Co, $K_{1,u}$, is 7.2×10^5 J/m^3 at low temperature and 4.2×10^5 J/m^3 at room temperature (ONO; MAETA, 1989). For the demagnetizing factor the value was varied from zero (value expected for an infinite cylinder) up to 0.1. It is possible to associate this value to a given aspect ratio, but this depends on some geometrical assumptions. Theoretical calculations performed by Chen *et al.* (CHEN; BRUG; GOLDFARB, 1991) present values for the demagnetizing factor considering either an ellipsoid or a cylinder calculated using inductance formulas. In what follows, the aspect ratio cited is based on these calculations.

Figure 6.10 presents some results of simulation for values of the parameters indicated in the legend. In Figure 6.10(a), (b), (c) and (e) the aspect ratio (L/r) of magnetic domain is held constant while the $K_{1,u}$ value was varied. In Figure 6.10 (d) and (f) the aspect ratio was varied and magnetocrystalline anisotropy held constant. The resonances (a), (c) and (e) are for θ-scan and (b), (d) and (f) are for ϕ-scan.

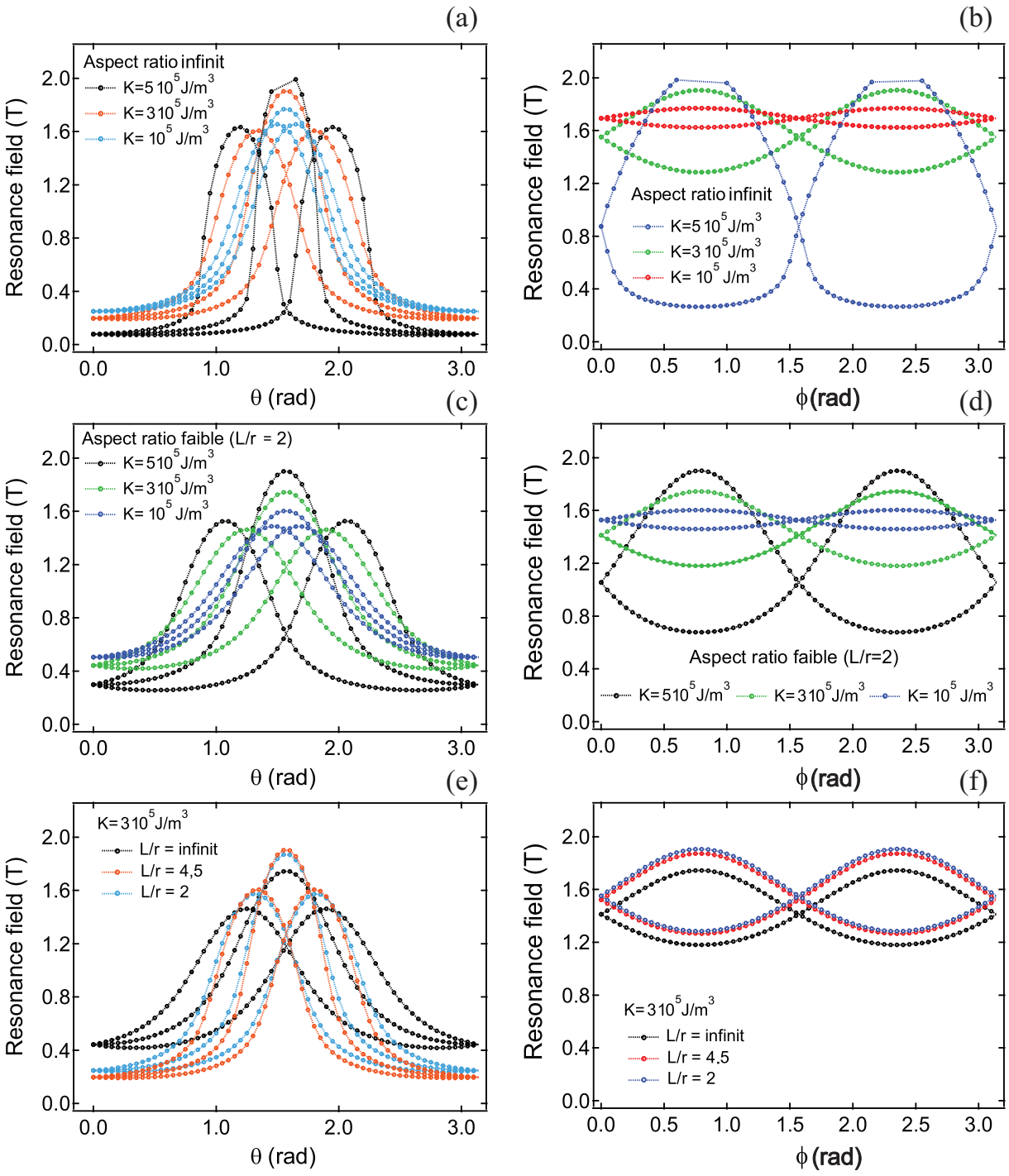

Figure 6.10: Simulations of the FMR spectra performed for different values of the aspect ratio and the magnetocrystalline anisotropy constant.

We consider that the magnetic domains are formed by one single crystallographic grain of hexagonal Co with axis pointing towards one of the four <111> directions. For each domain only one crystallographic direction is possible and it is expected that the four directions were equally probable. To account for this, we performed iterations for each one of the four possible directions separately. As the four directions have different

energy landscapes, the associated resonances are not necessarily equal. This is why we observe in the results of the simulations more than one resonance field for a given applied magnetic field. For example, in a plane containing <111> and <001> directions (θ-scan geometry) according to simulations, it would be possible to see up to three resonances at given angles and for a ϕ-scan up to two resonances would be present. The difference between the different resonance fields of different grains vanishes as the value of the magnetocrystalline constant decreases.

Figures 6.10(a), (b), (c) and (d) present the influence of the magnetocrystalline constant on the resonance field for some values of the aspect ratio. The value of this constant strongly affects the resonance in the plane of the sample (Figs. (b) and (d)); larger values of $K_{1,u}$ induce larger variations of the resonance fields with the ϕ angle. For out of plane measurements, the value of this constant causes principally a differentiation of the resonance fields of the different grains.

The best agreement between simulation and experimental results is shown in Figure 6.11 and was obtained for $K_{1,u} = 0.7{\times}10^5$ J/m^3 and $N_Z = 0.04$ which is the value for a cylinder with an aspect ratio of 7. In this figure the simulations are the solid lines and resonances for different grain directions are represented in different colors.

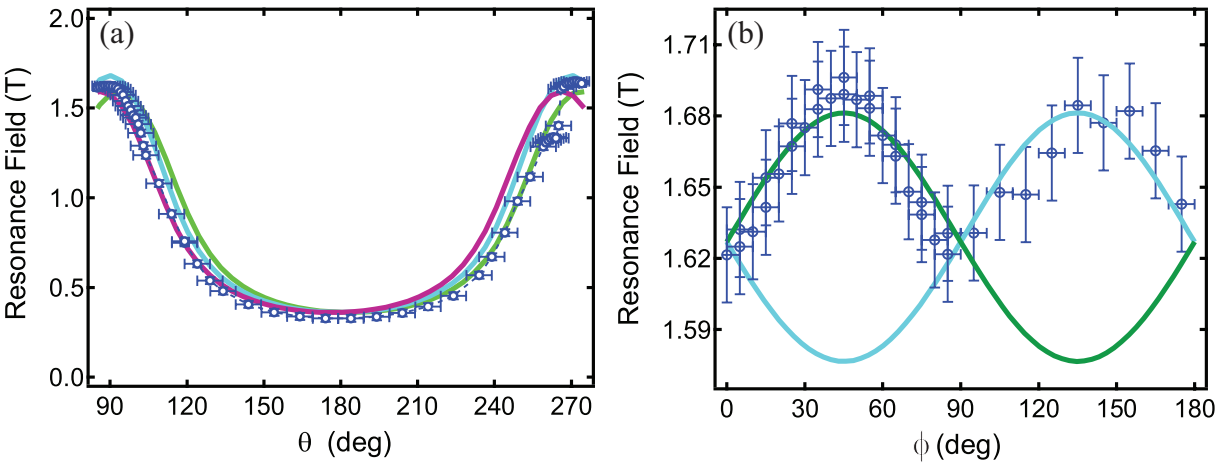

Figure 6.11: Comparison between the simulated results (lines) and experimental results (symbols) for $K_{1,u} = 0.7{\times}10^5$ J/m^3 and $N_Z = 0.04$. For the simulated results, the different colors represent resonances of different grains.

The value for $K_{1,u}$ is much lower than the bulk value. This attenuation can have two different explanations. One can imagine that for these very narrow FNWs, the value and the variation with T of $K_{1,u}$ might differ from the bulk. The low temperature value of $K_{1,u}$ may be lower than in the bulk and its decrease with T may be sharper. Indeed, in small particles, it is expected that some properties are modified with respect to the bulk

due to the lower coordination of surface/interface atoms.

On the other hand, the small value of $K_{1,u}$ extracted from the fitting procedure is at least partly due the approximations performed in modeling the structure of the grains. Indeed, the model neglects the exchange coupling between the grains. This exchange coupling adds some rigidity to the system and acts against the effects of $K_{1,u}$ in the localized reversal. Thus, the value extracted from the simulation is an effective magnetocrystalline anisotropy that is necessarily weaker than the bulk value.

The different resonance fields of different grains in the same magnetic field were not experimentally observed (neither in plane nor out of plane), probably because the effective magnetocrystalline anisotropy constant value estimated is very low, and under these conditions, the difference between the resonances of different grains is negligible compared to the width of the resonances. Moreover, for most of the measured spectra the approximation of a single Lorentzian peak is very doubtful. This suggests that two or more unresolved peaks can be present in the spectra. These peaks cannot be resolved because the shift of their resonance fields is much smaller than their width.

The resonance measurements were also performed at low temperature. For T <160 K, the resonance in the plane of the thin film could not be observed because the resonance field lies beyond the upper limit of the applied field. Thus, it was not possible to monitor the complete angular dependence of the resonance field at low T. The resonance field for θ-scan for some angles at $T = 88$ K is presented in figure 6.12.

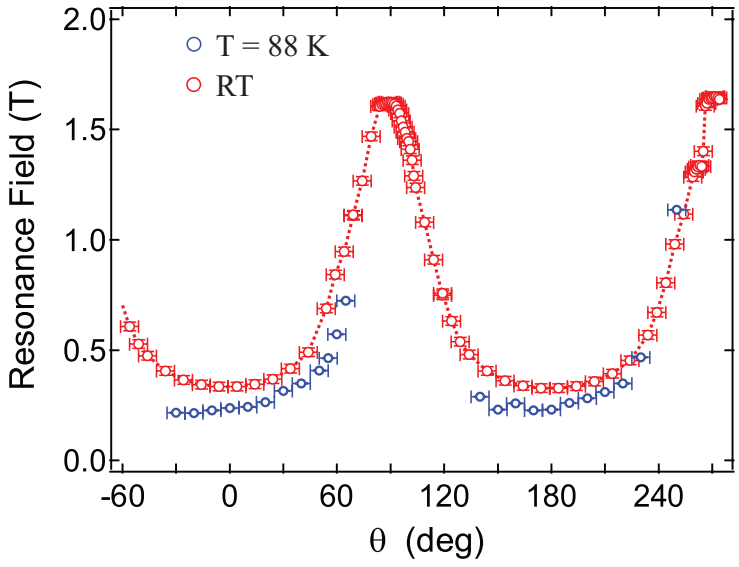

Figure 6.12: Resonance field as a function of θ at room temperature (red) and for $T = 88$ K(blue).

The data obtained at low temperature is insufficient to perform comparisons with simulations. It is expected that the coefficient $K_{1,u}$ is bigger at low temperature. The resonance fields for H_{app} parallel to the FNWs should then increase to values out of the range accessible with the FMR apparatus used. Further measurements may be done at low temperature for θ-scan at different ϕ-angles. Such measurements, together with simulations would be useful in order to extract values of the aspect ratio and magnetocrystalline constant at low temperature.

6.2.2 Ferromagnetic resonance for the d_5 sample

Ferromagnetic resonance was also performed for the d_5 sample. Some spectra at room temperature are presented in Figure 6.13 in θ-scan (a) and ϕ-scan (b) geometries.

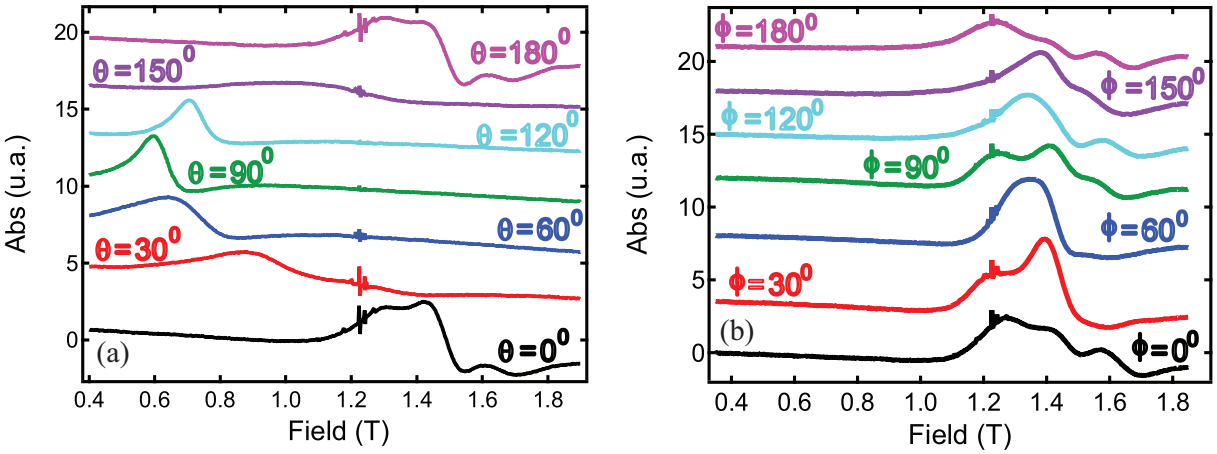

Figure 6.13: FMR spectra of d_5 sample for θ-scan(a) and ϕ-scan (b) geometries.

For θ-scans, a behavior similar to the one of the d_3 sample was observed but for the applied field parallel to the film surface (as well as for all spectra acquired in the ϕ-scan geometry), three peaks could be observed in the spectra. The origin of these three different resonances is not known but it could be linked to the high angular distribution for objects in this sample (as shown in section 4.4). Simulation has been performed for the results presented in θ-scan geometry with the same protocol mentioned above and considering $K_{1,u} = 0$. This way, the only parameter to vary was the aspect ratio of magnetic domains and the value found was corresponding to a cylinder with aspect ratio of 2. This result corroborate the previous assumptions or smaller (in length) magnetic domains due to higher disorder of d_5 sample in comparison with d_3 sample.

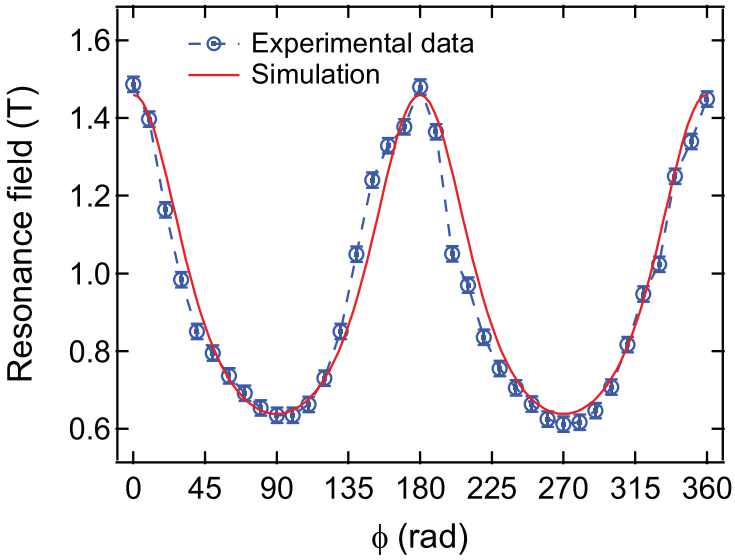

Figure 6.14: Comparison between simulated (solid line) and experimental data for d_5 sample.

6.3 Preliminary conclusions

In order to explain the weakening of the reversal localization with increasing temperatures, assumptions on the inner structure of Co FNW were made. These assumptions were verified by a careful analysis of HRTEM image, allowing us to determine the inner structure of the FNWs. Indexing multiple diffraction patterns, we could show that the wires are made of hcp Co grains with c-axis oriented parallel to one of the <111> directions of the CeO_2 matrix. Using a filtering procedure, cartographies of the grains in the two samples could be obtained. The results corroborate the previous assumptions on the grain size in the two samples. In d_5, the grains are small and their lateral extension can be smaller than the diameter. In contrast, the hcp grains in d_3 occupy the whole diameter and have length of the order of 5 to 20 nm. The hcp grains in d_3 should then lead to a non-zero contribution of the magnetocrystalline anisotropy to the total magnetic anisotropy of the system, as already postulated.

In order to check this, the anisotropy of the system was investigated using FMR. The angular variation of the resonance field in the out of plane geometry confirms that shape anisotropy dominates the magnetic behavior of d_3 and d_5. Also, the resonance field variation in the plane of d_3 corroborated the inner structure deduced from HRTEM analysis. Moreover, we could evaluate the values of the magnetocrystalline anisotropy contribution and aspect ratio of the grains through the comparison between simulated and experimental results.

7 Conclusions and perspectives

Co doped CeO_2 thin films were produced by pulsed laser deposition. Combining the results of HRTEM and XAS studies, we have evidenced the self-assembly of metallic Co nanowires in the epitaxial $CeO_2/SrTiO_3(001)$ matrix. The mechanisms of nanowires formation in this system is not fully understood yet. The complete understanding of the formation process is an exciting challenge for future studies.

This surprising result became even more interesting due the size of the objects formed: the nanowires have length of the order of hundreds nm (limited by the film thickness) and diameters that fall in the range between 3 and 7 nm with a very narrow diameters distribution. Such values lie at the limit of what can be envisaged with the other methods used to obtain such kind of system. Furthermore, such diameters are well below characteristic magnetic lengths such as the exchange length or the domain wall width. This makes the embedded Co nanowires interesting systems for nanomagnetism studies.

In order to study the impact of diameter reduction on magnetic properties of nanowires two samples were studied, d_5 and d_3, which possesses the same 15% Co content and narrow diameters distribution centered on 5 and 3 nm, respectively. Static and dynamic magnetic properties were investigated and we concluded to a localization of the magnetization reversal for both samples. Nevertheless, in the case of d_3, the magnetic behavior seems to be strongly influenced by magnetocrystalline anisotropy. This influence gives origin to an effective magnetic anisotropy that is temperature dependent, in contrast to shape anisotropy. For d_5, the energy barrier landscape does not vary strongly with temperature while for d_3 the variation in energy barrier landscape produces a strong localization of magnetization reversal at low temperature and a weakening of this localization as the temperature is increased.

The dissimilar magnetic behavior of these two samples has been related to the inner crystalline structure of the nanowires that was deduced from the analysis of multiple

diffraction patterns appearing in HRTEM data. In d_5, the nanowires are formed by small grains and the resulting magnetocrystalline anisotropy contribution is averaged to zero. In d_3, the crystalline grains are bigger, occupying the whole diameter extension of the wires, with length between 5 and 20 nm. This leads to a local contribution of the magnetocrystalline anisotropy to the total anisotropy. This was confirmed by a ferromagnetic resonance study.

The magnetic behavior of d_3 assembly can be summarized by:

- the reversal of magnetization is localized,
- the effective magnetic anisotropy depends on the temperature,
- the magnetic anisotropy can be described locally by a magnetostatic term and a magnetocrystalline term,
- there is a progressive delocalization of the reversal as the temperature increases,
- the magnetocrystalline term has a easy axis along one of the <111> direction of the matrix and its strength is lower than the bulk value of $K_{1,u}$ of hcp Co at room temperature.

In order to rationalize these observations we propose a simple model for localized reversal. The localized reversal occurs in the vicinity of an hcp grain oriented at 54.7° from the axis of the wire, separated by fcc regions (or regions with stacking faults). Outside the grain, Co is considered as fcc or polycrystalline and the magnetocrystalline anisotropy vanishes there (we neglect its value compared to $K_{1,u}$) . The magnetic energy can then be written as:

$$E = s \int \left\{ A \left(\frac{\partial \phi}{\partial x} \right)^2 + E_a(\phi, x) - M_s H \cos\phi \right\} dx \tag{7.1}$$

where $s = \pi R^2$ is the section of the wire, R is the radius of the wires, A is the exchange stiffness, ϕ is the angle between the magnetic moments and H is applied along the wires axis. E_a is the anisotropy energy density, modeled as:

$$E_a(\phi, x) = -K_m \cos^2\phi - K_u(x) \cos^2(\phi - \theta) \tag{7.2}$$

where K_m is the sum of the shape anisotropy and of the term related to interwire dipolar coupling, $K_u(x)$ is the magnetocrystalline anisotropy in the grain and θ is the orientation of the c axis of hcp Co with respect to the wire's axis. The model supposes the following

dependence for magnetocrystalline anisotropy in the vicinity of a grain:

$$K_u(x) = K_{1u} \exp(-x^2/\ell^2) \tag{7.3}$$

This model for the localized contribution of the magnetocrystalline anisotropy in the grain is illustrated in Figure 7.1. Following the approach developed by Kronmüller

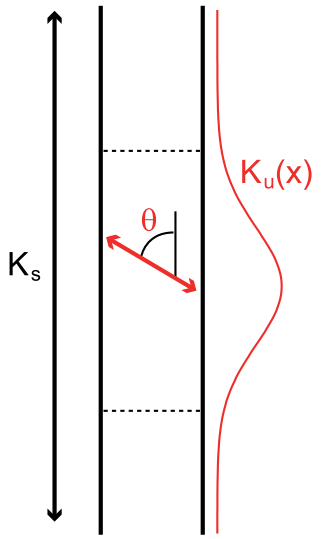

Figure 7.1: Model used to describe the contribution of a tilted hcp grain to the total magnetic anisotropy.

in (KRONMÜLLER, 1987) the nucleation field H_{nuc} can be calculated, resulting in:

$$H_{nuc} = \frac{2K_m}{M_s} - \frac{2K_{1u}|\cos 2\theta|}{M_s} + \frac{\delta_{DW}}{\pi\ell}\frac{2K_{1u}\sqrt{|\cos 2\theta|}}{M_s} \tag{7.4}$$

with $\delta_{DW} = \pi\sqrt{A/K_{1u}}$, the domain wall-width in hcp Co. Therefore, H_{nuc} can be written as the sum of three terms that can be identified as follows: the first one is related to shape anisotropy, the second is a drop related to the effect of magnetocrystalline anisotropy in the grain with tilted c-axis, the last one is related to the increase in exchange energy at the borders of the flipping region where magnetic moment are not parallel anymore.

In order to evaluate K_m, we need to take into account the dipolar coupling between wires. From mean field calculation (Julian Milano, private communication), the dipolar interaction would lead to a negative contribution to the anisotropy field of the order of $H_{dip,inter}$=-0.15 T, for a mean distance of 15 nm between the wires (mean distance between wires in d_3). From an estimate using $H_{dip,inter} = -6\pi M_s P$, where P is the porosity, following Encinas et al. (ENCINAS-OROPESA et al., 2001), we have $H_{dip,inter}$ = -0.14 T, in good agreement with the preceding value. Using the values available in the literature for the magnetic parameters of Co, the value of H_{nuc} can then be evaluated.

For ℓ=10 nm, we get H_{nuc}=0.63 T in very good agreement with the coercive field of d_3 at low temperature. Also, the value of ℓ is coherent with the size of the hcp grains detected in TEM images which is of the order of 5-20 nm. Moreover, grains of 10 nm length and 3 nm diameter correspond to volumes of $\sim$70 nm^3. This is fully coherent with the activation volume at low temperature extracted from viscosity measurements. Beyond this agreement between H_{nuc} and the value of H_c at low temperature, further effects can be interpreted in the scope of this model. First, the fact that $K_{1,u}$ depends on the temperature allows us to explain that temperature-independent energy barriers cannot be used to model the variation of H_c and S with the temperature. Finally, the nucleation field can be written as:

$$H_{nuc} = \frac{2K_m}{M_s} - \frac{2K_{1u}|\cos 2\theta|}{M_s}\left(1 - \frac{\delta_{DW}}{\pi\ell\sqrt{|\cos 2\theta|}}\right) \tag{7.5}$$

It is thus possible to identify an effective magnetocrystalline anisotropy given by:

$$K_{eff} = K_{1u}\left(1 - \frac{\delta_{DW}}{\pi\ell\sqrt{|\cos 2\theta|}}\right) \tag{7.6}$$

Thus, the magnitude K_{eff} is lower than $K_{1,u}$ due to the extra stiffness added by exchange at the border of the grains. This trend is coherent with the FMR measurements and analysis that leads to a magnetocrystalline anisotropy lower than $K_{1,u}$.

To conclude with the reversal in d_3, the model of localized reversal in hcp grains is coherent with the results obtained from magnetic measurements. The localization of the reversal is due to the presence of hcp grains with a tilted c-axis. Due to this tilt, there is a competition of shape and magnetic anisotropies that leads to a local reduction of the energy barrier and to a localized reversal.

The present study is a step towards the intimate correlation of magnetism and real structure in very thin Co nanowires. A direct and short-term perspective of this work is to continue working along these lines and to explore the magnetic properties of Co wires of different radius and different structures. Indeed it may be possible to reduce further the diameter of the nanowires by playing with the growth conditions.

Further perspectives

Another perspective is to test other materials. Recently we have tried to grow Ni wires embedded in CeO_2 using a similar recipe as the one used for Co. We have observed

the formation of Ni wires in the matrix. EFTEM and HRTEM images of these nanowires are depicted in Figure 7.2 and Figure 7.3, respectively.

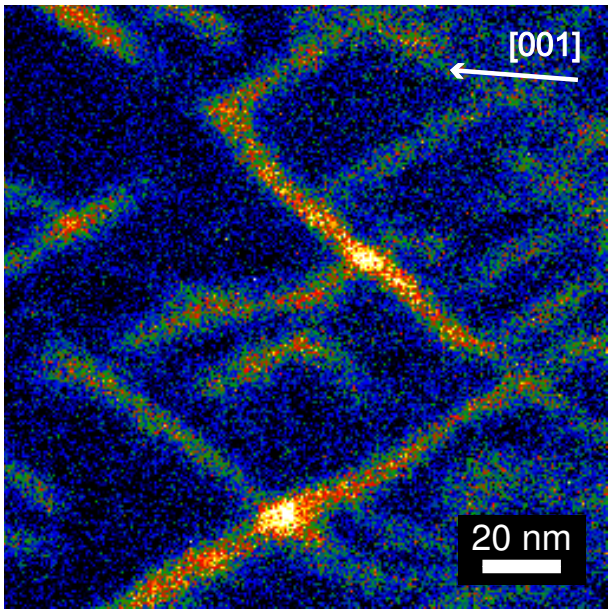

Figure 7.2: EFTEM image, taken at the Ni L-edge, of a Ni containing CeO_2 film grown on $SrTiO_3$(001). The arrow indicates the growth direction along [001] of $SrTiO_3$.

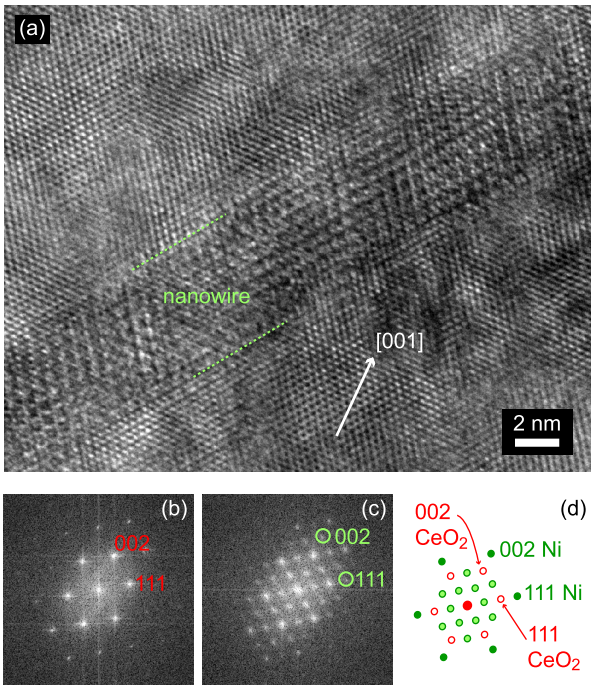

Figure 7.3: HRTEM image of a Ni containing CeO_2 film grown on $SrTiO_3$(001). The arrow indicates the growth direction along [001] of $SrTiO_3$.

Surprisingly, the wires grow along slanted directions with respect to the surface normal, as shown in Figure 7.2. This remains to be understood and mastered. Most

importantly, playing with the growth conditions may lead to a better alignment of the wires. A good point of the Ni nanowires is that Ni grows epitaxially within the matrix as shown in Figure 7.3.

In the medium term, it could be interesting to test the growth of $Co_{(1-x)}Ni_x$ nanowires. It could be a good compromise to have at the same time epitaxial fcc nanowires and a higher saturation magnetization than in Ni and thus a higher shape anisotropy. In the long term, an exciting perspective would be to find strategies to connect these nanowires. It would then be possible to study their transport properties (conductivity, magnetoresistance...). Finding ways to connect the wires (initiate the growth on conducting substrates with wires in contact with the substrates, connecting the wires on the free surface) is a challenge from the elaboration point of view.

Bibliography

AMPÉRE, A. *Recueil d'observations électro-dynamiques*. Paris: Crochard, 1822.

ATKINSON, D. et al. Magnetic domain-wall dynamics in a submicrometre ferromagnetic structure. *NATURE MATERIALS*, NATURE PUBLISHING GROUP, MACMILLAN BUILDING, 4 CRINAN ST, LONDON N1 9XW, ENGLAND, v. 2, n. 2, p. 85–87, 2003.

AUBERLECHNER, U.; KASPERKOVITZ, P.; STEINER, W. A theoretical discussion of vector pick-up systems for squid magnetometers. *Measurement Science and Technology*, v. 9, n. 6, p. 989, 1998. Disponível em: <http://stacks.iop.org/0957-0233/9/i=6/a=017>.

BEDANTA, S.; KLEEMANN, W. Supermagnetism. *Journal of Physics D: Applied Physics*, v. 42, n. 1, p. 013001, 2009. Disponível em: <http://stacks.iop.org/0022-3727/42/i=1/a=013001>.

BLOCH, F. Zur theorie des austauschproblems und der remanenzerscheinung der ferromagnetika. *Zeitschrift für Physik A Hadrons and Nuclei*, Springer Berlin / Heidelberg, v. 74, p. 295–335, 1932. Disponível em: <http://dx.doi.org/10.1007/BF01337791>.

BLUNDELL, S. *Magnetism in condensed matter*. Paris: Oxford University Press, 2001. (Oxford master).

BONILLA, F. *Elaboration and study of magnetic properties of self-assembled cobalt nanowires obtained by pulsed laser deposition (PLD)*. Dissertao (Mestrado) — Universite Pierre et Marie Curie Paris 06 - Master Nanomat, 2010.

BROWN, W. F. Thermal fluctuations of a single-domain particle. *Phys. Rev.*, American Physical Society, v. 130, p. 1677–1686, Jun 1963. Disponível em: <http://link.aps.org/doi/10.1103/PhysRev.130.1677>.

CEZAR, J. C.; VICENTIN, F. C.; TOLENTINO, H. C. N. Aplicação de Técnicas de Absorção de Raios x no Estudo de Materiais Magnéticos. *Revista Brasileira de Ensino de Fisica*, v. 22, n. 3, p. 363 –377, 2000. Disponível em: <http://www.sbfisica.org.br/rbef/pdf/v22_363.pdf>.

CHEN, D.-X.; BRUG, J.; GOLDFARB, R. B. Demagnetizing factors for cylinders. *Magnetics, IEEE Transactions on*, v. 27, n. 4, p. 3601 –3619, jul 1991.

CHIPARA, M. et al. Ferromagnetic resonance on ni nanowire arrays. *JOURNAL OF MATERIALS RESEARCH*, CAMBRIDGE UNIV PRESS, v. 26, n. 17, p. 2169–2174, 2011.

CHRISTEN, H. M.; ERES, G. Recent advances in pulsed-laser deposition of complex oxides. *Journal of Physics: Condensed Matter*, v. 20, n. 26, p. 264005, 2008. Disponível em: <http://stacks.iop.org/0953-8984/20/i=26/a=264005>.

CHUNG, H. V. et al. Studies on gold atom chains and lead nanowires on silicon vicinal surfaces. *Journal of Physics: Conference Series*, v. 187, n. 1, p. 012025, 2009. Disponível em: <http://stacks.iop.org/1742-6596/187/i=1/a=012025>.

COEY, J.; CHAMBERS, S. Oxide Dilute Magnetic Semiconductors: Fact or Fiction? *MRS Bulletin*, v. 33, p. 1053–1058, 2008.

COEY, J. M. D. *Magnetism and Magnetic Materials*. New York: Cambridge University Press, 2010.

COLLOCOTT, S. J.; DUNLOP, J. B. Anomalous magnetic viscosity in the bulk-amorphous ferromagnet $Nd_{60}Fe_{20}Co_{10}Al_{10}$. *Phys. Rev. B*, American Physical Society, v. 66, n. 22, p. 224420, Dec 2002.

CULLITY, B.; GRAHAM, C. *Introduction to Magnetic Materials*. New Jersey: John Wiley & Sons, 2009.

DIETL, T. et al. Zener model description of ferromagnetism in zinc-blende magnetic semiconductors. *Science*, Amer Assoc Advancement Science, v. 287, n. 5455, p. 1019–1022, fev. 2000.

DYSON, F. J. Thermodynamic behavior of an ideal ferromagnet. *Phys. Rev.*, American Physical Society, v. 102, n. 5, p. 1230–1244, Jun 1956.

EASON, R. *Pulsed laser deposition of thin films: applications-led growth of functional materials*. New Jersey: Wiley-Interscience, 2007.

EGERTON, R. *Electron energy-loss spectroscopy in the electron microscope*. New York: Springer, 2011. (Language of science).

EGERTON, R. F. Electron energy-loss spectroscopy in the tem. *Reports on Progress in Physics*, v. 72, n. 1, p. 016502, 2009. Disponível em: <http://stacks.iop.org/0034-4885/72/i=1/a=016502>.

ENCINAS-OROPESA, A. et al. Dipolar interactions in arrays of nickel nanowires studied by ferromagnetic resonance. *Phys. Rev. B*, American Physical Society, v. 63, p. 104415, Feb 2001. Disponível em: <http://link.aps.org/doi/10.1103/PhysRevB.63.104415>.

ENDERS, A. et al. Temperature dependence of the magnetism in Fe/Cu(001). *Phys. Rev. B*, American Physical Society, v. 72, n. 5, p. 054446, Aug 2005.

FARADAY, M. *Experimental researches in electricity*. Havard: R. and J. E. Taylor, 1839. (Experimental Researches in Electricity, *all volumes*).

FEYNMAN, R.; LEIGHTON, R.; SANDS, M. *The Feynman lectures on physics*. [S.l.]: Addison-Wesley Pub. Co., 1965. (The Feynman Lectures on Physics, v. 2).

FRUCHART, O.; THIAVILLE, A. Magnetism in reduced dimensions. *Comptes Rendus Physique*, v. 6, n. 9, p. 921 – 933, 2005. ISSN 1631-0705. Disponível em: <http://www.sciencedirect.com/science/article/pii/S1631070505001659>.

GAO, J.-H. et al. Magnetization reversal process and magnetic relaxation of self-assembled Fe_3Pt nanowire arrays with different diameters: Experiment and micromagnetic simulations. *Phys. Rev. B*, American Physical Society, v. 75, p. 064421, Feb 2007. Disponível em: <http://link.aps.org/doi/10.1103/PhysRevB.75.064421>.

GAO, J.-H. et al. Thermally activated magnetization reversal process of self-assembled $Fe_{55}Co_{45}$ nanowire arrays. *Journal of Magnetism and Magnetic Materials*, v. 305, n. 2, p. 365 – 371, 2006. ISSN 0304-8853. Disponível em: <http://www.sciencedirect.com/science/article/pii/S0304885306000357>.

GAUNT, P. Magnetic viscosity in ferromagnets .1. phenomenological theory. *Philosophical Magazine*, Taylor & Francis Ltd, v. 34, n. 5, p. 775–780, 1976.

GAUNT, P. Magnetic viscosity and thermal activation energy. *Journal of Applied Physics*, AIP, v. 59, n. 12, p. 4129–4132, 1986. ISSN 00218979. Disponível em: <http://dx.doi.org/10.1063/1.336671>.

GILBERT, W. *De Magnete*. New York: Dover Publications, 1958. (Dover Classics of Science and Mathematics).

GUIMARÃES, A. P. *Magnetism and magnetic resonance in solids*. New York: J. Wiley, 1998.

GUIMARÃES, A. P. *From Lodestone to Supermagnets*. Berlim: Wiley-VCH, 2005.

GUIMARÃES, A. P. *Principles of Nanomagnetism*. [S.l.]: Springer, 2009. (Nanoscience and Technology).

HAN, X.-F.; SHAMAILA, S.; SHARIF, R. Ferromagnetic nanowires and nanotubes. In: LUPU, N. (Ed.). *Electrodeposited Nanowires and their Applications*. [S.l.]: InTech, 2010.

HERTEL, R. Computational micromagnetism of magnetization process in nickel nanowires. *Journal of Magnetism and Magnetic Materials*, v. 249, p. 251–256, 2002. Disponível em: <http://www.sciencedirect.com/science/article/pii/s0304885302005395>.

HERZER, G. Magnetization process in nanocrystalline ferromagnets. *Materials Science and Engineering: A*, v. 133, p. 1 – 5, 1991. ISSN 0921-5093. Proceedings of the Seventh International Conference on Rapidly Quenched Materials. Disponível em: <http://www.sciencedirect.com/science/article/pii/0921509391900036>.

HUBERT, A.; SCHÄFER, R. *Magnetic Domains: the analyses of Magnetic Microstuctures*. Germany: Springer, 2009.

JUHASZ, R.; ELFSTRM, N.; LINNROS, J. Controlled fabrication of silicon nanowires by electron beam lithography and electrochemical size reduction. *Nano Letters*, v. 5, n. 2, p. 275–280, 2005. Disponível em: <http://pubs.acs.org/doi/abs/10.1021/nl0481573>.

KRONMÜLLER, H. Theory of nucleation fields in inhomogeneous ferromagnets. *physica status solidi (b)*, WILEY-VCH Verlag, v. 144, n. 1, p. 385–396, 1987. Disponível em: <http://dx.doi.org/10.1002/pssb.2221440134>.

LANDAU, L.; LIFSHITS, E. On the theory of dispersion of magnetic permeability in ferromagnetic bodies. *Phys. Z. Sowjetunion*, v. 8, p. 153169, 1935.

LEIGHTON, C.; SCHULLER, I. K. Magnetic viscosity measurements reveal reversal asymmetry in exchange-biased bilayers. *Phys. Rev. B*, American Physical Society, v. 63, n. 17, p. 174419, Apr 2001.

LI, J. et al. Highly-ordered carbon nanotube arrays for electronics applications. *Applied Physics Letters*, AIP, v. 75, n. 3, p. 367–369, 1999. Disponível em: <http://link.aip.org/link/?APL/75/367/1>.

LINDNER, J.; FARLE, M. Magnetic anisotropy of heterostructures. In: _____. Berlin, Heidelberg: Springer, 2088. (Springer Tracts in Modern Physics, v. 227), cap. 2, p. 57.

MAURER, T. et al. Exchange bias in Co/CoO core-shell nanowires: Role of antiferromagnetic superparamagnetic fluctuations. *Phys. Rev. B*, American Physical Society, v. 80, p. 064427, Aug 2009. Disponível em: <http://link.aps.org/doi/10.1103/PhysRevB.80.064427>.

MAXWELL, J. *A Treatise on Electricity and Magnetism*. New York: Cambridge University Press, 2010. (Cambridge Library Collection - Physical Sciences).

MIYAWAKI, J. et al. Structural study of Co/Pd(111) and CO/Co/Pd(111) by surface X-ray absorption fine structure spectroscopy. *Surface Science*, v. 601, n. 1, p. 95 – 103, 2007. ISSN 0039-6028. Disponível em: <http://www.sciencedirect.com/science/article/pii/S0039602806009526>.

NIELSCH, K. et al. Hexagonally ordered 100 nm period nickel nanowire arrays. *Applied Physics Letters*, AIP, v. 79, n. 9, p. 1360–1362, 2001. Disponível em: <http://link.aip.org/link/?APL/79/1360/1>.

NOLTING, W.; RAMAKANTH, A. *Quantum Theory of Magnetism*. [S.l.]: Springer, 2009.

OERSTED, H. C. Experiments on the effect of a current of electricity on the magnetic needle. In: THOMSON, T.; PHILLIPS, R.; BRAYLEY, E. (Ed.). *The Annals of Philosophy*. Michigan: Baldwin, Cradock, and Joy., 1820. v. 16, p. 273 – 276.

OERSTED, H. C. Thermo-electricity. In: BREWSTER, D. (Ed.). *Edinburgh encyclopedia*. Edinburgh: William Backwood, 1830. p. 573 – 589.

ONO, F.; MAETA, H. Thermal expansion and magnetocrystalline anisotropy in hcp cobalt. *Physica B: Condensed Matter*, v. 161, n. 1-3, p. 134 – 138, 1989. ISSN 0921-4526. Disponível em: <http://www.sciencedirect.com/science/article/pii/0921452689901191>.

PAULUS, P. et al. Low-temperature study of the magnetization reversal and magnetic anisotropy of Fe, Ni, and Co nanowires. *Journal of Magnetism and Magnetic Materials*, v. 224, n. 2, p. 180 – 196, 2001. ISSN 0304-8853. Disponível em: <http://www.sciencedirect.com/science/article/pii/S0304885300007113>.

REIMER, L.; KOHL, H. *Transmission electron microscopy: physics of image formation*. [S.l.]: Springer, 2008. (Springer series in optical sciences). ISBN 9780387400938.

RODENBURG, J. *Learn to use TEM: an introductory guide by John Rodenburg*. 2004. Disponível em: <http://www.rodenburg.org/guide/index.html>.

SELLMYER, D. J.; ZHENG, M.; SKOMSKI, R. Magnetism of Fe, Co and Ni nanowires in self-assembled arrays. *Journal of Physics: Condensed Matter*, v. 13, n. 25, p. R433, 2001. Disponível em: <http://stacks.iop.org/0953-8984/13/i=25/a=201>.

SHARROCK, M. P. Time dependence of switching fields in magnetic recording media (invited). *Journal of Applied Physics*, AIP, v. 76, n. 10, p. 6413–6418, 1994. ISSN 00218979. Disponível em: <http://dx.doi.org/10.1063/1.358282>.

SKOMSKI, R. Nanomagnetics. *Journal of Physics: Condensed Matter*, v. 15, n. 20, p. R841, 2003. Disponível em: <http://stacks.iop.org/0953-8984/15/i=20/a=202>.

SKOMSKI, R. *Simple models of magnetism*. Oxford: Oxford University Press, 2008.

SKOMSKI, R. et al. Magnetic localization in transition-metal nanowires. *Phys. Rev. B*, American Physical Society, v. 62, p. 3900–3904, Aug 2000. Disponível em: <http://link.aps.org/doi/10.1103/PhysRevB.62.3900>.

SLICHTER, C. *Principles of magnetic resonance*. Berlin: Springer, 1990. (Springer series in solid-state sciences).

SONG, T.; PARK, W. I.; PAIK, U. Epitaxial growth of one-dimensional gan nanostructures with enhanced near-band edge emission by chemical vapor deposition. *Applied Physics Letters*, AIP, v. 96, n. 1, p. 011105, 2010. Disponível em: <http://link.aip.org/link/?APL/96/011105/1>.

STAMENOV, P.; COEY, J. M. D. Sample size, position, and structure effects on magnetization measurements using second-order gradiometer pickup coils. *Review of Scientific Instruments*, AIP, v. 77, n. 1, p. 015106, 2006. Disponível em: <http://link.aip.org/link/?RSI/77/015106/1>.

STONER, E. C.; WOHLFARTH, E. P. A mechanism of magnetic hysteresis in heterogeneous alloys. *Philosophical Transactions of the Royal Society of London. Series A, Mathematical and Physical Sciences*, v. 240, n. 826, p. 599–642, 1948. Disponível em: <http://rsta.royalsocietypublishing.org/content/240/826/599.abstract>.

STREET, R.; WOOLLEY, J. C. A study of magnetic viscosity. *Proceedings of the Physical Society. Section A*, v. 62, n. 9, p. 562, 1949. Disponível em: <http://stacks.iop.org/0370-1298/62/i=9/a=303>.

STRIJKERS, G. J. et al. Structure and magnetization of arrays of electrodeposited co wires in anodic alumina. *Journal of Applied Physics*, AIP, v. 86, n. 9, p. 5141–5145, 1999. ISSN 00218979. Disponível em: <http://dx.doi.org/10.1063/1.371490>.

STUART, R.; MARSHALL, W. Direct exchange in ferromagnets. *Phys. Rev.*, American Physical Society, v. 120, p. 353–357, Oct 1960. Disponível em: <http://link.aps.org/doi/10.1103/PhysRev.120.353>.

SUN, L. et al. Tuning the properties of magnetic nanowires. *IBM Journal of Research and Development*, v. 49, p. 79 – 102, 2005.

SUN, S. et al. Monodisperse fept nanoparticles and ferromagnetic fept nanocrystal superlattices. *Science*, v. 287, n. 5460, p. 1989–1992, 2000. Disponível em: <http://www.sciencemag.org/content/287/5460/1989.abstract>.

SUN, Y. et al. Memory effects in an interacting magnetic nanoparticle system. *Phys. Rev. Lett.*, American Physical Society, v. 91, p. 167206, Oct 2003. Disponível em: <http://link.aps.org/doi/10.1103/PhysRevLett.91.167206>.

TONG, H. D. et al. Novel top-down wafer-scale fabrication of single crystal silicon nanowires. *Nano Lett.*, American Chemical Society, v. 9, n. 3, p. 1015–1022, jan. 2009. ISSN 1530-6984. Disponível em: <http://dx.doi.org/10.1021/nl803181x>.

UNG, D. et al. Growth of magnetic nanowires and nanodumbbells in liquid polyol. *Chemistry of Materials*, v. 19, n. 8, p. 2084–2094, 2007. Disponível em: <http://pubs.acs.org/doi/abs/10.1021/cm0627387>.

VÁZQUEZ, M. et al. Arrays of ni nanowires in alumina membranes: magnetic properties and spatial ordering. *Eur. Phys. J. B*, v. 40, n. 4, p. 489–497, 2004. Disponível em: <http://dx.doi.org/10.1140/epjb/e2004-00163-4>.

VÁZQUEZ, M.; VIVAS, L. G. Magnetization reversal in co-base nanowire arrays. *physica status solidi (b)*, WILEY-VCH Verlag, v. 248, n. 10, p. 2368–2381, 2011. ISSN 1521-3951. Disponível em: <http://dx.doi.org/10.1002/pssb.201147092>.

VODUNGBO, B. *Systèmes oxyde pour l'éctronique de spin : étude de l'oxyde magnétique dilué CeO_2 dopé au cobalt et d'assemblées de nano-particules de cobalt dans $TiO_{2-\delta}$.* Tese (Doutorado) — Universit*é* Pierre et Marie Curie, UPMC, 2008. Disponível em: <http://tel.archives-ouvertes.fr/tel-00248420/fr/>.

WEGROWE, J.-E. et al. Magnetic relaxation of nanowires: beyond the néel-brown activation process. *Europhys. Lett.*, v. 38, n. 5, p. 329–334, 1997. Disponível em: <http://dx.doi.org/10.1209/epl/i1997-00247-9>.

WILLMOTT, P. Deposition of complex multielemental thin films. *Progress in Surface Science*, v. 76, n. 6-8, p. 163 – 217, 2004. Disponível em: <http://www.sciencedirect.com/science/article/pii/S0079681604000371>.

WU, Y.; YANG, P. Direct observation of vaporliquidsolid nanowire growth. *Journal of the American Chemical Society*, v. 123, n. 13, p. 3165–3166, 2001. Disponível em: <http://pubs.acs.org/doi/abs/10.1021/ja0059084>.

ZACH, M. P.; NG, K. H.; PENNER, R. M. Molybdenum nanowires by electrodeposition. *Science*, v. 290, n. 5499, p. 2120–2123, 2000. Disponível em: <http://www.sciencemag.org/content/290/5499/2120.abstract>.

ZENG, H. et al. Structure and magnetic properties of ferromagnetic nanowires in self-assembled arrays. *Phys. Rev. B*, American Physical Society, v. 65, p. 134426, Mar 2002. Disponível em: <http://link.aps.org/doi/10.1103/PhysRevB.65.134426>.

ZHENG, Y. et al. Growth and structural analysis of diluted magnetic oxide Co-doped $CeO_{2-\delta}$ films deposited on Si and $SrTiO_3$ (100). *Journal of Crystal Growth*, v. 310, n. 14, p. 3380 – 3385, 2008. ISSN 0022-0248. Disponível em: <http://www.sciencedirect.com/science/article/pii/S0022024808003278>.